DGK Veröffentlichungen der DGK

Ausschuss Geodäsie der Bayerischen Akademie der Wissenschaften

Reihe C | Dissertationen | Heft Nr. 884

Wei Liu

Understanding ocean tide aliasing in satellite gravimetry

München 2022

Bayerische Akademie der Wissenschaften

ISSN 0065-5325 ISBN 978-3-7696-5296-3

Diese Arbeit ist gleichzeitig publiziert als E-Dissertation auf
OPUS - Online Publikationen der Universität Stuttgart
<https://elib.uni-stuttgart.de/handle/11682/10502>, Stuttgart 2019

DGK Veröffentlichungen der DGK

Ausschuss Geodäsie der Bayerischen Akademie der Wissenschaften

Reihe C Dissertationen Heft Nr. 884

Understanding ocean tide aliasing in satellite gravimetry

A thesis
accepted by the Faculty of Aerospace Engineering and Geodesy
of the University of Stuttgart
in partial fulfillment of the requirements for the
degree of Doctor of Engineering Sciences (Dr.-Ing.)

by

Wei Liu

born in Zhangjiakou, China

München 2022

Bayerische Akademie der Wissenschaften

ISSN 0065-5325 ISBN 978-3-7696-5296-3

Diese Arbeit ist gleichzeitig publiziert als E-Dissertation auf
OPUS - Online Publikationen der Universität Stuttgart <https://elib.uni-stuttgart.de/handle/11682/10502>, Stuttgart 2019

Adresse der DGK:

Ausschuss Geodäsie der Bayerischen Akademie der Wissenschaften (DGK)

Alfons-Goppel-Straße 11 ● D – 80 539 München

Telefon +49 – 89 – 23 031 1113 ● Telefax +49 – 89 – 23 031 - 1283 / - 1100

e-mail post@dgk.badw.de ● http://www.dgk.badw.de

Main referee: Prof. Dr.-Ing. Nico Sneeuw

Co-referee: Prof. Dr.techn. Roland Pail

Date of defense: 6 June 2019

ISSN 0065-5325 ISBN 978-3-7696-5296-3

To my dear grandfathers.

Acknowledgements

I have tried hard to start with a beautiful sentence to express my current emotions at this very end of my stage working for a doctorate, but it seems no words can do that job well. Although words are limited, true feelings are endless. On the way of "growing up", I am never alone. Therefore, I would like to use my limited words to express my sincere gratitude to those of you who are always at my side.

First and foremost, I would like to thank my supervisor, my mentor, and my friend, Nico Sneeuw. Thank you so much for giving me the opportunity to continue my higher education at the Institute of Geodesy, for offering me the continuous supports in my study, for encouraging me to leave my comfort zone and seek for the truth step by step, for generously sharing your wisdom and knowledge, and for leading me to be a real researcher. Without you, I could not reach this point, with satisfaction, confidence and hope in myself. Doing research sometimes could be tough, but working with you is always pleasant. I appreciate all the efforts you have made, either consciously or unconsciously, to help me smooth my research life and fulfil my dream.

I would like to express my gratitude to Roland Pail. I have learnt a lot from you during the past two years of working together, both in academic aspect and in routines. You showed me a great model of being a good researcher and a good project manager at the same time. Special thanks to you for being my examiner and giving nice advice in polishing my work.

I am also very grateful to my supervisor in Wuhan University, another mentor of me, Weiping Jiang. I am so thankful that I have received your continuous guides and supports in all aspects of my life for so many years. You are the one who motivated me to go out to see the world. You never stopped thinking for me, and never stopped guiding me to figure out who I am and what I really want. Thank you so much.

Thanks also go to all my dear colleagues, who have been so helpful to my research and everyday routines, and who have filled my days with a lot of joy. I have had a lot of nice discussions with all of you, which enlarge my knowledge and broaden my horizon. Thanks so much for your kindly inputs to my mind. Special thanks to Jianqin Cai for giving me a lot of good suggestions to be easy in my study, work and life; to Markus

Antoni for always being so patent and ready to give me all kinds of answers and help; to Qian Chen and Brama Dutt Vishwakarma for comforting me when I felt bad as a beginner; and to Anita Vollmer, Ron Schlesinger and Thomas Götz who have supported me a lot in living smoothly at the institute.

I would like to thank all my friends who accompany me in one way or another, and act as good listeners and advisers.

I wish to express my appreciation to my parent's unconditional love, understanding and supports during my long years of study.

Finally, many thanks to China Scholarship Council (CSC) for supporting my PhD study in Germany.

Contents

Abstract

With the innovative and successful CHAMP (CHAllenging Mini-satellite Payload) mission (2000–2010), GOCE (Gravity field and steady-state Ocean Circulation Explorer) mission (2009–2013) and GRACE (Gravity Recovery and Climate Experiment) mission (2002–2017), and the launch of its successor GRACE-Follow-On (2018), satellite gravimetry plays an increasingly important role in modelling the static and temporal gravity fields, detecting geophysical signals and monitoring Earth mass change processes. Among the Earth temporal gravitational signals, ocean tides have relative high frequencies such as semi-diurnal and diurnal, which are fundamentally undersampled by the satellites with an absolute orbit precession of about 0.02–0.46°/day and by the gravity recovery with a weekly or even monthly average. Therefore, aliasing of ocean tides into low-frequency gravity solutions is unavoidable. The alias periods of different constituents vary from several days up to infinity. In general, an ocean tide model is included while recovering the gravity fields to remove the ocean tide signals. However, the uncertainty of the ocean tide model causes the ocean tide errors remaining in the fields. As a result, those ocean tide errors are undersampled, resulting in aliasing errors. In the past decades, it has been amply demonstrated that ocean tide aliasing is a significant problem including evidence of S_2 aliasing in GRACE data. The problem can become more severe with the technology improvement of the on-board payloads, e.g. from micro-wave K-band ranging to laser ranging, which is being tested on the GRACE-Follow-On mission and may be widely used in future missions.

Though this problem attracts enough attention, the understanding of the ocean tide aliasing in satellite gravimetry is insufficient. In view of this, this work

- elaborates the mechanism of the ocean tide aliasing systematically,
- demonstrates the mechanism analytically or numerically,
- applies the derived mechanism in reducing the tidal aliasing in post-processing, and
- makes suggestions for the future mission design aiming at ocean tide aliasing error mitigation.

To be specific, a two-step aliasing mechanism for satellite gravimetry is elaborated. A

primary aliasing is due to the orbital undersampling of the ocean tides. The orbital sampling is determined by the orbit precession. The periodic patterns of the observations along the orbits demonstrate the primary aliasing periods well. Those patterns also indicate the phase sampling of the ocean tides by the orbits, which can be used for orbit design of future missions.

A secondary aliasing is due to the undersampling of the primary aliases by gravity recovery. Gravity recovery is a process of combining the observations or geopotential functionals both in space and in time. Geophysical signals are averaged within the recovery periods at different spatial scales. In general, each recovered solution can be considered as a sample. Therefore, the secondary aliasing occurs when the primary aliasing period and the recovery period do not satisfy the Nyquist sampling rule. The secondary aliasing can be revealed by the spectral analysis of the recovered fields.

Primary and secondary aliasing periods are unique under the conditions that the groundtrack pattern of a given spatial scale is homogeneous within a single recovery period and consistent among different recovery intervals. Otherwise, side aliasing frequencies show up.

The aliasing behaviour of an individual constituent is investigated for GRACE-type formations and Bender-type constellations. The aliasing periods of a Bender-type constellation is a stack of the aliasing periods of each single pair. In other words, the aliasing of a constellation can be treated by individual pairs separately and interference among them needs no special handling.

Ocean tide aliasing errors can be reduced significantly by least-squares spectral estimation at the aliasing frequencies in post-processing. In general, the primary aliasing affects the spherical harmonic coefficients in the whole spectrum, and the secondary aliasing has more influence on the zonal and lower order tesseral coefficients. Aliasing does not correlate with striping, but removing the aliasing errors does reduce the striping errors.

According to the phase sampling of the ocean tides by the orbits, the optimal node separation(s) for a double- or triple-pair constellation with respect to individual constituents is analysed. A constellation can be self-dealiasing by following the out-of-phase sampling criteria. As each tidal constituent has different frequencies, the optimal nodal separation for each constituent is different. Therefore, one needs to make a compromise according to different objectives.

Zusammenfassung

Mit der innovativen und erfolgreichen CHAMP-Mission (CHAllenging Mini-satellite Payload (2000–2010), GOCE-Mission (Gravity field and steady-state Ocean Circulation Explorer) (2009–2013), GRACE-Mission (Gravity Recovery and Climate Experiment) (2002–2017) und dem Start der Nachfolgemission GRACE-Follow-On (2018) spielt die Satellitengravimetrie eine zunehmend wichtige Rolle in der Modellierung des statischen und zeitlich-variablen Schwerefeldes, der Erfassung geophysikalischer Signale und der Überwachung von Massentransportprozessen in der Erde. Unter den zeitlich-variablen gravitativen Signalen der Erde haben die Ozeangezeiten die höchsten Frequenzen, welche jedoch durch Satelliten grundsätzlich zu gering abgetastet werden, zum einen durch die absolute Präzession von etwa 0.02–0.46°/Tag zum anderen durch die Erfassung des Schwerefeldes in wöchentlichen oder gar monatlichen Mittelwerten. Daher ist das Aliasing der Ozeangezeiten in die niedrigen Frequenzen der Schwerfeldlösungen nicht vermeidbar. Im Allgemeinen wird ein Ozeangezeitenmodell für die Bestimmung des Schwerefeldes berücksichtigt, um die Signale der Ozeangezeiten zu eliminieren. Die Unsicherheiten der Ozeangezeitenmodelle bewirken jedoch den Verbleib von Fehleranteilen der Ozeangezeiten in den Schwerefeldlösungen. Da die Fehler der Ozeangezeiten ihrerseits aus der zu geringen Abtastung entstehen, ergeben sich Aliasingfehler. In den letzten Jahrzehnten wurde mehrfach demonstriert, dass das Aliasing der Ozeangezeiten – insbesondere der nachgewiesene S_2-Effekt – ein ernstzunehmendes Problem in den GRACE-Daten darstellt. Das Problem kann in Zukunft noch gravierender werden durch die verbesserte Technologie der Bordinstrumente, z.B. durch den Wechsel im Ranging-System von Mikrowellen im K-Band zur Lasertechnologie, wie dies derzeit in der GRACE-Follow-On Mission getestet wird und was in zukünftigen Missionen weitere Verwendung finden soll.

Obwohl dieses Problem viel Aufmerksamkeit auf sich zieht, ist das Verständnis vom Aliasing der Ozeangezeiten in der Satellitengravimetrie ungenügend. In Anbetracht davon werden in dieser Arbeit

- die Mechanismen des Aliasing der Ozeangezeiten systematisch herausgearbeitet,
- die gefundenen Mechanismen analytisch oder numerisch aufgezeigt,
- die entwickelten Methoden zur Reduzierung des Gezeitenaliasing in der Datennachbearbeitung eingesetzt,
- und Vorschläge für den Entwurf zukünftiger Missionen gemacht, in denen das Aliasing der Ozeangezeiten verringert werden soll.

Insbesondere wird in der Arbeit ein Zwei-Schritt Mechanismus des Aliasings für die Satellitengravimetrie herausgearbeitet. Der primäre Aliasingeffekt stammt aus der zu geringen Abtastung des Orbits, welche durch die Präzession der Orbitebene vorgegeben ist. Die periodischen Muster der

Beobachtungen entlang des Orbit zeigen ebenfalls die primären Aliasingperioden. Diese Muster geben auch die Abtastung der Phase der Ozeangezeiten durch den Orbit wieder, was für den verbesserten Entwurf der zukünftiger Satellitenmissionen eingesetzt werden kann.

Ein sekundäres Aliasing folgt aus der zu geringen Abtastung des primären Aliasingeffekts in der Schwerefeldbestimmung. Die Bestimmung der Schwerefeldparameter ist ein Prozess, in welchem die Beobachtungen und die Funktionale des Schwerepotentials in Zeit oder Raumbereich kombiniert werden. Geophysikalische Signale werden dabei innerhalb des Lösungszeitraums auf verschiedene räumlichen Skalen gemittelt. Im Allgemeinen kann jede bestimmte Lösung als eine Stichprobe der Realität betrachtet werden. Daher ergibt sich ein sekundäres Aliasing, wenn die primäre Aliasingperiode und die Periode der zeitlichen Lösung nicht das Nyquist-Abtasttheorem berücksichtigen. Das sekundäre Aliasing kann durch die spektrale Analyse der bestimmten Lösungen aufgezeigt werden.

Primäre und sekundäre Aliasingperioden sind eindeutig unter der Bedingung, dass die Bodenspuren innerhalb des Lösungszeitraum für eine vorgegebene räumliche Skala homogen verteilt sind und außerdem konsistent für alle Zeitintervalle der Lösung. Ist dies nicht der Fall, so werden zusätzliche Aliasingfrequenzen erkennbar.

Das Aliasingverhalten für die einzelnen Gezeitenkomponeten wird für GRACE-ähnliche Formationen und für Bender-ähnliche Satellitenkonstellationen untersucht. Die Aliasingperioden der Bender-ähnlichen Konstellation setzt sich aus den Aliasingperioden der einzelnen Satellitenpaare zusammen. Daher kann man das Aliasing einer kombinierten Konstellation auch unabhängig als einzelne Paare betrachten und es wird keine spezielle Behandlung für die Überlagerung notwendig.

Die Fehler durch das Aliasing der Ozeangezeitem können deutlich verringert werden durch die spektrale Kleinste-Quadrate-Schätzung der Aliasingfrequnzen in der Nachbearbeitung der Daten. Im Allgemeinen betrifft das primäre Aliasing die sphärisch-harmonischen Koeffizienten im ganzen Spektralbereich, während das sekundäre Aliasing vor allem die zonalen und die tesseralen Koeffizienten der niedrigen Ordnung betrifft. Das Aliasing ist zwar nicht mit den Streifenmustern der GRACE-Lösungen korreliert, aber die Entfernung der Aliasingfehler reduziert gleichzeitig die Streifenfehler.

Gemäß der Abtastung der Ozeangezeiten bezüglich der Phasenlage durch die Orbitgeometie, werden die optimale Trennungen der Knotenlinien für Doppel- und Dreifach-Paare-Konstellationen bezüglich der einzelnen Gezeitenkomponenten untersucht. Eine Konstellation kann dabei das Aliasing durch die Geometrie reduzieren, indem man einem „out-of-phase“ Abtastkriterium folgt. Da jede Gezeitenkomonente eine andere Frequenz hat, differenzieren auch die optimale Trennungen der Knotenlinien für jede Komponente. Daher ist es notwendig, einen Kompromiss für die verschiedenen Ziele zu finden.

Acronyms

AO	atmosphere and non-tidal ocean.
BD	Bender-type de-aliasing.
BR	Bender-type recovery.
CHAMP	Challenging Minisatellite Payload.
D1	de-aliasing with respect to primary aliasing periods.
D12	de-aliasing with respect to primary and secondary aliasing periods.
D12S	de-aliasing with respect to primary and secondary aliasing periods and de-striping.
D12SAS	de-aliasing with respect to the primary aliasing frequencies, secondary aliasing frequencies and side frequencies.
D12SASS	de-aliasing with respect to the primary aliasing frequencies, secondary aliasing frequencies, side frequencies and de-striping.
D2	de-aliasing with respect to secondary aliasing periods.
DS	de-striping.
DSAM	de-aliasing with respect to the main frequencies of spectral analysis.
DSAM1	de-aliasing with respect to the main frequencies and primary aliasing frequencies.

DSAM1S	de-aliasing with respect to the main frequencies, primary aliasing frequencies and side frequencies.
GD	GRACE-type de-aliasing.
GOCE	Gravity Field and Steady-State Ocean Circulation Explorer.
GR	GRACE-type recovery.
GRACE	Gravity Recovery and Climate Experiment.
JPL	Jet Propulsion Laboratory.
ll-SST	low-low satellite to satellite tracking.
PSD	power spectral density.
RF	recovered field.
SBASA	simulation-based aliasing spectral analysis.
T/P	Topex/Poseidon.
UT	Universal Time.

CHAPTER 1

INTRODUCTION

Time and tide wait for no man.

1.1 Aliasing

IN signal processing and other related disciplines, *aliasing* has two meanings: (1) an effect that results in *indistinguishable* signals when sampled; (2) the *distortion* or *artefact* when the reconstructed signal from samples is different from the original continuous signal. Generally speaking, aliasing happens when the signal is undersampled. According to the Nyquist-Shannon sampling theorem[1], if a signal $y(t)$ contains no frequencies higher than B hertz, it is completely determined by giving its ordinates at a series of points spaced $1/(2B)$ seconds apart (Nyquist 1928; Shannon 1949). In other words, for a given sample rate f_s, undistorted reconstruction is guaranteed for the band-limit $B < f_s/2$. Otherwise, if the signal $y(t)$ contains frequencies equal to or larger than half the sample rate $f_s/2$, aliasing occurs when reconstructing the original signal based on the samples. The two thresholds, $2B$ and $f_s/2$ are called the *Nyquist rate* and *Nyquist frequency*, respectively, which should not be confused with each other. In the context of the aliasing problem, Nyquist rate is the lower bound for the sample rate for alias-free signal sampling. The Nyquist frequency is half of the sampling rate of a discrete signal processing system, also

[1] The name *Nyquist-Shannon sampling theorem* honors Harry Nyquist and Claude Shannon. The theorem was also discovered independently by E.T. Whittaker, by Vladimir Kotelnikov, and by others.

Harry Nyquist (1889–1976), Swedish-born American electronic engineer, made important contributions to communication theory.

Claude Elwood Shannon (1916–2001), American mathematician, electrical engineer and cryptographer, known as "the father of information theory".

Edmund Taylor Whittaker (1873–1956), English mathematician.

Vladimir Aleksandrovich Kotelnikov (1908–2005), information theory and radar astronomy pioneer from the Soviet Union.

known as the folding frequency of a sampling system.

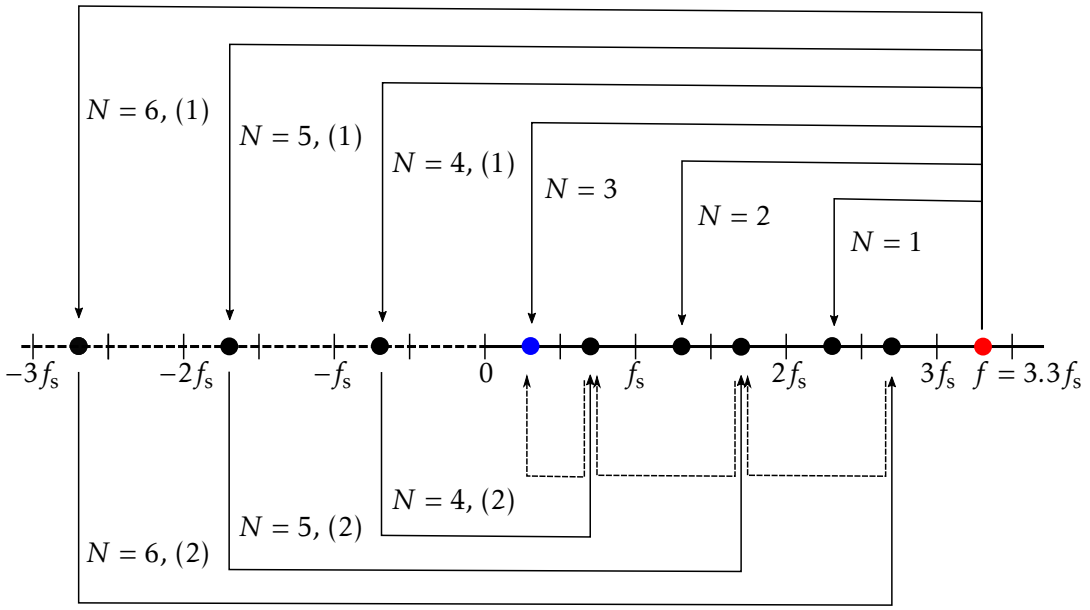

Figure 1.1: Aliasing mechanism. The abscissa is the frequency axis. f is the original signal frequency , which is marked by the red dot. f_s is the sampling frequency. The negative frequency axis is marked as dashed line because negative frequencies[2] help understanding equation (1.1) but are out of scope of this research. All the dots except for the red one are the aliases of frequency f, which can be derived by equation (1.1). The indices (1) and (2) refer to the operation *differencing* and *getting absolute value*, respectively, according to the equation (1.1). The blue dot indicates the aliased frequency of the frequency f detected by the sampling frequency f_s.

Aliasing can occur in signals sampled in time or in space, which is referred to as temporal aliasing and spatial aliasing, respectively. In reality, signals are commonly modelled as the superposition of sinusoids with different frequencies and different amplitudes, for instance with a Fourier series. Therefore, understanding aliasing of an individual sinusoid is important for understanding the aliasing of their sum, the real signals. Figure 1.2 shows the basic idea of aliasing when a sinusoid is sampled at different frequencies which are all no higher than twice the original frequency. In general, when a sinusoid of frequency f is sampled with frequency f_s, the resulting number of *cycles per sample* is $f_N = f/f_s$, which is also known as *normalized frequency*. When $f_N \geq 0.5$, aliasing occurs. The samples are indistinguishable from another sinusoid, called an alias, whose normalized frequency differs from f/f_s by any positive or negative integer. That is because adding an integer number of cycles to the samples of a sinusoid has no effect on their values. All the aliases of frequency f with respect to sampling frequency f_s can be expressed as

$$f_{\text{alias}}(N) = |f - N f_s|\,, \tag{1.1}$$

where N is integer with unit *cycles per sample*. When $N = 0$, $f_{\text{alias}} = f$ is the true frequency. Figure 1.1 shows the alias mechanism expressed by equation (1.1). Suppose the red dot indicates the original frequency, $f = 3.3 f_s$, of a sinusoid, each of the remaining dots at positive frequencies[2] indicates a possible alias of original frequency f given the sampling frequency f_s, while the blue dot indicates the alias frequency that is achieved. This example also shows a two-step procedure when $N = 4, 5, 6$ according to equation (1.1), that is: (1) differencing, and (2) getting absolute value.

One should notice that, if the signal frequency is unknown, the original frequency of the blue dot can be any of the dots, black or red in this example; if the original frequency is known, the alias frequency is unique given the sampling frequency, the blue in this example. The tide aliasing problem belongs to the second case.

In signal processing, aliasing is generally avoided by applying low-pass filters or anti-aliasing filtering to the analogue signal before sampling. Apart from the discussion above, two aspects should be emphasized, see Figure 1.2 for the examples:

i) aliasing not only causes frequency distortion, but may also cause amplitude distortion, e.g. scenario (A1), (A5), (B1) and (B5);

ii) sampling a signal at the same sampling rate at shifted lags (in time or in space) gives different amplitude distortion, c.f. scenario (A1) and (B1), or scenario (A5) and (B5).

1.2 Satellite gravimetry and ocean tide aliasing

Gravitational field of the Earth is important in many senses, such as providing the Earth's shape, defining the reference frame, indicating the mass distribution. In general, the global gravitational field can be expressed by spherical harmonic expansion as (e.g. Hofmann-Wellenhof and Moritz 2006)

$$V(r,\theta,\lambda) = \frac{GM}{R}\sum_{l=0}^{\infty}\left(\frac{R}{r}\right)^{l+1}\sum_{m=0}^{l}\left(\bar{C}_{lm}\cos(m\lambda) + \bar{S}_{lm}\sin(m\lambda)\right)\bar{P}_{lm}(\cos\theta) \tag{1.2}$$

in which

r, θ, λ = radius, co-latitude, longitude

G, M, R = gravitional constants, the Earth's mass, mean radius of the Earth

$\bar{C}_{lm}, \bar{S}_{lm}$ = fully normalized spherical harmonic coefficients of degree l and order m

$\bar{P}_{lm}(\cos\theta)$ = fully normalized Legendre function of degree l and order m,

[2] Negative frequencies are also alias frequencies of the original frequency. Negative frequencies are commonly used in some disciplines, in which the absolute value indicates the magnitude and the sign indicates the direction, for instance, a wheel rotating forwards or backwards can be modelled with positive and negative frequency. In this research, negative frequencies are out of the scope and ignored.

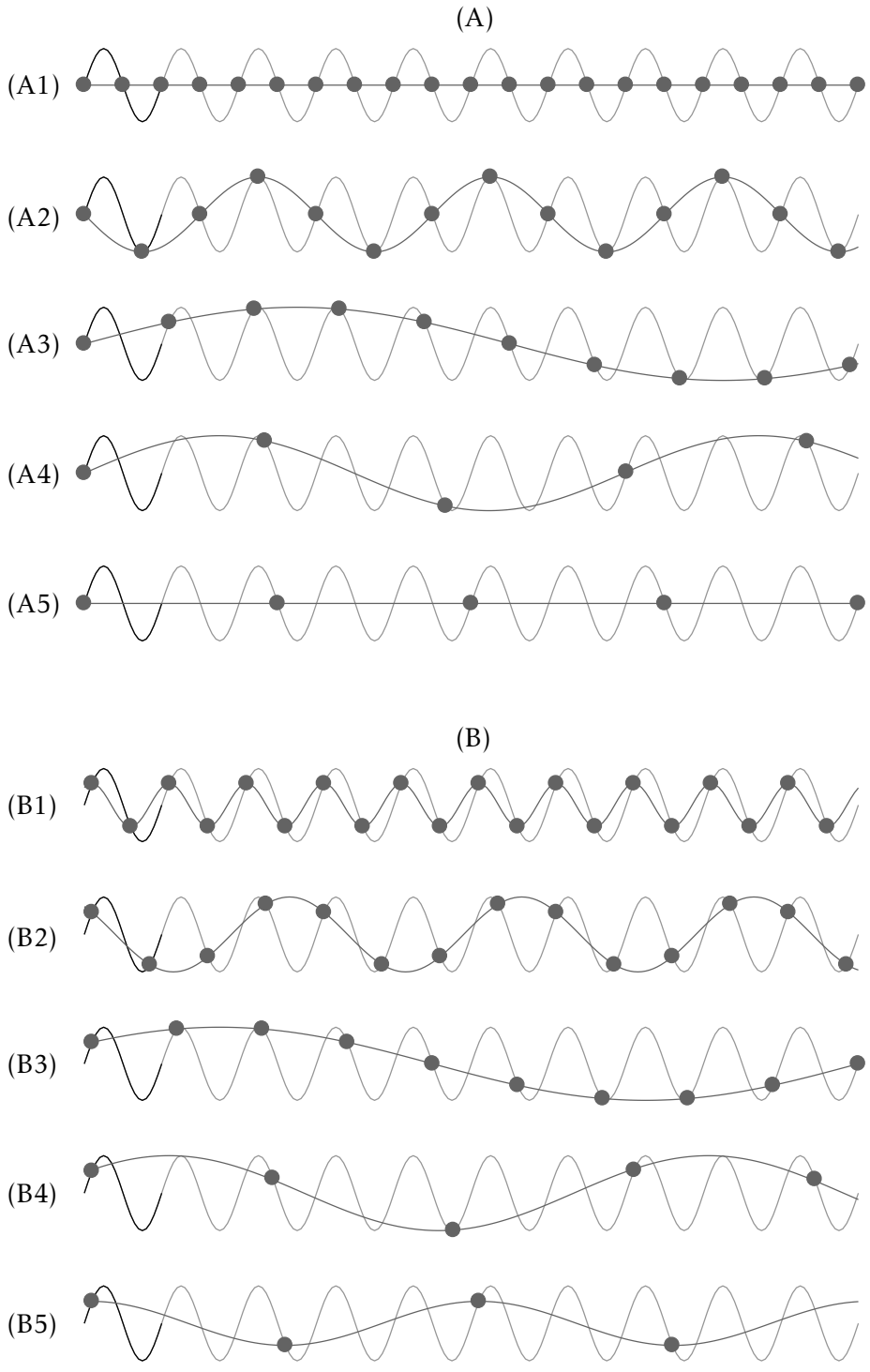

Figure 1.2: Aliasing examples of a sinusoid. The light grey wave with one black segment is the original signal and it is the same for all the scenarios (A1)–(B5). The black segment indicates one cycle. The dark grey dots are samples at different sampling rates. The dark grey line is the reconstruction from the samples. Every two corresponding scenarios in group (A) and group (B), for instance (A1) and (B1), have the same sampling rate but different time lags.

with normalization factor

$$N_{lm} = \sqrt{(2-\delta_{m0})(2l+1)\frac{(l-m)!}{(l+m)!}}. \tag{1.3}$$

The complex-valued expression of (1.2) is (e.g. Sneeuw 2000)

$$V(r,\theta,\lambda) = \frac{GM}{R}\sum_{l=0}^{\infty}\left(\frac{R}{r}\right)^{l+1}\sum_{m=-l}^{l}\bar{K}_{lm}\bar{Y}_{lm}(\theta,\lambda), \tag{1.4}$$

with normalized surface spherical harmonic of degree l and order m $\bar{Y}_{lm}(\theta,\lambda)$ defined as

$$\bar{Y}_{lm}(\theta,\lambda) = \bar{P}_{lm}(\cos\theta)e^{im\lambda}, \tag{1.5}$$

and the corresponding normalized spherical harmonic coefficients $\bar{K}_{lm}$ expressed in complex-valued quantities. The complex- and real-valued spherical harmonic coefficients have the relation

$$\bar{K}_{lm} = \begin{cases} (-1)^m\left(\bar{C}_{lm} - i\bar{S}_{lm}\right)/\sqrt{2}, & m>0 \\ \bar{C}_{lm}, & m=0 \\ \left(\bar{C}_{lm} + i\bar{S}_{lm}\right)/\sqrt{2}, & m<0 \end{cases}. \tag{1.6}$$

Note that the normalization factor of the complex-valued expression is different from (1.3) and one can find more details in (Sneeuw 2000). The complex conjugated of $\bar{Y}_{lm}(\theta,\lambda)$ and $\bar{K}_{lm}$ are: $\bar{Y}^*_{lm} = (-1)^m\bar{Y}_{l,-m}$ and $\bar{K}^*_{l,-m} = (-1)^m\bar{K}_{lm}$.

Since the beginning of the 21 century, the satellite gravity missions, i.e. Challenging Minisatellite Payload (CHAMP) (Reigber et al. 1999), Gravity Recovery and Climate Experiment (GRACE) (Tapley et al. 2004) and Gravity Field and Steady-State Ocean Circulation Explorer (GOCE) (Drinkwater et al. 2003), have innovatively enlarged our knowledge of the Earth's static and temporal gravity field. Among them, the GRACE mission has provided a wide application in the Earth sciences, such as terrestrial water storage (e.g. Rodell et al. 2009), ice sheets and glaciers (e.g. Luthcke et al. 2008), sea level (e.g. Leuliette and Miller 2009), solid Earth (e.g. Davis et al. 2004), earthquakes (e.g. Han et al. 2006). Because of the extraordinary performance of the GRACE mission, the successor GRACE Follow-On mission was planned and launched on May 22, 2018 to carry on the work of its predecessor. Additionally, it will test an intersatellite laser ranging instrument which has the potential to improve the precision of low-low satellite to satellite tracking (ll-SST) tracking dramatically (Sheard et al. 2012).

Several problems need special attention to derive reasonable gravity fields by satellite mission like GRACE, one of which is aliasing. In this work, *aliasing* specially refers to the effect caused by undersampling of the high frequency temporal signals such as ocean tides, atmosphere and non-tidal ocean (AO) signals. The aliasing of the spectrum from higher degree to lower degree *because of the real world complexity and inadequate sampling comparing to the infinity*, which was investigated by e.g. Han et al. (2002),

is not included in this discussion. Currently, the aliasing is dealt with by subtracting corresponding models, i.e. ocean tide model and AO model, before estimating the gravity field. This will certainly reduce the power of aliased signal, but will not prevent the aliasing mechanism itself. Therefore, the aliasing errors cannot be fully removed because of the uncertainty of the models. For instance, Thompson et al. (2004) and Han et al. (2004) showed that aliasing is a significant problem relative to GRACE measurement noise by using numerical oceanic and atmospheric models, and Schrama (2003) suggested that ocean tide models may contain errors that affect temporal gravity solutions derived by GRACE observations. Therefore, different efforts are still ongoing to improve the estimated gravity field by handling the aliasing problem. For example, Wiese et al. (2011) promoted a method of estimating low resolution gravity fields at short interval in order to mitigate the AO aliasing errors.

Ocean tide aliasing is a typical problem in satellite altimetry and the understanding and handling of it are sophisticated nowadays. However, as Schrama (2003) indicated, *"the aliasing problem for a gravity mission is far more difficult to comprehend than the way tidal modelling errors map along repeating Topex/Poseidon altimeter ground tracks"*. Nevertheless, ocean tide aliasing errors must be tackled because if the laser ranging testing is successfully demonstrated by GRACE Follow-On and is applied in a future ll-SST tracking mission, the ocean tide aliasing errors are expected to be two orders of magnitude larger than the gravity recovery error due to laser range observation noise (Flechtner et al. 2016). That is, ocean tide aliasing errors may become one of the major factors hindering the precision improvement of the gravity field solutions derived by the satellite missions. Furthermore, quite a few studies have observed tidal aliasing errors even from GRACE, which applied K-Band ranging for ll-SST (see the discussion below).

Many researchers have dealt with the ocean tide aliasing problem. Before the launch of the GRACE mission, Knudsen and Andersen (2002) estimated the aliasing frequency by *assuming the sampling interval as half a sidereal day*, and Knudsen (2003) revised the estimated alias frequencies comparing to the estimation in (Knudsen and Andersen 2002) by taking "the actual precession of the node" of GRACE into account. However, Ray et al. (2003) calculated the aliasing period by considering the orbit plane precession of the satellite with respect to the tide-raising body, without further explanation of how to do it. Somehow, they estimated the alias periods of five solar tides, namely K_2, K_1, S_2, S_1 and P_1, and claimed that the lunar tides could be hardly problematic (Ray et al. 2003). For some of the constituents, the aliasing periods do not coincide when comparing (Knudsen and Andersen 2002; Knudsen 2003) with (Ray et al. 2003).

Later on, Ray and Luthcke (2006) revised their estimation of the alias periods and tidal aliasing errors, and announced that total error budget of GRACE accepted at that time (2006) is roughly one order of magnitude larger than the aliasing errors arising from ocean tide modelling errors *except for the lowest degree*. Seo et al. (2008a) simulated the

ocean tide errors along the GRACE groundtracks using the GRACE level 1B data provided by Jet Propulsion Laboratory (JPL). They found that the M_2 alias period is about 140 days rather than the predicted 13.5 days because of the monthly sampling and K_1 has two alias periods of about 90 days and 7 years. Schrama and Visser (2007) estimated aliasing errors via simulated GRACE data and showed that the signals at periods shorter than 3 months were not well retrieved due to errors in geophysical background models. Seo et al. (2008b) investigated GRACE spatial aliasing errors due to errors in geophysical models, such as ocean tide models, by simulation. Tourian (2013) estimated the aliasing frequencies by using half a GRACE nodal day as the sampling period, discussed the effect of the recovery process on the aliasing magnitude and evaluated the tidal aliasing errors with respect to the residuals of GRACE monthly solutions.

Regarding the effect of ocean tide aliasing errors on *lower degree*, apart from the conclusion mentioned in (Ray and Luthcke 2006), Seo et al. (2008b) showed S_2 aliasing error to be a possible error source of $C_{2,0}$ of GRACE fields. This speculation was further confirmed in (Chen et al. 2009), which indicated the $C_{2,0}$ of RL04 solutions showing significantly larger S_2 aliasing errors than those from RL01 solutions. However, Cheng and Ries (2017) held the opposite opinion. They insisted that the unexpected 161 day signal in GRACE $C_{2,0}$ cannot be due to aliasing from the errors in the S_2 constituent. Special attention should be paid that Cheng and Ries (2017) took one of the tidal perturbation frequencies as the tidal aliasing frequency for each of the constituent.

Apart from the discussion on the aliasing frequency and error estimation, as well as the probable influence on the GRACE data and the derived gravity field solutions, the possible strategies to mitigate the ocean tide aliasing errors were also investigated by a few researchers. For instance, Visser et al. (2010) explored three methods, i.e. constellation design, temporal filtering of the time-series of the gravity field and spatial smoothing, to mitigate the ocean tide aliasing errors. Hauk and Pail (2018) provided a method to co-parametrize the ocean tides to mitigate their aliasing in the process of gravity field retrieval.

Another natural question is whether it is possible to estimate the ocean tides from missions like GRACE. Ray et al. (2003) discussed the sampling of tidal signals by GRACE and concluded that GRACE was never optimized for being able to observe the tidal signals as it was done by Topex/Poseidon (T/P) mission. However, Han et al. (2005) claimed that an unmodeled ice shelf ocean tide effect of M_2 and S_2 is detected underneath the Filchner-Ronne and Larsen ice shelves in the GRACE data. They detected it by looking at certain bands around the alias periods of corresponding tidal constituents. Han et al. (2007) derived the tidal solutions of three constituents by locally analysing the intersatellite tracking data from GRACE, and found that they were in good agreement with the in-situ measurements at several locations in Antarctica. Han et al. (2010) presented one centimeter-level observations of diurnal tides derived from the GRACE monthly solutions

relative to a prior ocean tide model GOT4.7. Mayer-Gürr et al. (2012) tried to derive a global ocean tide model by combining GRACE data and ocean tide model EOT08a, which led to a marginally improved new ocean tide model.

In view of all the research above, several problems still exist regarding the ocean tide aliasing in satellite gravimetry:

- the precise aliasing mechanism is unclear;
- the understanding of sampling frequency and aliasing frequency for gravity missions is different from study to study;
- the influence on individual spherical harmonic coefficients, especially the lower degree coefficients, should be further investigated;
- what is the difference between spatial aliasing and temporal aliasing?
- is there any take-away knowledge for future missions in case all the problems above are solved?

1.3 Objective and outline

Based on the discussion in the previous section, this work aims at solving the following problems:

1) clarifying the mechanism of the ocean tide aliasing in satellite gravimetry;

2) estimating the aliasing periods according to the aliasing mechanism and giving demonstrations;

3) understanding the influence of aliasing on the spherical harmonic coefficients;

4) reducing the aliasing errors via data processing;

5) mitigating the ocean tide aliasing errors through orbit design for the future missions.

This work starts with introducing the basic theory of the ocean tide, its modelling and expression in gravity field in Chapter 2. The introduction is not dedicated to cover all the topics related to ocean tides, but to briefly present the necessary preliminaries to understand ocean tides and following discussions.

Chapter 3 discusses the ocean tide aliasing mechanism in satellite gravimetry from different views. Firstly, the aliasing problems in satellite gravimetry and altimetry are compared and distinguished. Secondly, the relation between spatial aliasing and temporal aliasing is cleared up. Thirdly, a two-step tide aliasing mechanism is elaborated. Lastly, the relation between the orbit perturbation and aliasing is discussed.

In the subsequent Chapter 4, a spectral analysis method for detection of aliasing periods is proposed based on simulations. The aliasing spectrum is investigated regarding different regions, different spherical harmonic coefficients and different recovery periods. The influence of frequency interference on aliasing is discussed.

Chapter 5 deals with the ocean tide aliasing error reduction in post-processing. Aliasing error estimation regarding different aliasing periods is investigated in spatial and spectral domain. The influence of the aliasing on different spherical harmonic coefficients is discussed. Apart from that, the relation between striping and aliasing is examined.

In Chapter 6, the orbit design of future missions considering ocean tide mitigation is discussed. Possible double-pair and triple-pair constellations are investigated. Based on that, some suggestions are provided for ocean tide self-dealiasing.

Finally, Chapter 7 summarizes this work and discusses the prospects for future research.

CHAPTER 2

TIDAL THEORY AND MODELLING

OCEAN tides are important gravity signals which contribute to satellite gravimetry observations. In order to better understand the ocean tide signal and its role in the gravity recovery, a close look into tidal theory and tide modelling is needed. In this chapter, the tide-generating force and potential are introduced in section 2.1 and section 2.2. The harmonic expansion of the tide-generating potential is then discussed in section 2.3, which leads to astronomical tidal species and constituents. Next, a brief description of the equilibrium tide (section 2.4) is followed by a discussion of the real response of ocean, and tidal analysis (section 2.5). In the end, a few words about ocean tide modelling (section 2.6) and spherical harmonic analysis of tidal heights (section 2.7) are given. Figure 2.1 describes the relationship between different topics in this chapter.

2.1 Tide-generating force

ISAAC Newton's *Principia*(1687) gave the first correct theory for the tide generating forces, which are the differences between the Moon's (Sun's) gravitational attraction at certain location and at the Earth's center (Cartwright 1993). Here we take a simplified Sun-Earth system as an example, ignoring the fact that the orbit of the Earth around the Sun is elliptical and that the Earth rotation axis is inclined to the ecliptic, see Figure 2.2. Hereafter, a **bold** character in a formula indicates a *vector*.

Taking the Earth as a whole, the gravitational attraction $\mathbf{F_2}$ at the center of mass of the Earth is to keep the Earth in its orbit around the Sun. The corresponding force per unit mass is $\mathbf{a}_r = \mathbf{F}_2/M_E$, in which M_E is the entire mass of the Earth. For an arbitrary mass M_a on the side of the Earth towards the Sun, the attraction $\mathbf{F_1}$ is greater than $M_a\mathbf{a}_r$ as it is closer to the Sun. Since the Earth is not a rigid body, the Earth deforms towards the

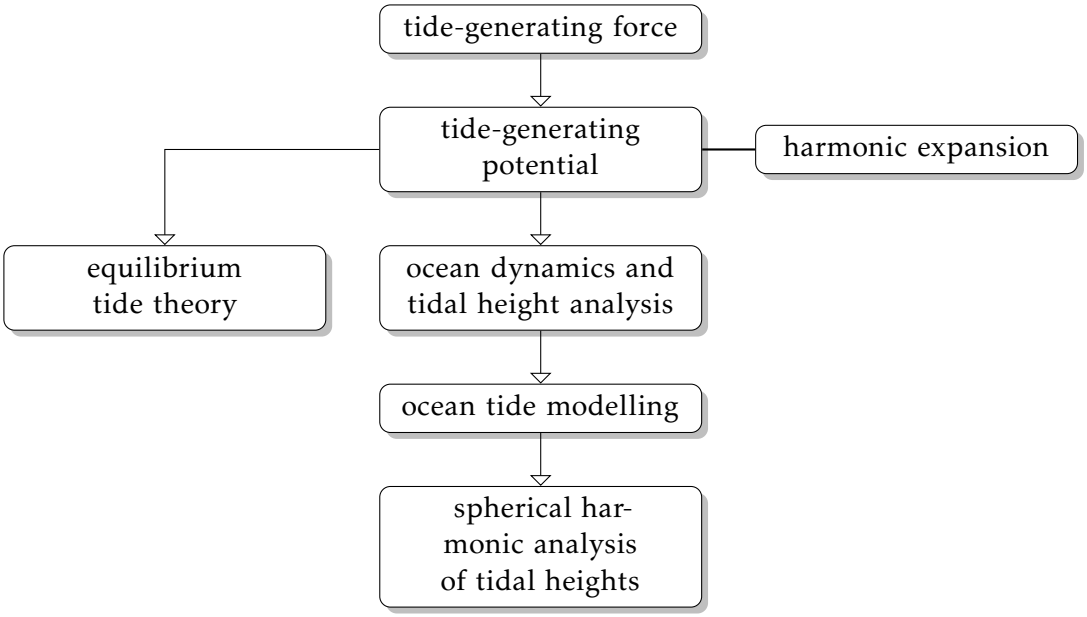

Figure 2.1: The relationship of the topics discussed in Chapter 2.

Sun. The deformation effect of water is more significant than that of solid Earth, as the water is more flowable than the solid Earth. For an arbitrary mass M_a on the opposite side of the Earth, the gravitational force $\mathbf{F_3}$ is smaller than $M_a\mathbf{a}_r$. Therefore, the mass on this side of the Earth, especially the water, deforms away from the Sun. To summarize, the tide-generating forces are the differences between the gravitational attraction at the center of the Earth and at the target points, which vary according to the distances from the Sun, that is,

- $\mathbf{D_1} = \mathbf{F_1} - M_a\mathbf{a}_r$, directed towards the Sun,
- $\mathbf{D_3} = \mathbf{F_3} - M_a\mathbf{a}_r$, directed away from the Sun.

All the **D**s form an envelope of the tide-generating forces, see the grey shadow in Figure 2.2. It should be reminded that this symmetrical egg-shaped figure is only for the solid Earth but *not* the tidal bulge of the ocean. It is the inflation that the tide-generating bodies *try* to make in the ocean waters but never realize exactly because of many factors, i.e., restriction of wave speed, irregular depths, presence of continents, bottom friction, turbulence, and viscosity (Hicks and Szabados 2006).

The Moon-Earth system essentially gives the same pattern of tide-generating forces as the Sun-Earth system, except for magnitudes.

According to Newton's law of gravitation, the attraction of the tide-generating body B on a particle P on the Earth's surface is given by

$$\mathbf{F}_{PB}(P) = GM_PM_B\frac{\mathbf{r}_P}{r_P^3}, \tag{2.1}$$

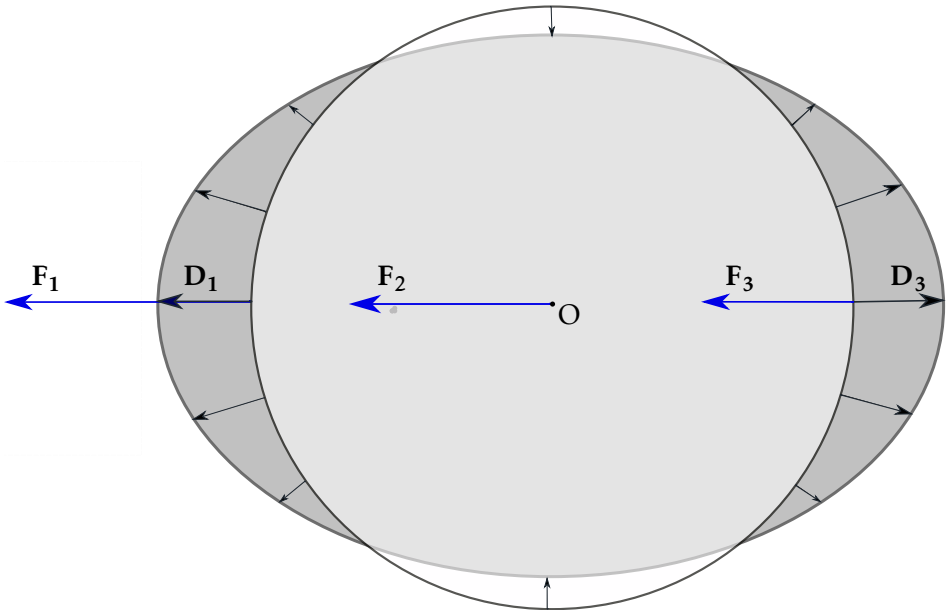

Figure 2.2: The envelope of tide generating forces.

in which G is the universal gravitational constant, M_P and M_B are the mass of P and B, $\mathbf{r}_P$ is the radial vector from P to body B, and r_P is its magnitude (see Figure 2.3). Integrating all the Ps on the Earth donates the force $\mathbf{F}_{OB}$, the same as $\mathbf{F}_2$ in Figure 2.2, which assuming the entire mass M_E of the Earth concentrated at the center of the Earth O:

$$\mathbf{F}_{OB} = GM_E M_B \frac{\mathbf{r}_B}{r_B^3}, \tag{2.2}$$

where $\mathbf{r}_B$ is the radial vector from the Earth center O to the body B. The corresponding $\mathbf{F}_{OB}$ component on point P is

$$\mathbf{F}_{OB}(P) = GM_P M_B \frac{\mathbf{r}_B}{r_B^3}, \tag{2.3}$$

and the difference of (2.1) and (2.3) deforms the Earth and produces the tide-generating force $\mathbf{F}_t$ (**D** in Figure 2.2) at P:

$$\mathbf{F}_t = \mathbf{F}_{PB}(P) - \mathbf{F}_{OB}(P) = GM_P M_B \left(\frac{\mathbf{r}_P}{r_P^3} - \frac{\mathbf{r}_B}{r_B^3} \right). \tag{2.4}$$

2.2 Tide-generating potential

The tidal acceleration $\mathbf{a}_t = \mathbf{F}_t / M_P$, also known as force per point mass, can be derived from a tide-generating potential V_t by:

$$\mathbf{a}_t = \nabla V_t, \tag{2.5}$$

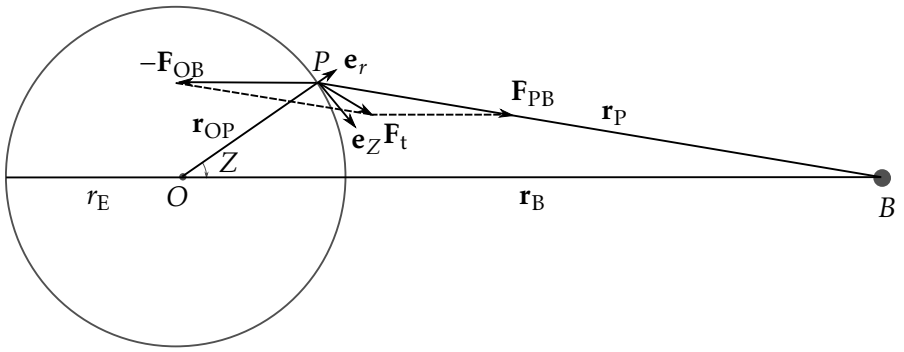

Figure 2.3: The tide-generating force.

where ∇ is the gradient operator. The component of $\mathbf{a}_{\mathrm{t}}$ along the vertical and horizontal axes $\mathbf{e}_r$ and $\mathbf{e}_Z$ respectively in Figure 2.3 are

$$\begin{aligned} \mathbf{a}_r &= \frac{\partial}{\partial r} V_{\mathrm{t}} \\ \mathbf{a}_{\mathrm{Z}} &= -\frac{\partial}{r\partial Z} V_{\mathrm{t}} \,. \end{aligned} \tag{2.6}$$

where Z is the zenith angle of the tide-generating body B (see Figure 2.3 and Figure 2.4). It should be reminded that the *vertical* component of the tide generating forces plays no role in generating tidal elevations (Smith 1999). The horizontal force $\mathbf{a}_Z$ is responsible for tides rather than the vertical force $\mathbf{a}_r$, as it is always easier to *push* than to *lift* an object.

According to (2.2), the potential at the center of the Earth due to tide-generating body B is

$$V_{\mathrm{t}}(O) = \frac{GM_{\mathrm{B}}}{r_{\mathrm{B}}^2} r_{\mathrm{OP}} \mathrm{cos}Z + C \,, \tag{2.7}$$

where r_{OP} is the radius at the point P, and C is an arbitrary constant. Then the tide-generating gravitational potential at P is

$$V_{\mathrm{t}}(P) = \frac{GM_{\mathrm{B}}}{r_{\mathrm{P}}} - \frac{GM_{\mathrm{B}}}{r_{\mathrm{B}}^2} r_{\mathrm{OP}} \mathrm{cos}Z \,. \tag{2.8}$$

Note that the force on the Earth as a whole, namely (2.2), is balanced by the centrifugal force due to the motion of the Earth about the common center of mass between the Earth and tide-generating body.

In the triangle $\triangle POB$ (Figure 2.3), the following relationship holds $r_{\mathrm{P}}^2 = r_{\mathrm{B}}^2 - 2r_{\mathrm{OP}} r_{\mathrm{B}} \mathrm{cos}Z +$

r_{OP}^2 . Hence

$$\frac{1}{r_P} = \frac{1}{r_B}\left(1 - \frac{2r_{OP}}{r_B} + \frac{r_{OP}^2}{r_B^2}\right)^{-\frac{1}{2}} = \frac{1}{r_B}\sum_{l=0}^{\infty}\left(\frac{r_{OP}}{r_B}\right)^l P_l(\cos Z), \tag{2.9}$$

in which $P_l(x)$ is the Legendre polynomial of degree l, with $P_0(x) = 1$, $P_1(x) = x$ and $P_2(x) = (3x^2 - 1)/2$. Inserting (2.9) into (2.8) gives

$$V_t(P) = \frac{GM_B}{r_B}\left[1 + \sum_{l=2}^{\infty}\left(\frac{r_{OP}}{r_B}\right)^l P_l(\cos Z)\right], \tag{2.10}$$

The constant GM_B/r_B can be ignored because it generates no force according to (2.5). The $l = 1$ term corresponds to a uniform force field with strength $F = GM_BM_P/r_P^2$, and is compensated by the centrifugal force. For the Moon, $0.0157 \leq r_{OP}/r_B \leq 0.0180$ and for the Sun $r_{OP}/r_B \backsim 10^{-4}$. Thus the potential may be truncated after $l = 2$. Therefore, the principal tide-generating potential at arbitrary P becomes

$$V_t(P) = \frac{GM_B}{r_B}\left(\frac{r_{OP}}{r_B}\right)^2 P_2(\cos Z). \tag{2.11}$$

Hereafter, the subscript t and location indicator P are omitted for simplification, namely $V_t(P)$ is written as V.

2.3 Harmonic expansion of tidal potential: tidal species and constituents

The (apparent) movements of the Sun and the Moon are not along the equator, but in the orbital planes inclined to it. Therefore, the direction of the tidal bulge changes according to the declination of the tide-generating body in its orbit. Thus, it is more convenient to express the tidal potential in geographical coordinates: latitude and longitude of the observer on the Earth and the apparent longitude and latitude of the tide-generating body. For the spherical triangle $\triangle NBP$ (see Figure 2.4), the following relationship holds:

$$\cos Z = \sin\phi\sin\delta + \cos\phi\cos\delta\cos H. \tag{2.12}$$

The angle $\lambda - \lambda_B$ is called the hour angle H of the tide-generating body B, which is measured from the observer's local meridian positive to the west of the observer.

Inserting (2.12) into (2.13) gives the principal part of the tide-generating potential in geographic coordinates (Doodson 1921):

$$V(\lambda,\phi) = \frac{3GM_Br_{OP}^2}{4r_B^3}\left[\left(\frac{1}{3} - \sin^2\phi\right)\left(1 - 3\sin^2\delta\right) + \sin 2\phi\sin 2\delta\cos H + \cos^2\phi\cos^2\delta\cos 2H\right]. \tag{2.13}$$

The first term in the square bracket in (2.13) has no dependence on the hour angle H, and gives rise to a long-period potential. The second term forms a diurnal potential and

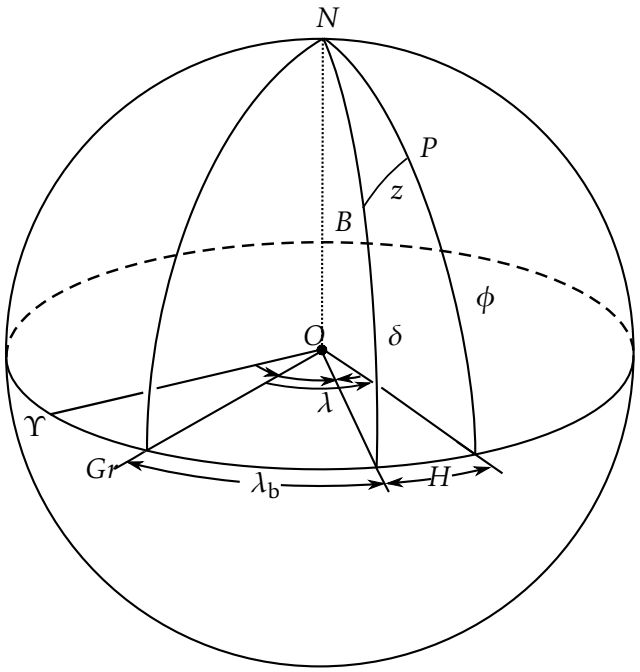

Figure 2.4: The geographical coordinates of the tide-generating body and an observing point P on the Earth. Here λ and ϕ are the geographic longitude and latitude of P. z is the angle between the observer at P and tide-generating body B, the same as in Figure 2.3. λ_b and δ are the apparent longitude and latitude (declination) of the body B with respect to the Greenwich and equator plane accordingly. *Gr* stands for the Greenwich meridian. Υ is vernal equinox, the intersection point of equator and ecliptic while the Sun travels northward. H is the hour angle of the tide-generating body B with respect to observer P. N stands for the north pole.

the last term indicates a semi-diurnal potential. In reality, the declination δ and orbital distance r_B vary in time. The declination changes over time because the ecliptic or the Moon's orbit plane around the Earth is tilted to the equator plane. The varied orbital distance is due to elliptical orbit of the Moon around the Earth or the Earth around the Sun. For more details, please refer to e.g. (Doodson 1921), (Smith 1999) and (Hicks and Szabados 2006).

Variations of declination and distance to the tide-generating bodies change the potential in (2.13). These variations can be expanded in a Fourier series and result in (1) the long-period tides, and (2) the diurnal and semi-diurnal tides with the modulations of basic tidal frequencies: the diurnal and semi-diurnal. To express the tide-generating potential

into its harmonics, (2.13) can be written as:

$$V(\lambda,\phi)=\left(\frac{\bar{r}_{\mathrm{B}}}{r_{\mathrm{B}}}\right)^3\left[G_{\mathrm{B}}^{(0)}(1-3\sin^2\delta)+G_{\mathrm{B}}^{(1)}\sin 2\delta\cos H+G_{\mathrm{B}}^{(2)}\cos^2\delta\cos 2H\right], \tag{2.14}$$

in which $\bar{r}_{\mathrm{B}}$ is the mean distance between the tide-generating body and the Earth. The superscript m on the $G_{\mathrm{B}}^{(m)}$ stands for the tidal species, namely $m=0$ for long-period tides, $m=1$ for diurnal tides and $m=2$ for semi-diurnal tides. G_{B} is the general coefficient and defined as:

$$G_{\mathrm{B}}=\frac{3GM_{\mathrm{B}}r_{\mathrm{OP}}^2}{4\bar{r}_{\mathrm{B}}^3}, \tag{2.15}$$

in which the subscript B stands for the tide-generating body. For the Moon and the Sun, the general coefficients are usually labelled as G and G_{s}, respectively. G is also known as Doodson's tidal constant (Doodson 1921). The general coefficients appear in the terms $G_{\mathrm{B}}^{(m)}$ in (2.15). These terms, which also involves the observer's latitude ϕ, are called Doodson's geodetic coefficients (of degree $l=2$) (Doodson 1921). In case of the Sun, they will be denoted by $G_{\mathrm{s}}^{(m)}(\phi)$, and in case of the Moon by $G^{(m)}(\phi)$. For the Moon, the geodetic coefficients for $l=2$ read:

$$\begin{aligned}
G^{(0)}(\phi)&=G\left(\frac{1}{3}-\sin^2\phi\right)\\
G^{(1)}(\phi)&=G\sin 2\phi\\
G^{(2)}(\phi)&=G\cos^2\phi\,.
\end{aligned} \tag{2.16}$$

The expressions of the geodetic coefficients of the Sun can be derived by replacing G by G_{s} in (2.16).

The harmonic expansion of the tidal potential is to expand the function (2.14), which depends on $\bar{r}_{\mathrm{b}}/r_{\mathrm{b}}$, δ and H, into a series of harmonics. In order to make the harmonic coefficients being relative comparable, all the coefficients of the harmonic expansion should be normalized with respect to the same quantity, taking G in this case. Therefore, we can rewrite the geodetic coefficients of the Sun as G_{s}/G times the geodetic coefficients of the Moon, namely G, and absorb the factor G_{s}/G in the coefficients of the solar harmonics (Doodson 1921). Finally, the tidal-generating potential of the Moon and the Sun given in (2.14) is written to a form

$$V(\lambda,\phi)=V_0(\lambda,\phi)+V_1(\lambda,\phi)+V_2(\lambda,\phi), \tag{2.17}$$

with

$$V_m(\lambda,\phi)=G^{(m)}(\phi)\sum_k\left|\eta_k\right|\cos\left(\Theta_k(t)+\chi_k+m\lambda\right), \tag{2.18}$$

where $G^{(m)}(\phi)$ are the geodetic coefficients of the Moon and $m=0,1,2$. η_k are the coefficients of the harmonic expansion, which contains G_{s}/G in case of solar harmonics. The

summation over k is over all harmonic terms of the tidal species. The arguments $\Theta_k(t)$ are the astronomical arguments or Doodson arguments at *Greenwich*, defined as

$$\Theta_k(t) = A\tau + Bs + Ch + Dp + EN' + Fp_s\,, \tag{2.19}$$

where $A-F$ are integer numbers, τ is Greenwich mean lunar time and (s,h,p,N,p_s) are five fundamental angles, cf. Table 2.1 and Figure 2.5. N' is by definition the negative of N in order to make all the angles increasing eastward. $\Theta_k + m\lambda$ is called the local argument. χ_k is the Doodson-Warburg phase correction (Cartwright and Edden 1973; Dow 1988; Petit and Luzum 2010), defined by

$$\chi_k = \begin{cases} 0 & \text{for semi-diurnal and long-period tides} \\ \pi/2 & \text{for diurnal tides with } \eta_k > 0\text{, e.g. } K_1 \\ -\pi/2 & \text{for diurnal tides with } \eta_k < 0\text{, e.g. } O_1, P_1, Q_1 \end{cases}. \tag{2.20}$$

Table 2.1: Fundamental angles.

symbol	definition	period
s	mean longitude of the Moon	27.32 mean solar days
h	mean longitude of the Sun	365.24 mean solar days
p	mean longitude of the lunar perigee	8.85 tropical years
N	mean longitude of the lunar node	18.61 tropical years
p_s	mean longitude of the solar perigee	21 000 tropical years

These fundamental angles (s,h,p,N',p_s) describe the long-term motion of the Sun and the Moon, which means periodic variations of the motion are excluded. The expressions are given as follows (Doodson 1921), the origin of time is taken as midnight at Greenwich on 1 January, 1900:

$$\begin{aligned} s &= 277°.0248 + 481267°.8906T + 0°.0020T^2 + \ldots \\ h &= 280°.1895 + 36000°.7689T + 0°.0003T^2 + \ldots \\ p &= 334°.3853 + 4069°.0340T - 0°.0103T^2 + \ldots \\ N' &= 100°.8432 + 1934°.1420T - 0°.0021T^2 + \ldots \\ p_s &= 281°.2209 + 1°.7192T + 0°.0005T^2 + \ldots, \end{aligned} \tag{2.21}$$

in which T is in Julian centuries counting from 1 January 1900, 0 hour Universal Time (UT)[1]. All these angles are longitudinal angles and measured with respect to the vernal equinox in the ecliptic. The angles are corresponding to five fictitious bodies moving along the ecliptic with speeds $\dot{s}$, $\dot{h}$, $\dot{p}$, $\dot{N}'$ and $\dot{p}_s$ accordingly. For instance, the mean longitude of the Sun h represents the longitude of a fictitious Sun moving in the ecliptic plane at an angular speed of 360° per 365.24 mean solar day. Mean solar time and mean

[1] The Universal Time, also known as mean solar time, is civil time based on the motion of the mean Sun, see exact definition of the mean Sun and mean solar time in the text.

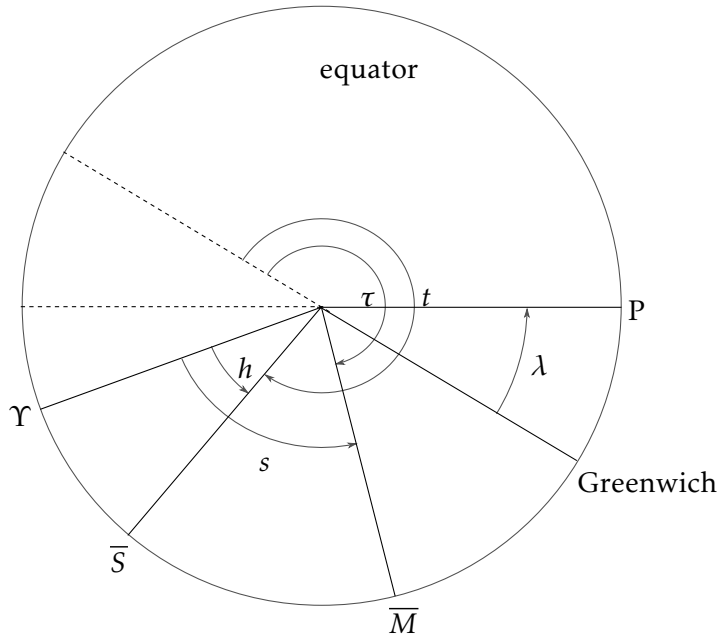

Figure 2.5: Mean solar time and mean lunar time. Mean Sun $\overline{S}$ and mean Moon $\overline{M}$ define the mean solar time and mean lunar time, respectively, which denoted by Greenwich mean solar time t and Greenwich mean lunar time τ. Similarly, $t+\lambda$ is local mean solar time and $\tau+\lambda$ is local mean lunar time, in which λ is the longitude of observer location P. s and h are mean longitude of Moon and Sun, respectively, which refer to the vernal equinox Υ.

lunar time are defined by the mean Sun and mean Moon, respectively, see Figure 2.5. The mean Sun is defined to move along the *equator* with a *constant speed* $\dot{h}$ the same as the fictitious Sun in the *ecliptic* at a certain reference epoch. The speed $\dot{h}$ can be considered as *constant* because the variations of $\dot{h}$ is about $0°.0006$/century per century according to (2.21), which is negligible over centuries. The time elapsed between two successive passages of the mean Sun at the Greenwich meridian is called a mean solar day. The time between successive passages of the mean Sun at the vernal equinox is called a tropical year, which contains 365.24 mean solar days. Similarly, the mean Moon is defined to travel in the equatorial plane with a nearly constant speed $\dot{s}$ at certain reference epoch. A mean lunar day is the time between successive passages of the mean Moon at the Greenwich meridian, which equals 1.035 mean solar days. Figure 2.6 shows the relationship among the Earth, the Moon and the Sun, with the Earth being the center of the celestial Sun-Earth-Moon system. The mean Sun and mean Moon are the projection of the Sun and the Moon to the equatorial plane travelling with constant speed.

According to Figure 2.5, a relation between mean solar time and mean lunar time holds as follows:

$$\tau = t - s + h. \tag{2.22}$$

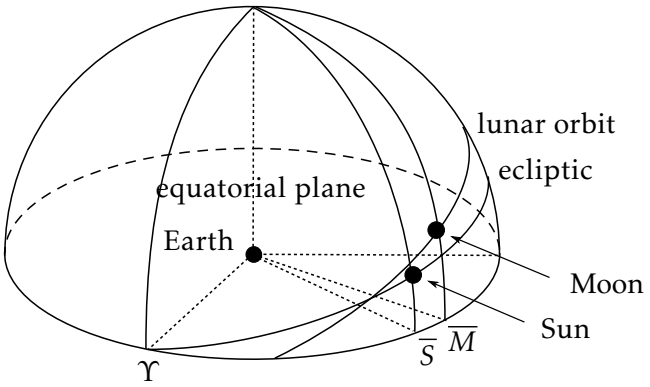

Figure 2.6: The Sun-Earth-Moon system. $\overline{S}$ and $\overline{M}$ are mean Sun and mean Moon, respectively, which are the same as shown in Figure 2.5.

Doodson number and tidal constituents A tidal constituent is one of the harmonic elements in the mathematical expression for the tide-generating potential. Doodson (1921) introduced a systematic notation for classifying the tides. Before Doodson, Darwin (1883) had given the harmonic expansion of the tide-generating potential which had been universally used and had been of remarkable value. The discrepancies between prediction and observation were serious at Darwin's time and had been attributed to *harmonic constants* (Doodson 1921). There was a residue composed of constituents which were not included in Darwin's schedule when all the "Darwinian constituents" were removed from the tidal height. Therefore, Doodson tried to make a more thorough development of the potential. In Doodson's notation, each tide harmonic is denoted by a 6-digit number which is known as the Doodson number, $k = k_1k_2k_3.k_4k_5k_6$. The Doodson number is obtained by adding 055.555 to the integer argument number $ABC.DEF$ in (2.19), that is

$$k_1k_2k_3.k_4k_5k_6 = A(B+5)(C+5).(D+5)(E+5)(F+5). \tag{2.23}$$

As the integers $A-F$ are rarely outside the range $[-4,4]$, adding 055.555 to the argument number avoids the Doodson number being negative values as much as possible (Doodson 1921). Inserting (2.23) into the Greenwich astronomical argument (2.19) gives

$$\Theta_k(t) = k_1\tau + (k_2-5)s + (k_3-5)h + (k_4-5)p + (k_5-5)N' + (k_6-5)p_s, \tag{2.24}$$

which is equivalent to

$$\Theta_k(t) = \dot{\Theta}_k t + \Theta_k(t_0). \tag{2.25}$$

$\dot{\Theta}_k$ is tidal frequency and $\Theta_k(t_0)$ is the Greenwich astronomical argument at initial epoch t_0. Then

$$\dot{\Theta}_k = k_1\dot{\tau} + (k_2-5)\dot{s} + (k_3-5)\dot{h} + (k_4-5)\dot{p} + (k_5-5)\dot{N}' + (k_6-5)\dot{p}_s, \tag{2.26}$$

and

$$\Theta(t_0) = k_1\tau(t_0)+(k_2-5)s(t_0)+(k_3-5)h(t_0)+(k_4-5)p(t_0)+(k_5-5)N'(t_0)+(k_6-5)p_s(t_0). \tag{2.27}$$

The index k_1 corresponds to the species index m. According to Doodson (1921), the term *constituent* is referred and restricted to a set of harmonics inseparable within a year. In other words, *constituent* indicates those harmonics whose arguments differ by multiples of h, but not by multiples of p, N' and p_s, which is unable to distinguish using one year's observation. Therefore, the first three figure of the argument-number is called *constituent-number*, and the first two figures of the argument-number is called *group-number*. The following gives an example:

- argument-number: 255.555, M_2 harmonic,
- constituent-number: 255, M_2 constituent,
- group-number: 25, M_2 group,
- species-number: 2, semi-diurnal.

However, certain symbols such as M_2, S_2 established by Darwin, as shown in the above example, are still used. A list of Darwin's symbols and the corresponding Doodson constituent number was given in Doodson (1921) Table VI. Table 2.2 shows part of tide constituents (Doodson 1921; Hicks et al. 2000). Hereafter, the term *constituent* is used by following Darwin's notation, which, to be precise, means corresponding tide harmonic in the context of Doodson (1921) without further explanation. In reality, it is not necessary to go any further than the constituent level so that a year worth of tide gauge data can be used to define amplitude and phase of a constituent (Schrama 2011). Nodal modulation factors are needed to be defined to properly define the amplitude and phase of a constituent.

Table 2.2: Tide constituents in both notation.

tidal species	constituent	Darwin	Doodson	period (hr)
long period	solar annual	S_a	056.555	8765.812 551 9
	solar semi-annual	S_{sa}	057.555	4382.905 208 7
	lunar monthly	M_m	065.455	661.309 204 9
	lunisolar fortnightly	M_f	075.555	327.858 968 9
diurnal	larger lunar elliptic diurnal	Q_1	135.655	26.868 356 7
	lunar diurnal	O_1	145.555	25.819 341 7
	solar diurnal	P_1	163.555	24.065 890 2
	lunisolar diurnal	K_1	165.555	23.934 469 7
semi-diurnal	larger lunar elliptic semi-diurnal	N_2	245.655	12.658 348 2
	principal lunar semi-diurnal	M_2	255.555	12.420 601 2
	principal solar semi-diurnal	S_2	273.555	12.000 000 0
	lunisolar semi-diurnal	K_2	275.555	11.967 234 8

2.4 The equilibrium tide theory

The equilibrium tide theory is based on a hypothetic Earth which is totally covered with water and has no land masses. Friction and inertia are also disregarded. In this case, waters covering the Earth respond instantaneously to the tide-generating forces to form *a surface of equilibrium* under the equilibrium theory. The theoretical tides formed under these conditions are known as the equilibrium tides. According to Bruns's formula (Hofmann-Wellenhof and Moritz 2006), the vertical distance ζ can be derived by

$$\zeta = \frac{V_t}{g}, \tag{2.28}$$

where g is the Earth's mean gravity and the V_t is the disturbing potential. In terms of the tide heights, the disturbing potential is the tide-generating potential as indicated by (2.17) or (2.18).

2.5 Real response to the tide-generating potential

In reality, it is unrealistic to assume that the ocean tide follows an equilibrium response as none of the assumptions of the equilibrium theory is fulfilled. To be specific, terrestrial factors play an important role in shaping the observed tides at a specific location and epoch. Some of the terrestrial factors are (Hicks and Szabados 2006):

- Earth rotation,
- irregular and restricted ocean depths,
- irregularly shaped continents,
- bottom friction,
- turbulence,
- water viscosity.

Smith (1999) discussed the unrealistic equilibrium response by summarizing several papers. The real response of the ocean to the tide-generating potential is the result of combined effect of the tide-generating potential and the terrestrial factors. These phenomena can be described by ocean dynamics.

Ocean dynamics The motion of the water mass, i.e. horizontal currents (u, v), i.e. *(local east, local north)* vector, and vertical tidal heights ζ, can be described by the *Laplace tidal equations* which were originally established by Marquis P.S. Laplace in 1775 (Smith 1999). Those equations are mostly valid in *deep ocean*[2], where some terrestrial factors like bottom friction can be ignored, see e.g. Cartwright (1993). As a consequence, the tidal equations become linear in u, v and ζ. Therefore (u, v, ζ) have the same frequencies as presented in the tidal generating potential, see section 2.2. However, in *shallow waters*, the dynamics

[2]The *deep* ocean is defined as the depths larger than about 200 m (Cartwright 1993).

become nonlinear due to the finite water depth, advection and bottom friction (Pugh 1996). The nonlinear distortion can be modelled by *compound tides* and *overtides*, which are higher harmonics with frequencies that are sums, differences or multiples of the frequencies in the tide-generating potential (Pugh 1996). Compound tides and overtides (e.g., M_4 and $2MS_2$) are also called shallow water tides, as they are caused by the nonlinear distortion of major astronomical tidal constituents (e.g., M_2, S_2) in shallow water (Andersen 1999). In other words, these high frequency constituents (from 3 to 13 cycles per day) produced by combining the fundamental diurnal and semi-diurnal constituents, are artefacts that attempt to describe the complex non-linear effects of bottom friction and shallow water. These constituents are outside of the scope of this research work.

In this case, the real tidal heights should be derived or predicted by tidal analysis using observations rather than by (2.28). There are mainly two tidal analysis methods: harmonic analysis and response analysis. For the response method, it is assumed that the ocean tides can be represented by the equilibrium tide and a weight function (Munk and Cartwright 1966). Therefore, the equilibrium tides calculated by (2.28) serves as the input values of the response method. The Fourier transformation of the weight function is called the *admittance*, see more details in e.g. (Munk and Cartwright 1966), (Cartwright and Ray 1991). Here, a brief introduction of the harmonic analysis method is given.

Harmonic analysis The tidal elevation of the water mass as a result of the tide-generating forces behaves linearly in *deep oceans* and can be analysed according to (Schwiderski 1980a; Pugh 1996)

$$\zeta(\lambda,\phi,t) = \sum_k f_k \xi_k(\lambda,\phi)\cos\left[\Theta_k(t) + \chi_k + u_k - \delta_k(\lambda,\phi)\right]. \tag{2.29}$$

where the summation over k includes all the constituents to be considered. Unknowns $\xi_k(\lambda,\phi)$ and $\delta_k(\lambda,\phi)$ represent the amplitude and phase lag of a particular constituent, also known as *harmonic constants*, which depend on the location (λ,ϕ). As Θ_k in (2.24) is the astronomical argument at *Greenwich*, $\delta_k(\lambda,\phi)$ is a phase lag at location (λ,ϕ) with respect to the Greenwich equilibrium tide. In other words, $\delta_k(\lambda,\phi)$ expresses the time interval between high water of the observed tide at (λ,ϕ) and high water of the Greenwich equilibrium tide, at frequency $\dot{\Theta}_k$ (Schureman 1958). f_k and u_k are the nodal factor and nodal angle accordingly, which are so-called nodal parameters. In practice, nodal parameters express the dependence of constituent coefficients and constituent arguments in terms of lunar node N (Schureman 1958). The aim of the harmonic analysis is to determine the constants ξ_k and δ_k by least-squares estimation. For this purpose, (2.29) can be written as

$$\zeta(\lambda,\phi,t) = \sum_k \left[f_k C_k(\lambda,\phi)\cos\left(\Theta_k(t) + \chi_k + u_k\right) + f_k S_k(\lambda,\phi)\sin\left(\Theta_k(t) + \chi_k + u_k\right)\right], \tag{2.30}$$

in which the constants C_k and S_k are to be estimated. The amplitude and phase lag can be derived by

$$\begin{aligned} \xi_k &= \sqrt{C_k^2 + S_k^2} \\ \delta_k &= \arctan\left(\frac{S_k}{C_k}\right). \end{aligned} \tag{2.31}$$

2.6 Ocean tide modelling and models

OCEAN tides can be modelled in two ways[3]:

i) solving the oceanic tides from the hydrodynamic equations. The corresponding model is a so-called *hydrodynamic model*, e.g. Schwiderski (1980b), Schwiderski (1983) and FES94.1 (Le Provost et al. 1994);

ii) fitting parameter model through tidal observations. The corresponding model is a so-called *empirical model*, e.g. the Goddard Ocean Tide (GOT) model series (Ray 1999), and Empirical Ocean Tide (EOT) model series (Savcenko and Bosch 2008; Savcenko and Bosch 2012).

In this study, ocean tide models GOT4.7 and EOT08a are used. Therefore, they are briefly introduced. Table 2.3 shows the basic information of the global tide model. An overview of altimetry missions, from which these models have been derived, can be referred to e.g. Table 1 in (Mayer-Gürr et al. 2012).

GOT4.7 Goddard Ocean Tide model GOT4.7 (Ray 1999) is an updated version of GOT99.2 (Ray 1999), both of which provide solutions for amplitudes and phases of the global oceanic tides. The Goddard Ocean Tide models are derived by empirical harmonic analysis of satellite altimetry relative to prior models. The prior models include *regional* hydrodynamic models as well as the *global* hydrodynamic model FES94.1 (Le Provost et al. 1994; Ray 1999; Stammer et al. 2014). The GOT4.7 solution depends only on the Topex/Poseidon (T/P) and Jason-1 satellites in the deep ocean within latitudes $[-66°, 66°]$, while in shallow seas and deep water at latitudes beyond ±66°, data from Geosat Follow-On (GFO), ERS-1, ERS-2 and ICESat are included (Stammer et al. 2014).

EOT08a Empirical Ocean Tide (EOT) model EOT08a is an empirical model derived by Deutsches Geodätisches Forschungsinstitut (DGFI) based on multi-mission satellite altimetry data. By taking the prior model FES2004 (Lyard et al. 2006) as a reference, EOT08a assimilates the data of altimetry mission T/P, Jason-1, ERS-2 and Envisat (Savcenko and Bosch 2008). At latitudes poleward of ±62°, which are the latitude limits

[3]Some researchers, e.g. Smith (1999), argued a third way: assimilating the tidal data into an existing hydrodynamic model. The corresponding model is called a *hybrid model*. In essence, it is the same as the second method.

of ERS-2 and ENVISAT, EOT08a is the same as FES2004. Table 2.3 shows constituents included in EOT08a by data analysis.

Table 2.3: Basic information of ocean tide model GOT4.7 and EOT11a

tide model	prior model	altimetry data used	constituent
GOT4.7	FES99.2	T/P, GFO, Jason-1	Q_1, O_1, P_1, K_1
	local tide models	ERS-1/2, ICESat	N_2, M_2, S_2, K_2, M_4
EOT08a	FES2004	T/P, Jason-1, GFO	$Q_1, O_1, P_1, K_1, 2N_2$
		ERS-2, Envisat	N_2, M_2, S_2, K_2, M_4

In this study, eight main tide constituents, namely $Q_1, O_1, P_1, K_1, N_2, M_2, S_2, K_2$, are included. The rest of the constituents are excluded for following reasons:

i) they are not modelled or commonly modelled by GOT4.7 and EOT08a, for instance all the long period constituents listed in Table 2.2;

ii) their magnitudes are small compared to the eight main constituents and negligible in the context of global analysis of the ocean tides;

iii) high harmonic constituents like overtones and compound tides only appear in the shallow water which is out of the scope of this study. In the deep ocean, it is unlikely that those constituents dominate ocean tide (Schrama 2011).

2.7 Spherical harmonic analysis of tidal heights

The ocean response of the tide-generating potential is the superposition of the tidal heights ζ_k which depend on frequencies. Being the same as in previous formulas, the subscript k refers to a particular tidal constituent. Each tidal height ζ_k corresponds to a constituent. Similar to (2.18), the tidal height ζ_k can be written in terms of amplitude ξ_k and phase lag δ_k at a specific location on the Earth (λ, θ) at an epoch t

$$\zeta(\lambda, \phi, t) = \sum_k \zeta_k = \sum_k \xi_k(\lambda, \phi) \cos\left[\Theta_k(t) + \chi_k - \delta_k(\lambda, \phi)\right]. \tag{2.32}$$

Now ζ_k can be written as

$$\zeta_k = \xi_k \cos(\delta_k)\cos(\Theta_k + \chi_k) + \xi_k \sin(\delta_k)\sin(\Theta_k + \chi_k). \tag{2.33}$$

Dow (1988) expanded the tidal height ζ_k into spherical harmonics. The in-phase and quadrature terms $\xi_k\cos(\delta_k)$ and $\xi_k\sin(\delta_k)$ can be expanded in spherical harmonics as

$$\begin{aligned} \xi_k \cos(\delta_k) &= \sum_{l=0}^{\infty} \sum_{m=0}^{l} \left[a_{lm,k}\cos(m\lambda) + b_{lm,k}\sin(m\lambda)\right] \bar{P}_{lm}(\sin\phi) \\ \xi_k \sin(\delta_k) &= \sum_{l=0}^{\infty} \sum_{m=0}^{l} \left[c_{lm,k}\cos(m\lambda) + d_{lm,k}\sin(m\lambda)\right] \bar{P}_{lm}(\sin\phi). \end{aligned} \tag{2.34}$$

where $a_{lm,k}$, $b_{lm,k}$, $c_{lm,k}$ and $d_{lm,k}$ are the corresponding normalized spherical harmonic coefficients and $\bar{P}_{lm}$ are normalized Legendre polynomials depending on degree l and order m. Inserting (2.34) into (2.33) gives

$$\zeta_k = \sum_{l=0}^{\infty} \sum_{m=0}^{l} \sum_{+}^{-} \left[\bar{C}^{\pm}_{lm,k} \cos(\Theta_k + \chi_k \pm m\lambda) + \bar{S}^{\pm}_{lm,k} \sin(\Theta_k + \chi_k \pm m\lambda) \right] \bar{P}_{lm}(\sin\phi). \tag{2.35}$$

The coefficients $(\bar{C}^{\pm}_{lm,k}, \bar{S}^{\pm}_{lm,k})$ represent normalized prograde and retrograde spherical harmonic coefficients of the tide k at degree l and order m. Alternatively, the coefficients can be written in terms of amplitude $\hat{\bar{C}}^{\pm}_{lm,k}$ and phase $\hat{\varepsilon}^{\pm}_{lm,k}$ as

$$\begin{aligned} \bar{C}^{\pm}_{lm,k} &= \hat{\bar{C}}^{\pm}_{lm,k} \sin(\hat{\varepsilon}^{\pm}_{lm,k}) = \frac{1}{2}\left(a_{lm,k} \mp d_{lm,k}\right) \\ \bar{S}^{\pm}_{lm,k} &= \hat{\bar{C}}^{\pm}_{lm,k} \cos(\hat{\varepsilon}^{\pm}_{lm,k}) = \frac{1}{2}\left(c_{lm,k} \pm b_{lm,k}\right), \end{aligned} \tag{2.36}$$

Therefore, the tidal heights can be expressed as

$$\zeta_k = \sum_{l=0}^{\infty} \sum_{m=0}^{l} \sum_{+}^{-} \hat{\bar{C}}^{\pm}_{lm,k} \sin(\Theta_k + \chi_k \pm m\lambda + \hat{\varepsilon}^{\pm}_{lm,k}) \bar{P}_{lm}(\sin\phi). \tag{2.37}$$

The mass redistribution effect of ocean tides on the Earth's gravitational potential is described by

$$\Delta V_k = \frac{GM_e}{r_e} \sum_{l=0}^{\infty} \left(\frac{r_e}{r_{OP}} \right)^{(l+1)} \sum_{m=0}^{l} \left[\Delta\bar{C}_{lm,k} \cos(m\lambda) + \Delta\bar{S}_{lm,k} \sin(m\lambda) \right] \bar{P}_{lm}(\sin\phi). \tag{2.38}$$

where r_e is the mean radius of the Earth and $(\Delta\bar{C}_{lm,k}, \Delta\bar{S}_{lm,k})$ are normalized spherical harmonic coefficients which can be derived by

$$\begin{aligned} \Delta\bar{C}_{lm,k} &= \frac{4\pi r_e^2 \rho_w}{M_e} \frac{1+k'_l}{2l+1} \left[\left(\bar{C}^{+}_{lm,k} + \bar{C}^{-}_{lm,k} \right) \cos(\Theta_k + \chi_k) + \left(\bar{S}^{+}_{lm,k} + \bar{S}^{-}_{lm,k} \right) \sin(\Theta_k + \chi_k) \right] \\ \Delta\bar{S}_{lm,k} &= \frac{4\pi r_e^2 \rho_w}{M_e} \frac{1+k'_l}{2l+1} \left[\left(\bar{S}^{+}_{lm,k} - \bar{S}^{-}_{lm,k} \right) \cos(\Theta_k + \chi_k) - \left(\bar{C}^{+}_{lm,k} - \bar{C}^{-}_{lm,k} \right) \sin(\Theta_k + \chi_k) \right], \end{aligned} \tag{2.39}$$

in which ρ_w is the water density and k'_l is the load Love number. The factor $(1 + k'_l)$ accounts for both the mass redistribution due to ocean tides, as well as the effect of the deformation of the solid Earth as a consequence of ocean mass redistribution.

Chapter 3

Ocean tide aliasing in satellite gravimetry

Based on the tide theory in Chapter 2, we know that the ocean tides can be modelled by the superposition of tidal constituents. As the gravimetry satellite cannot revisit a certain location within half a day or one day, semi-diurnal and diurnal tidal signals are under-sampled according to the Nyquist sampling theorem and alias to longer periods. Apart from that, gravity field solutions are derived by combining the global observations in a certain recovery period up to a certain degree and order, which results in applying space-time averaging to the observations. As a consequence, the gravity field solutions are derived by "re-sampling" the observations, which may cause aliasing as well. Therefore, in order to collect all the information to subtract tide signals from the observations, or from the final field products, we need to know the alias periods of tidal constituents.

Tidal aliasing is a typical problem in satellite altimetry, and the estimation of the alias periods of tidal constituents is well demonstrated by (e.g. Parke et al. 1987; Cartwright and Ray 1990; Schlax and Chelton 1994). However, the aliasing mechanism is different for satellite gravimetry and simply "borrowing" from satellite altimetry is not sufficient. Three pieces of evidence support this argument:

i) altimetry satellites normally fly in repeat orbits but the gravimetry satellites do not;

ii) final products of altimetry satellites, heights, are derived "point-wise" or locally combined, while satellite gravimetry measures a potential field and thus the sum of mass distribution or change;

iii) each observation is considered independently as an "instantaneous" sample in satellite altimetry, while time averaging is commonly used in satellite gravimetry to derive a solution within a certain period.

Therefore, alias period estimation in satellite gravimetry needs to be investigated specifically. Chapter 1 described that by knowing signal frequency and sampling frequency, the aliasing frequency can be estimated. As signal frequencies, frequencies of tidal constituents in this case, are precisely known, finding sampling frequencies becomes the key task. In this chapter, the mechanism of tidal aliasing in satellite gravimetry is discussed in detail and the sampling frequencies are determined. As a result, the alias periods can be estimated analytically.

At the beginning, spatial aliasing and temporal aliasing are discussed in general in section 3.1 and section 3.2, respectively. Next, the alias mechanism in satellite gravimetry is investigated in two aspects: orbit sampling (section 3.3) and gravity recovery (section 3.4). Section 3.5 discusses the relation between the perturbation frequency and alias frequency. In the end, section 3.6 summarizes the tide aliasing spectrum estimation in satellite gravimetry.

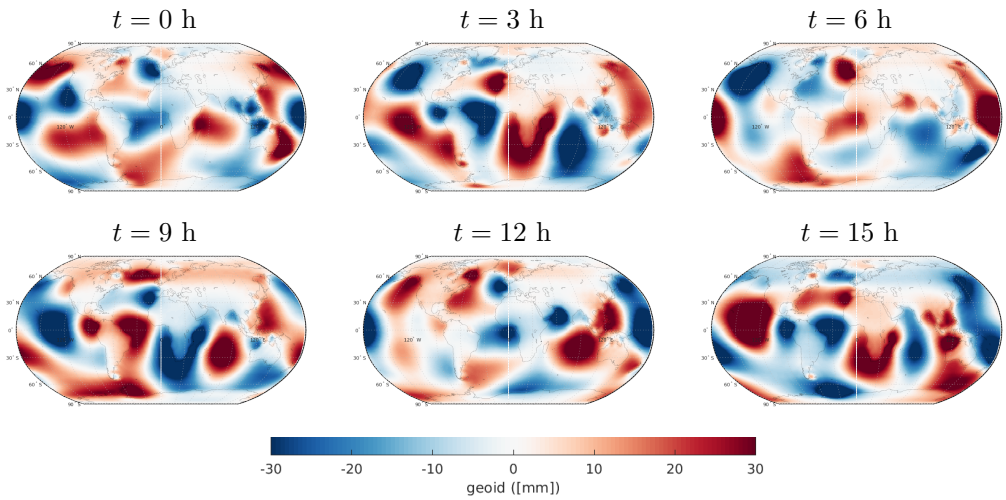

Figure 3.1: Variations of ocean tides in geoid height [mm] on January 1, 2002. The tide signals include 8 major constituents M_2, N_2, S_2, K_2, K_1, O_1, P_1 and Q_1 from tide model EOT08a.

3.1 Spatial aliasing

SPATIAL aliasing and temporal aliasing are two types of aliasing problem. In some cases, they can be referred as two sides of the same problem, which means they are equivalent and one can choose any of them to investigate. But in other cases, they have nothing in common and the researcher must decide what they want to investigate and then take the corresponding concept to carry on the study. In general, spatial aliasing is caused by insufficient sampling of the data along the space axis and is discussed in

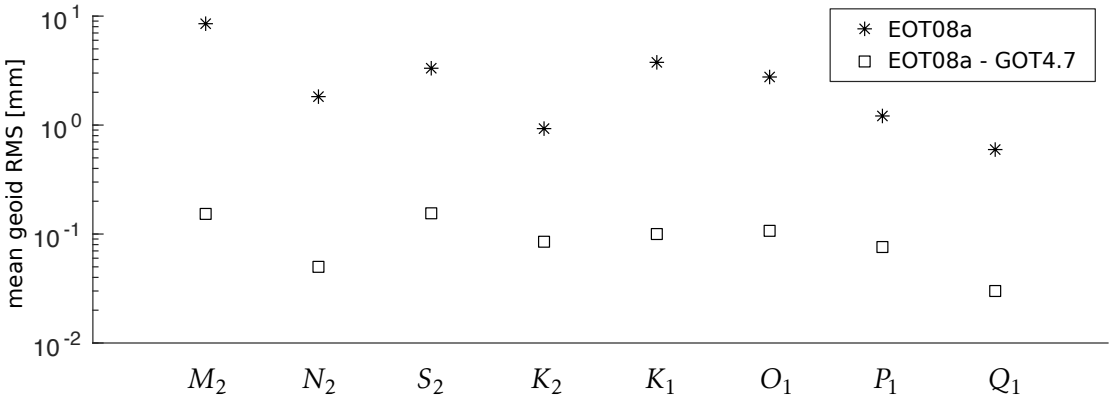

Figure 3.2: Mean geoid RMS of one day of tidal signal from tide model EOT08a and tidal errors by EOT08a–GOT4.7.

the wavenumber space. The term *wavenumber* refers to the spatial frequency of a wave, measured in cycles per unit distance or radians per unit distance.

Ocean tides are temporal-spatial signals. On the one hand, tidal height variations are point-wise and time dependent. On the other hand, the tidal height profile of continuous region forms a waveform in space. In satellite altimetry, the juxtaposition of the phase-shifted aliased signals at adjacent nodes causes the spatial aliasing of tidal signals (Schlax and Chelton 1994). These aliased tidal signals might be misinterpreted as sea surface height or as evidence for a westward propagating Rossby wave[1]. For instance, Schlax and Chelton (1994) showed that the spatial aliasing of M_2 tidal error for T/P acted as a westward propagating signal.

Tidal heights are commonly expressed in terms of spherical harmonics, as shown in section 2.7, which are also widely used when investigating gravity signals globally. Consequently, the spatial aliasing has an extended meaning. As the spherical harmonics represent the spatial scale, mapping of the signal from higher spherical harmonics onto lower spherical harmonics is equivalent to mapping the short-wavelength signal to the long-wavelength signal. As a result, signals of different locations are aliased to each other. Koop and Rummel (2007) gave examples of *coarse* spatial aliasing and *fine* spatial aliasing based on GRACE results. An example of *coarse* spatial aliasing is the relative low-precision $C_{2,0}$ time series, and an example of *fine* spatial aliasing is localized excursions of gravity field signals (Koop and Rummel 2007). Seo et al. (2008b) showed that errors in component of higher harmonics of semi-diurnal tides can alias into lower harmonics, for instance $Y_{6,2}$ of S_2 can alias to $Y_{6,0}$, $Y_{4,0}$ and $Y_{2,0}$.

Due to the presence of land, ocean tides are not globally distributed signals. Therefore, the spherical harmonic analysis of tidal heights introduces errors by nature. Figure 3.1

[1] Rossby wave, also known as planetary wave, is a natural phenomenon in the atmosphere and oceans of rotating planets.

shows geoid heights of tidal constituents expressed in spherical harmonics. Significant "ocean tide signals", which are errors, are present on land. However, this phenomenon can be considered as ocean tide signal *leaking* to the land rather than *aliasing* to the land, as no under-sampling of ocean tides is involved while applying spherical harmonic analysis to the tidal heights. Figure 3.2 shows the magnitudes of tidal signals and errors of eight major constituents in mean geoid RMS. Generally speaking, *spatial aliasing* happens when signals are *undersampled* in spatial domain, while *spatial leakage* happens when signals are *"transferred"* from their original location to other location(s) due to data processing.

3.2 Temporal aliasing

Temporal aliasing is normally discussed in the time-frequency domain. A temporal alias is referred when the time characteristics of investigated signals are the key information. For instance, tide modelling aims to derive the amplitude and phase lag of an individual constituent, and the temporal height variations of tidal constituents are important inputs. When using satellites to sample the tidal signals, tidal constituents with short periods alias to long periods due to undersampling. In this case, *aliasing* specifically refers to temporal aliasing.

An important aim of gravity field research is to investigate the temporal gravity field, e.g. due to water storage change. Time-frequency analysis is a common strategy to approach the task. Therefore, as an important error source of the temporal gravity field, tidal aliasing in the satellite gravity field is better investigated in the time-frequency domain. Actually, as ocean tides are temporal-spatial signals, tidal aliasing errors expressed in the time domain also present themselves in the spatial domain. If the aliasing error is removed in the time domain, its spatial effect is also removed. Therefore, the tidal aliasing can be investigated in either time domain or spatial domain, but there is no need to deal with them in both domains for a single aim.

The aliasing problem discussed from now on refers to temporal aliasing. Therefore, in order to estimate the alias errors, the key is to get precise alias periods. With alias periods, the error magnitudes of tidal constituents can be estimated. An altimeter satellite in a repeat orbit with a period of α nodal days samples the tides at a given location once every α nodal days, which is called repeat period. The observations are processed at each location independently with a given spatial resolution. In this case, there is only one-step aliasing caused by satellite orbit undersampling and the alias periods can be calculated with the signal periods and sampling periods, i.e. the tidal constituent periods and the repeat period α days accordingly. The ocean tide aliasing in satellite gravimetry is different from that in satellite altimetry as discussed at the beginning of this chapter. In view of those aspects, there is a two-step sampling and accordingly two-step aliasing in satellite gravimetry, see Figure 3.3. The first step is primary aliasing due

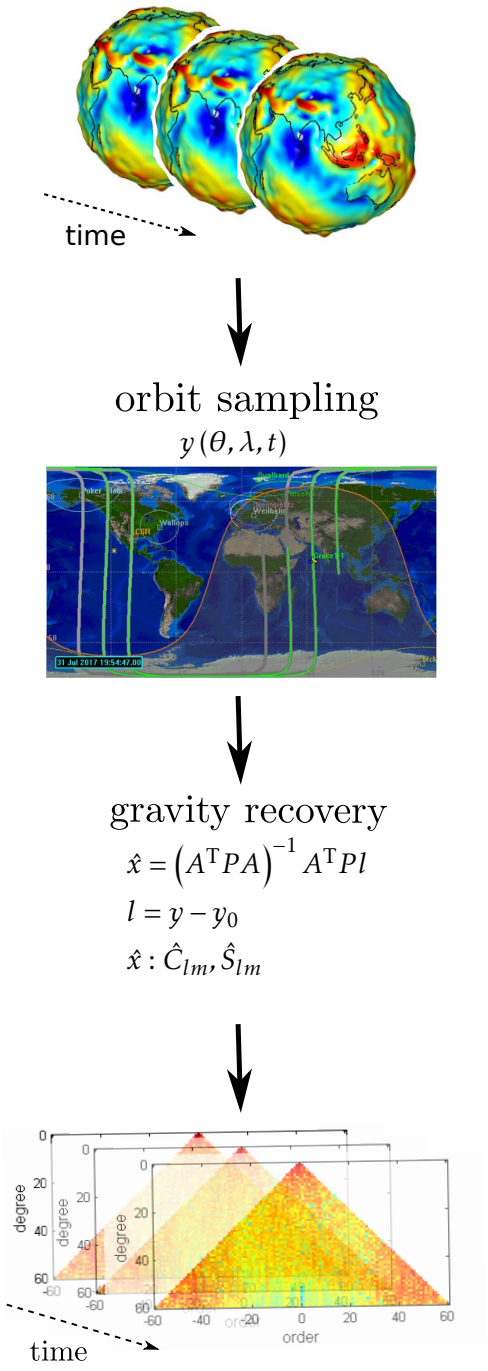

Figure 3.3: Two-step sampling in satellite gravimetry. The first diagram representing Earth is from https://www.jpl.nasa.gov/spaceimages, and the diagram of ground track is from http://www2.csr.utexas.edu/grace/ground/.

to undersampling of signals by satellite orbits, and the second step is secondary aliasing due to resampling (and undersampling) of observations during gravity recovery. The two-step sampling will be elaborated in following sections.

3.3 Orbit sampling and primary aliasing

The observations of satellite gravimetry taken from orbits are largely related to the signals below the orbit tracks, though not point-wise. Therefore, the ground track pattern is directly connected to the sampling of temporal signals. If we consider a repeat orbit, a satellite revisits the exact location after α nodal days. The satellite samples the Earth with a frequency of $1/\alpha$. For a non-repeat orbit, or an orbit with a considerable large repeat period and not repeating itself within a targeted time span, the samples of a satellite along a latitude cycle can be considered jointly regardless of the local characteristics, namely local amplitudes and phase lags. The corresponding sampling rate is the orbit plane procession rate $\dot{\Lambda}$ in the Earth-fixed frame, namely $\dot{\Lambda} = \dot{\Omega} - \omega_{\mathrm{E}}$, in which $\dot{\Omega}$ is nodal drift rate and ω_{E} is the Earth rotation rate. This approximation of drift-orbit sampling holds only when the investigated signal can be considered as *longitudinal uniform signal*. *A longitudinal uniform signal* specifically means the signal can be modelled as (superposition of) spatially continuous harmonic(s) with the constant amplitudes for all different longitudes. A longitudinal uniform signal guarantees that different orbit planes sample the same signal in longitudinal direction, under which condition the orbit plane procession rate can be taken as the sampling rate.

In terms of ocean tide aliasing, the above approximation is valid when we consider each tidal constituent as a longitudinal sinusoid signal rather than a localized signal. Rewriting (2.35) as

$$\zeta_k = \sum_{l=0}^{\infty} \sum_{m=0}^{l} A_{lm,k} \cos\left(\Theta_k + \Phi_{lm,k}\right) \bar{P}_{lm}(\sin\phi), \tag{3.1}$$

then

$$\begin{aligned} A_{lm,k}\cos\left(\Theta_k + \Phi_{lm,k}\right) &= A_{lm,k}\cos\left(\dot{\Theta}_k t + \Phi_{lm,k}\right) \\ &= \sum_{+}^{-}\left[\bar{C}^{\pm}_{lm,k}\cos\left(\dot{\Theta}_k t + \chi_k \pm m\lambda\right) + \bar{S}^{\pm}_{lm,k}\sin\left(\dot{\Theta}_k t + \chi_k \pm m\lambda\right)\right] \\ &= A^{+}_{lm,k}\sin\left(\dot{\Theta}_k t + \chi_k + m\lambda + \phi^{+}_{lm,k}\right) + \\ &\quad A^{-}_{lm,k}\sin\left(\dot{\Theta}_k t + \chi_k - m\lambda + \phi^{-}_{lm,k}\right), \end{aligned} \tag{3.2}$$

in which $\dot{\Theta}_k$ is the tidal constituent frequency and

$$\begin{aligned} A^{\pm}_{lm,k} &= \sqrt{\bar{C}^{\pm 2}_{lm,k} + \bar{S}^{\pm 2}_{lm,k}} \\ \phi^{\pm}_{lm,k} &= \arctan\frac{\bar{C}^{\pm}_{lm,k}}{\bar{S}^{\pm}_{lm,k}}, \end{aligned} \tag{3.3}$$

the amplitude $A_{lm,k}$ and initial phase $\Phi_{lm,k}$ are

$$\begin{aligned} A_{lm,k} &= \sqrt{A_{lm,k}^{+2} + A_{lm,k}^{-2} + 2A_{lm,k}^{+}A_{lm,k}^{-}\cos\left(2m\lambda + \phi_{lm,k}^{+} - \phi_{lm,k}^{-}\right)} \\ \Phi_{lm,k} &= \arctan\frac{A_{lm,k}^{+}\sin\left(\chi_k + m\lambda + \phi_{lm,k}^{+}\right) + A_{lm,k}^{-}\sin\left(\chi_k - m\lambda + \phi_{lm,k}^{-}\right)}{A_{lm,k}^{+}\cos\left(\chi_k + m\lambda + \phi_{lm,k}^{+}\right) + A_{lm,k}^{-}\cos\left(\chi_k - m\lambda + \phi_{lm,k}^{-}\right)}. \end{aligned} \tag{3.4}$$

Similarly, (3.1) can be further written as

$$\zeta_k = A_k\cos\left(\dot{\Theta}_k t + \Phi_k\right), \tag{3.5}$$

the amplitude A_k and initial phase Φ_k can be derived by successively adding two sinusoidal waves, which is similar to the typical problem in physics: *synthesis of simple harmonic vibration in same direction at same frequency*. In this case, the sinusoidal waves to be added are

$$\underbrace{A_{lm,k}\bar{P}_{lm}(\sin\phi)}_{\text{amplitude}}\sin\left(\dot{\Theta}_k t + \Phi_{lm,k} + \frac{\pi}{2}\right), \tag{3.6}$$

with the degree l and order m vary accordingly. Adding every two harmonics above will derive a new harmonic with a similar amplitude and phase as given by (3.4) at the same frequency $\dot{\Theta}_k$. The addition operation continues till the generalized form (3.5) is achieved. The generalized form (3.5) indicates that tidal height of each constituent can be expressed as *a single sinusoid wave* at a given latitude λ if one ignores the longitudinal-dependent amplitude A_k and initial phase Φ_k as (3.4). Note that $A_{lm,k}^{\pm}$ and $\phi_{lm,k}^{\pm}$ do not equal A_k and Φ_k, but act as the factors to calculate them by applying an equation similar to (3.4).

This idealized assumption, *single wave at latitude circle*, is not in line with reality when we see the co-tidal charts or the amplitude and phase maps of constituents. However, this **single-wave assumption** is justified because of two reasons:

i) the amplitudes (which will be taken care of later) are out of scope at this moment;

ii) the phase differences of the neighbouring regions at the same latitude are negligible.

In other words, the signal frequency is the only factor that matters in this step of orbit sampling. Given the arguments above, we can assume a constant amplitude and a constant phase lag for all single points at the same latitude. That is, the alias of a given tidal constituent may be illustrated by sampling a spatially uniform harmonic with the tidal frequency at the satellite sampling points, which is also adopted by (Schlax and Chelton 1994).

Figure 3.4 shows the basic idea of the single-wave assumption. The left diagram is a tidal height envelope of a semi-diurnal constituent at a constant latitude viewed from the north pole (NP). Taking the *original* Earth surface (the circle) as height "0", the

distances between *deformed* Earth surface (the ellipse) and the *original* Earth surface can be considered as the tidal heights. If we open this tidal height envelope at o and map it into a two-dimension space, the tidal height will unfold as vertical axis, indicated as the right diagram of Figure 3.4. The horizontal axis can be taken as both the spatial axis and the time axis. When taken as spatial axis, it increases from longitude 0° to 360° from o to o and repeats afterwards. When taken as time axis, every o-to-o indicates one sidereal day. An arrow indicates a sample. Different samples at different longitudes can be considered as the same samples as long as they are at the same phase. For example, the samples with dash-line arrows are the mapping of solid-line samples. In this case, samples at different longitudes are only distinguished by tidal phases, not by locations, and the tidal height variation is considered as a single-wave signal rather than many waves (therefore, many signals) for different longitudes at a certain latitude circle.

This space-time change of tidal signal can be further illustrated by *a simplified example* in Figure 3.5. Two sinusoids with periods of 12 hours and 24 hours *represent semi-diurnal and diurnal tides roughly*. An arrow indicates a sample at one epoch. Within one day, samples almost locate at the same phase regardless of the sampling epoch. This is because the dominant part of tidal frequency, cf. equation (2.26), and the orbit precession in the Earth-fixed frame are the same, namely Earth rotation rate. Therefore, the change of tidal phase and the orbit rotation angle with respect to the Earth are synchronous. For the real tidal constituents with not exactly 12 hours or 24 hours, the phases of samples are expected to vary in a small range around the arrow, from which one cannot recover the entire signal. After an adequate time length, at least one alias period, enough varied phase information is collected to recover the original signal.

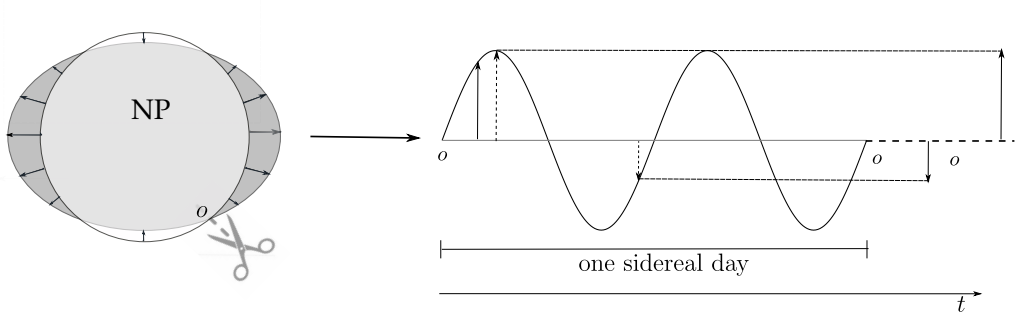

Figure 3.4: The single-wave assumption.

For further understanding, orbit sampling in this context specifically means the procedure that the orbit plane scans the phase of a signal while precessing relative to the Earth. The measure of *tidal phase change per longitudinal degree*, ϕ_{1d}, is

$$\phi_{1d} = \frac{f_t \cdot T_{sd}}{360}, \tag{3.7}$$

in which f_t is the phase velocity of a single constituent, and T_{sd} stands for a sidereal day. For an individual constituent, it is obvious that ϕ_{1d} only depends on its own frequency

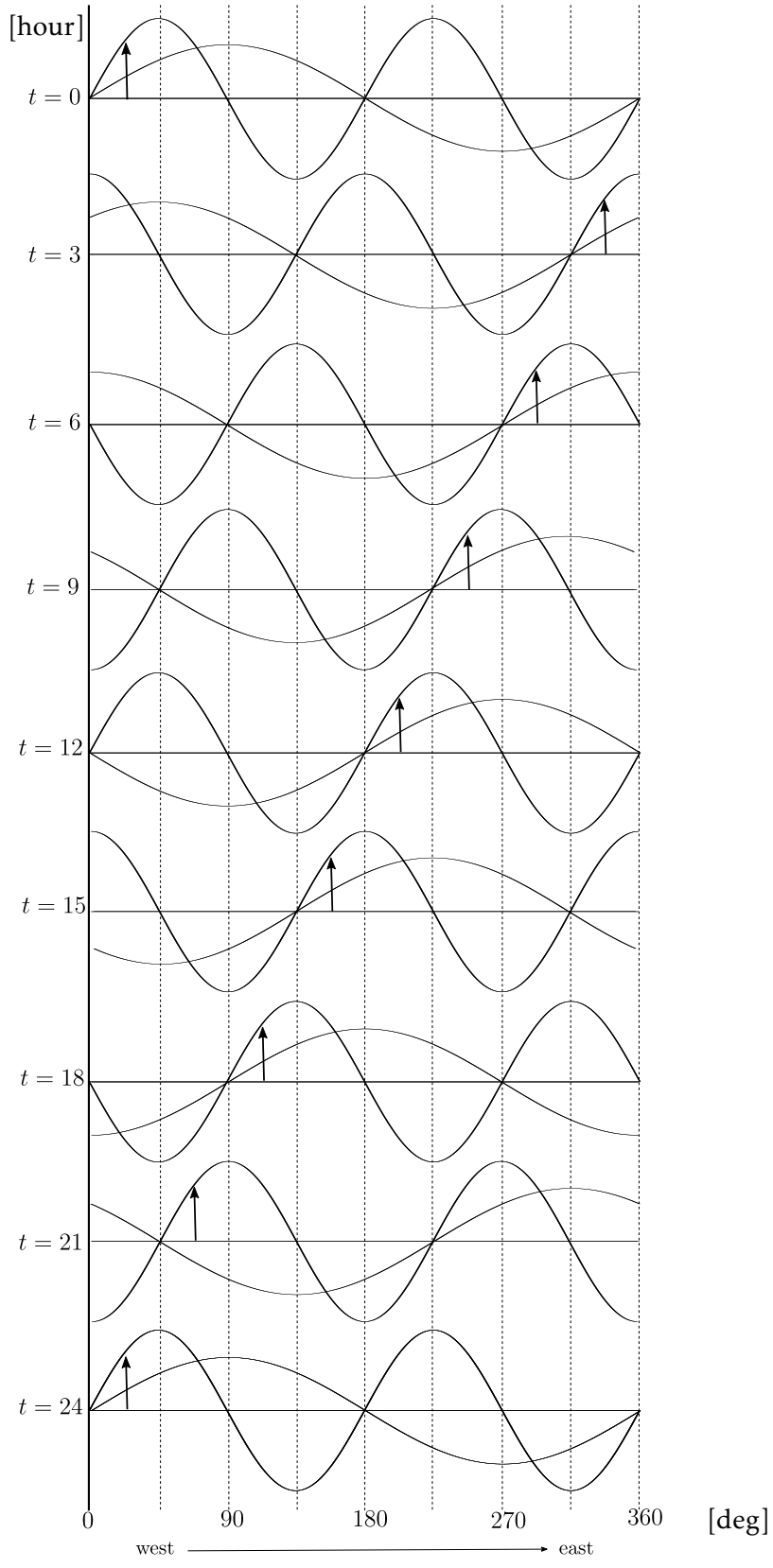

Figure 3.5: Orbit sampling of diurnal and semi-diurnal signals in one day.

and is a constant. Suppose the longitude of the ascending node of the orbit plane at $t = t_0$ is $\Lambda(t_0) = 0°$ and the tidal phase of a constituent is $\phi(t_0) = 0°$, the longitude of the ascending node at $t = t_1$, $\Lambda(t_1)$, will be

$$\Lambda(t_1) = (\dot{\Omega} - \omega_E)t_1 + 360°n, \tag{3.8}$$

in which $n \in Z$ is an integer to keep $\Lambda(t_1)$ in the range of $[0°, 360°)$. Then the tidal phase at t_1 is

$$\phi(t_1) = \phi_{1d} \cdot \Lambda(t_1) + f_t t_1 + 360°n. \tag{3.9}$$

Using equation (3.7), (3.8) and (3.9), we can get the similar phase change sequences as shown in Figure 3.5.

To summarize, orbit sampling of ocean tides cause a first-step aliasing in satellite gravimetry, and the corresponding alias frequency is called primary alias frequency, noted as f_a^p. The primary alias frequency can be estimated by applying equation (1.1) with specific integer N satisfying

$$f_a^p = \min\left(\left|f_t - N\left(\dot{\Omega} - \omega_E\right)\right|\right). \tag{3.10}$$

***u*-*t* cyclogram** The estimated primary alias periods can be demonstrated by displaying the field or its functionals along the orbit with *u-t cyclogram*. A *u-t* cyclogram shows the observable in the domain of argument of latitude u against time t. Conventionally, the argument of latitude of the ascending node is 0°, and u equals 90°, 180°, 270° (or −90°) when a satellite is at the most Northern points, equator (descending node), the most Southern points, accordingly. The argument of latitude u and latitude ϕ are related by

$$\sin\phi = \sin I \sin u\,, \tag{3.11}$$

in which I is the inclination of the satellite.

Table 3.1: Simulation and alias periods of individual tidal constituent.

constituent	simulation time [day]	alias period [day]	number of cycles
M_2	60	13.96	4.3
N_2	60	9.27	6.5
S_2	363	257.51	1.4
K_2	1826 (5y)	628.02	2.9
K_1	1826 (5y)	1256.03	1.5
O_1	60	13.81	4.3
P_1	363	213.70	1.7
Q_1	60	9.20	6.5

Demonstration of $f_{\mathbf{a}}^{\mathbf{p}}$ In this demonstration a nominal orbit at $h = 361.9$ km and $I = 92°$ is simulated with *tidal error* of individual constituent as input. A nominal orbit means that the eccentricity of the orbit equals 0, and thus no perturbation due to perigee drift $\dot{\omega}$. It should be reminded that a repeat orbit is not a necessity. The tidal error is obtained by the difference of two tide models, namely EOT08a and GOT4.7. The spatial distribution of ocean tides and the magnitudes of the tidal errors are shown in the Figure 3.1 and Figure 3.2. The simulated observation is the acceleration difference of two satellites projected on the line-of-sight direction, that is

$$(\nabla V_B - \nabla V_A) \cdot \vec{e}_{AB}, \tag{3.12}$$

in which A and B stand for two satellites flying as GRACE-type formation, and $\vec{e}_{AB}$ is the line-of-sight unit vector of the low-low satellite ranging between satellite A and B. Table 3.1 shows the estimated primary alias period according to (3.10), simulation periods and expected cycles in the given simulation periods. Figure 3.6 and 3.7 show the observations along the orbit for 8 major constituents. The plot on the left side shows the observation distribution in the u-t domain, and the right side shows the RMS of observations. The red and blue color indicate the opposite sign of observations. If one "scans" the u-t cyclogram along a constant u, obvious alternating red-blue patterns are shown for all 8 constituents. The number of alternations equals the number of cycles given in Table 3.1, which well demonstrates the estimated alias period by (3.10).

3.4 Gravity recovery and secondary aliasing

GRAVITY field recovery from satellite missions is a process combining observations or geopotential functionals along orbits in a certain recovery period, T_{r}, to derive the spherical harmonic coefficients till a certain degree and order. In this process, data covering most regions of the Earth and spanning several days are merged into one solution. Therefore, after being sampled by orbits, the temporal signals are sampled in a second time by T_{r}-day averaging. In general, the functionals of the geopotential, $f^{\#}$, can be represented by a 2D-Fourier series (Sneeuw 2000) for a nominal orbit:

$$f^{\#} = \sum_{m=-\infty}^{\infty} \sum_{p=-\infty}^{\infty} A_{mp}^{\#} e^{i\psi_{mp}}, \tag{3.13}$$

with

$$\begin{aligned} A_{mp}^{\#} &= \sum_{l=\max(|m|,|p|)}^{\infty} H_{lmp}^{\#} \bar{K}_{lm} \\ \psi_{mp} &= pu + m\Lambda = \dot{\psi}_{mp} t + \psi_{mp}(t_0), \end{aligned} \tag{3.14}$$

in which $H_{lmp}^{\#}$ is transfer coefficient and $\bar{K}_{lm}$ is normalized spherical harmonic coefficient of degree l and order m. Index p is used instead of k to avoid the conflict of using k as tidal constituent indicator. Transfer coefficients of several functionals can be found in

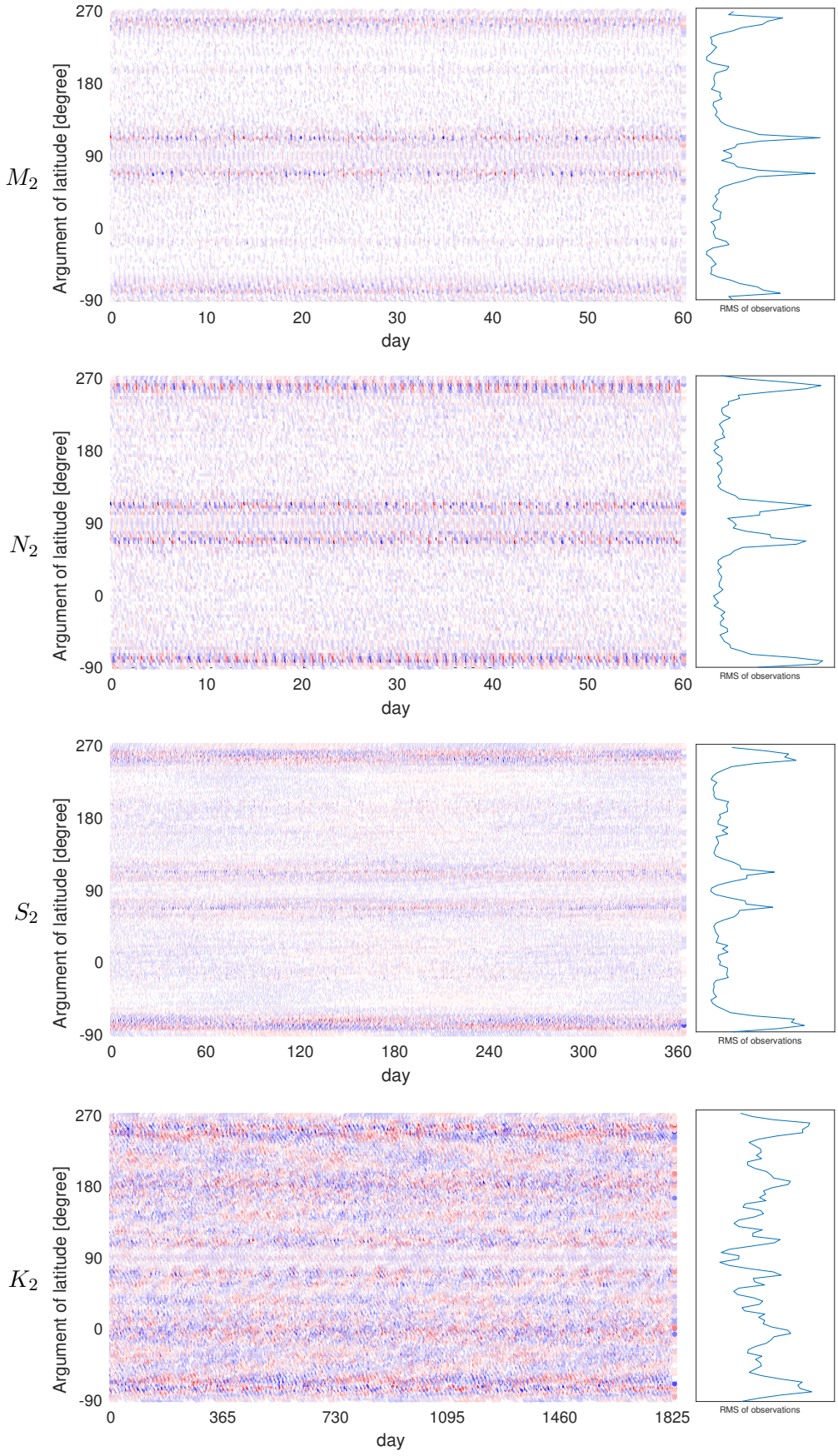

Figure 3.6: Orbit sampling of the semi-diurnal constituents. The red and blue color indicate the opposite sign of observations along orbits.

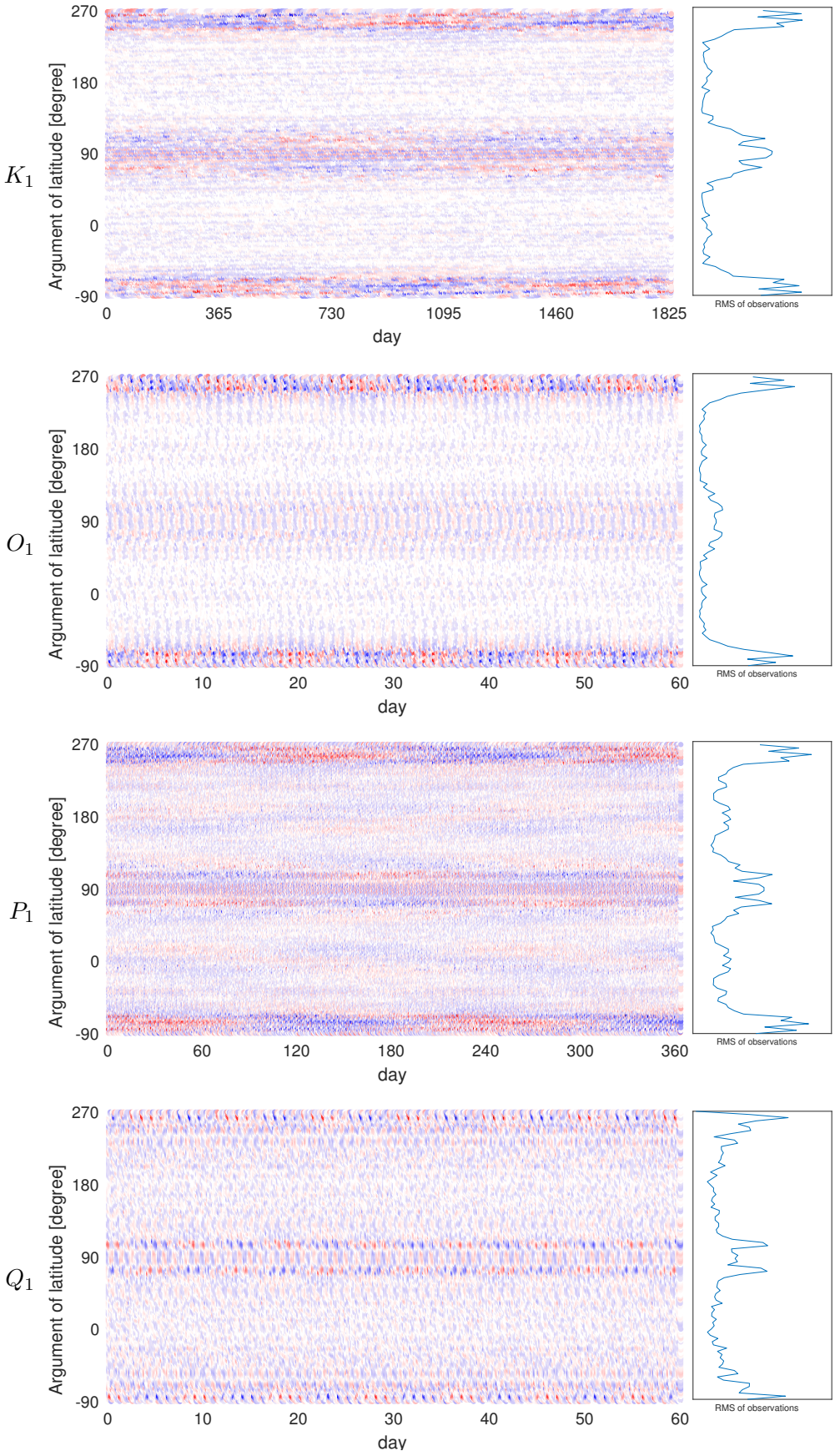

Figure 3.7: Orbit sampling of the diurnal constituents. The red and blue color indicate the opposite sign of observations along orbits.

(e.g. Sneeuw 2000, p. 31). Gravity recovery is to estimate coefficients $\bar{K}_{lm}$ according to $f^{\#}$ and corresponding $H^{\#}_{lmp}$.

The spherical harmonic coefficients of ocean tides are time variable (Petit and Luzum 2010), see (2.39), therefore

$$\begin{aligned}\bar{K}_{lm}(t) &= \left[\Delta\bar{C}_{lm} + i\Delta\bar{S}_{lm}\right](t) \\ &= \sum_k \sum_{+}^{-} \left(C^{\pm}_{lm,k} \mp i S^{\pm}_{lm,k}\right) e^{\pm i\dot{\Theta}_k t}.\end{aligned} \tag{3.15}$$

Comparing (3.15) to (2.39), the coefficients $C^{\pm}_{lm,k}$ and $S^{\pm}_{lm,k}$ can be computed as

$$\begin{aligned}C^{\pm}_{lm,k} &= \frac{4\pi r_e^2 \rho_w}{M_e} \frac{1+k'_l}{2l+1} \hat{\bar{C}}^{+}_{lm,k} \sin\left(\hat{\varepsilon}^{\pm}_{lm,k} + \chi_k\right) \\ S^{\pm}_{lm,k} &= \frac{4\pi r_e^2 \rho_w}{M_e} \frac{1+k'_l}{2l+1} \hat{\bar{C}}^{+}_{lm,k} \cos\left(\hat{\varepsilon}^{\pm}_{lm,k} + \chi_k\right).\end{aligned} \tag{3.16}$$

Rewriting (3.15) one gets

$$\begin{aligned}\Delta\bar{C}_{lm} &= \sum_k \sum_{+}^{-} A^{C}_{lm,k} \sin\left(\dot{\Theta}_k t + \Phi^{C}_{lm,k}\right) \\ \Delta\bar{S}_{lm} &= \sum_k \sum_{+}^{-} A^{S}_{lm,k} \sin\left(\dot{\Theta}_k t + \Phi^{S}_{lm,k}\right),\end{aligned} \tag{3.17}$$

with

$$\begin{aligned}A^{C}_{lm,k} &= \sqrt{\left(C^{+}_{lm,k} + C^{-}_{lm,k}\right)^2 + \left(S^{+}_{lm,k} + S^{-}_{lm,k}\right)^2} \\ A^{S}_{lm,k} &= \sqrt{\left(C^{+}_{lm,k} - C^{-}_{lm,k}\right)^2 + \left(S^{+}_{lm,k} - S^{-}_{lm,k}\right)^2} \\ \Phi^{C}_{lm,k} &= \arctan\left(\frac{C^{+}_{lm,k} + C^{-}_{lm,k}}{S^{+}_{lm,k} + S^{-}_{lm,k}}\right) \\ \Phi^{S}_{lm,k} &= \arctan\left(\frac{S^{-}_{lm,k} - S^{+}_{lm,k}}{C^{+}_{lm,k} - C^{-}_{lm,k}}\right).\end{aligned} \tag{3.18}$$

Equation (3.17) indicates that the spherical harmonic coefficient increment corresponding to ocean tides can be considered as the sum of harmonics at the same frequencies $\dot{\Theta}_k$ as the tidal constituents. After the undersampling by orbits, the original tidal signals at frequency $\dot{\Theta}_k$ alias into primary alias frequency $f^{\mathrm{p}}_{\mathrm{a}}$ (3.10). Therefore, the geopotentional functionals $f^{\#}$ derived from orbit(s) convey the *new distorted* tidal signals at frequency $f^{\mathrm{p}}_{\mathrm{a}}$. Gravity recovery with T_{r} day is equivalent to sampling the *new distorted* tidal signals of frequency $f^{\mathrm{p}}_{\mathrm{a}}$ by frequency $1/T_{\mathrm{r}}$. If $1/T_{\mathrm{r}} \leq 2f^{\mathrm{p}}_{\mathrm{a}}$, *secondary aliasing* happens. The name *secondary aliasing* is designated by following the primary aliasing due to orbit undersampling. A secondary aliasing frequency can be estimated as

$$f^{\mathrm{s}}_{\mathrm{a}} = \min\left(\left|f^{\mathrm{p}}_{\mathrm{a}} - N\frac{1}{T_{\mathrm{r}}}\right|\right). \tag{3.19}$$

Similar to primary aliasing, the secondary aliasing is demonstrated as well. An analysis method *simulation-based alias spectrum analysis (SBASA)* is proposed for this task, which will be discussed specifically in next chapter.

Spherical harmonic representation of S_2 A special remark should be made for the principal solar semidiurnal constituent, S_2, which represents the Earth rotation with respect to the Sun. As the tidal potential envelope of S_2 seems to perfectly coincide with the surface spherical harmonic $Y_{2,2}$ and have nothing in common with $Y_{2,0}$ (see Figure 3.8), it is easy to mistakenly think that spherical harmonic expansion of S_2 can be derived without $Y_{2,0}$, or, the commensurate $\Delta C_{2,0}$ of S_2 equals 0. This is wrong due to an overlooked fact that the equator and the ecliptic do not coincide. The deformation of the Earth because of the perturbation of the S_2 tidal force has an ellipsoidal shape with the semi-major axis always towards the Sun in the ecliptic, which can be expressed by $Y_{2,2}$ in the coordinate frame (θ', λ'), with colatitude ecliptical θ' and longitude λ'. The spherical harmonic analysis of the tides is normally conducted in the coordinate frame (θ, λ), which are the equatorial colatitude and longitude. Regardless of the complexity of tidal amplitudes and phase lags for different locations, the S_2 deformation of the Earth can be expressed by a single $Y_{2,2}$ when taking the ecliptic as reference. The connection between the S_2-perturbed Earth shape and the conventional spherical harmonics can be achieved by rotating the ecliptic to the equator. According to representation theory, the rotation of spherical harmonics (Sneeuw 2000), spherical harmonic in the original frame (θ', λ') is a linear combination of harmonics of the same degree l in the rotated frame (θ, λ). Therefore, the following relationship holds:

$$Y_{2,2}(\theta', \lambda') = \sum_{k=-2}^{2} D_{22k}(\alpha, \beta, \gamma) Y_{2k}(\theta, \lambda), \tag{3.20}$$

with rotation angle

$$\begin{aligned} \alpha &= \frac{2\pi}{24 \cdot 3600} t - \frac{\pi}{2} \\ \beta &= \varepsilon \\ \gamma &= \frac{\pi}{2}, \end{aligned} \tag{3.21}$$

in which t is the local time in second and ε is the obliquity of the ecliptic. The representation coefficients $D_{lmk}(\alpha, \beta, \gamma)$ and an elaborate discussion of the rotation of spherical harmonics can be found in (Sneeuw 2000). Equation (3.20) demonstrates that the commensurate ΔC_{20} of S_2 will not be 0 in general.

3.5 Perturbation frequency and alias frequency

As discussed in section 1.2, Cheng and Ries (2017) took tide perturbation frequencies as the aliasing frequencies of the ocean tides, which needs special attention. In order to understand the relation between the aliasing frequency and the perturbation

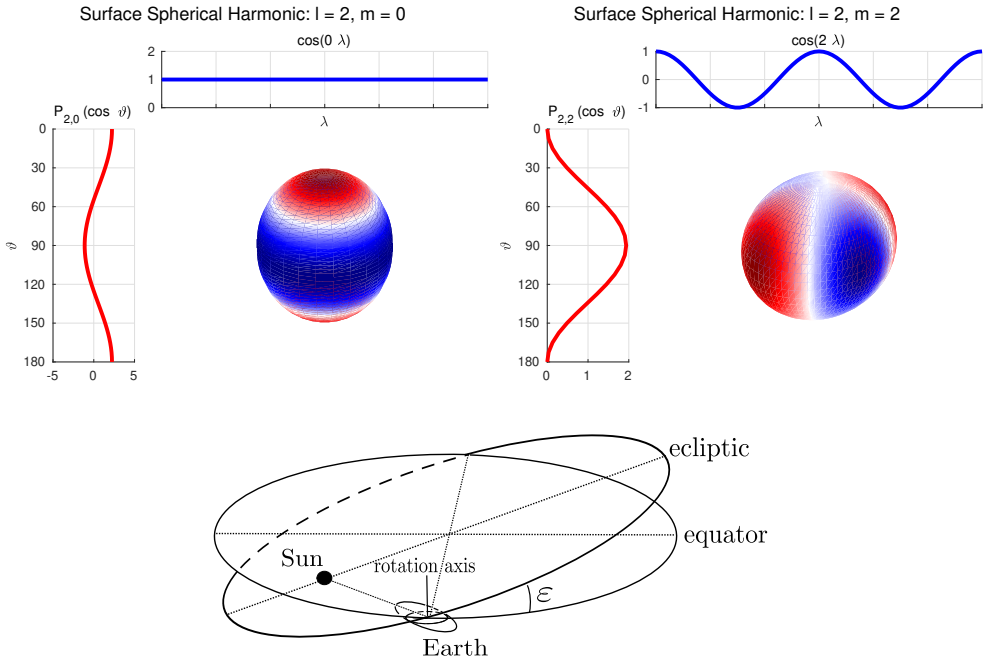

Figure 3.8: Surface spherical harmonics Y_{20}, Y_{22} (top) and Earth-Sun system indicating the S_2-disturbed Earth profile (bottom). The ecliptic obliquity ε is about 23°26′. The Earth shape is exaggerated to show the deformation due to S_2 tidal potential. Note that the equator and the S_2-disturbed Earth elliptical profile, viewed perpendicular to the ecliptic, are not in the same plane.

frequency, a review of orbit perturbation theory is needed. In general, perturbations are caused by the noncentral Earth's gravitational field. Apart from these, other forces such as the gravitational attraction of the Sun and Moon, the radiation pressure of the Sun and the drag of the atmosphere, also cause perturbations (Kaula 2000). The Earth's gravitational disturbing potential can be represented by (3.13) and (3.14) with spherical harmonic coefficients $l \geq 2$, and the corresponding perturbation spectrum is $\dot{\psi}_{mp}$. Note that a nominal orbit is assumed. Furthermore, the definition of p is different from that in (Kaula 2000), c.f. section 3.4. Nevertheless, the assumption of nominal orbits does not affect the analysis and the derived conclusions afterwards, compared to a more realistic orbit setting.

Any gravitational field functional such as orbit (position and velocity, or Keplerian elements), low-low intersatellite range and range can be written as (3.13) under the assumption of semi-analytical theory. For instance, satellite orbits are perturbed, relative to the circular orbit, with *dominant* secular precession (zero-frequency with $m = p = 0$) and *small* periodic oscillation at frequency $\dot{\psi}_{mp}$. Resonance occurs when $\dot{\psi}_{mp} \approx 0$ and the periodic variation is more significant so that there may be libration rather than secular motion (Kaula 2000). To summarize and emphasize, forward modelling starts with a given set of

K_{lm} with $l \geq 2$ and results in the secular and periodic functional $f^{\#}$. Backward modelling is to derive the K_{lm}, *which conveys only spatial information but no temporal information for a single solution*, based on the time series $f^{\#}$.

Actually, the perturbation theory was initially developed based on an implied condition, *the static field*. The temporal property of gravity fields started to be widely investigated and applied only after GRACE mission was launched and the time series of the fields were analysed. Therefore, the spherical harmonic coefficients K_{lm}, derived from the perturbation theory, by definition and by nature represent the spatial but no temporal characteristic of a field.

The temporal characteristics of ocean tides can be considered by inserting (3.15) and (3.14) into (3.13), assuming $\psi_{mp}(t_0) = 0$. That is, the geopotential functionals due to periodic ocean tides can be written as

$$f^{\#} = \sum_{m=-\infty}^{\infty} \sum_{p=-\infty}^{\infty} \sum_{l=\max(|m|,|p|)}^{\infty} H^{\#}_{lmp} \sum_{k} \sum_{+}^{-} \left(\bar{C}^{\pm}_{lm,k} \mp i \bar{S}^{\pm}_{lm,k} \right) e^{\pm i \dot{\Theta}_k t} e^{i \dot{\psi}_{mp} t} . \tag{3.22}$$

Rewriting (3.22) by separating retrograde and prograde waves gives

$$f^{\#} = \sum_{l,m,p} H^{\#}_{lmp} \sum_{k} \left[\bar{K}^{+}_{k,lm} e^{i\left(\dot{\psi}_{mp} + \dot{\Theta}_k\right)t} + \bar{K}^{-}_{k,lm} e^{i\left(\dot{\psi}_{mp} - \dot{\Theta}_k\right)t} \right], \tag{3.23}$$

with $\sum_{l,m,p} = \sum_{m=-\infty}^{\infty} \sum_{p=-\infty}^{\infty} \sum_{l=\max(|m|,|p|)}^{\infty}$, and the corresponding prograde and retrograde coefficients of constituent k are

$$\begin{aligned} \bar{K}^{+}_{k,lm} &= \bar{C}^{+}_{k,lm} - i \bar{S}^{+}_{k,lm} \\ \bar{K}^{-}_{k,lm} &= \bar{C}^{-}_{k,lm} + i \bar{S}^{-}_{k,lm} , \end{aligned} \tag{3.24}$$

and the prograde and retrograde perturbation spectrum of each constituent k are

$$\begin{aligned} \dot{\Psi}^{+}_{k,mp} &= \left(\dot{\psi}_{mp} + \dot{\Theta}_k \right) \\ \dot{\Psi}^{-}_{k,mp} &= \left(\dot{\psi}_{mp} - \dot{\Theta}_k \right) . \end{aligned} \tag{3.25}$$

Equation (3.25) indicates a richer perturbation spectrum compared to the static field, also demonstrated by (Cheng 2002). To be specific, different constituents with prograde and retrograde frequencies are added to the original spectrum $\dot{\psi}_{mp}$ to give new perturbation spectrum $\dot{\Psi}^{+}_{k,mp}$ and $\dot{\Psi}^{-}_{k,mp}$. This means that the forward modelling of $f^{\#}$ depends on a larger number of perturbation frequencies. However, the backward modelling of one set of $(\bar{K}^{+}_{k,lm}, \bar{K}^{-}_{k,lm})$, is equivalent to *a sample* by averaging the spatial-temporal information of the field within a certain period.

In (Cheng and Ries 2017), the authors attempted to describe the temporal characteristics of the gravity fields, namely fields due to periodic ocean tide variation, by the orbit perturbation frequency. This attempt is infeasible as the temporal information of the

fields is merged into one solution as a whole and cannot be tracked back by its resulted-in perturbation frequencies of the functional $f^{\#}$. Only by analysing the time series of the fields, can one get the (distorted) temporal information. Assuming perturbation frequency as the alias frequency is equivalent to describe the spectral property of a time series by a single sample, which is derived by a time series with certain frequencies. This assumption of using a sample to indicating the spectral characteristic of the whole time series is unreasonable in any case.

3.6 Summary

Aliasing in satellite gravimetry occurs in two steps. First, high frequency temporal signals like ocean tides are undersampled by the satellite orbits. Second, the observations are combined globally within a recovery period to derive single gravity field solution, which is a procedure of resampling and possible undersampling, of the signals conveyed in the observations. Figure 3.3 shows the two-step sampling. Table 3.2 shows the related parameters of the two-step aliasing in terms of ocean tides. It should be noted that the secondary alias does not happen for all cases. According to the Nyquist sampling rule, the secondary alias occurs when the recovery period T_r is no less than half of the primary alias period $1/f_\mathrm{a}^\mathrm{p}$. For example, in some cases with a combination of certain orbit sampling pattern and recovery period, some of the tidal constituents will suffer from primary and secondary aliases but some of them may only have a primary alias.

Long period tidal constituents may have secondary alias, as the recovery is an undersampling of original signals, but no "primary alias" as the orbit sampling is not undersampling the signals. In this case, the terms *primary* and *secondary* may not be appropriate. Nevertheless, the basic idea of aliasing in satellite gravimetry is still valid and one can use a similar strategy demonstrated in this study.

Table 3.2: Parameters of two-step aliasing in terms of ocean tides. The frequencies f_sg, f_s and f_a are signal frequency, sampling frequency and alias frequency, respectively.

alias procedure	due to	f_sg	f_s	f_a
primary alias	orbit sampling	f_t	$\omega_\mathrm{E} - \dot{\Omega}$	f_a^p
secondary alias	gravity recovery	f_a^p	$1/T_\mathrm{r}$	f_a^s

For satellite gravimetry, the spatial aliasing and temporal aliasing of the ocean tides can be considered as the two sides of a single problem. Furthermore, perturbation frequency cannot be considered as alias frequency, although the periodic ocean tides variation of the spherical harmonic coefficients are taken into consideration while deriving the perturbation frequency.

Chapter 4

Simulation-based aliasing spectrum analysis

In the previous Chapter 3, the two-step aliasing mechanism in satellite gravimetry is discussed. A brief demonstration of the primary aliasing is given in section 3.3 by showing the distribution pattern of the observations along the orbit in the u-t domain. In this Chapter, the secondary aliasing will be demonstrated by spectral analysis. For this sake, an analysis method called simulation-based aliasing spectral analysis (SBASA) is developed. It is based on the investigation of power spectral density in different regions. Furthermore, it allows us to investigate the aliasing behaviour of a single spherical harmonic coefficient, for instance to analyze the discussion on the 161-day signal in $C_{2,0}$ of GRACE-derived fields (e.g. Seo et al. 2008b; Chen et al. 2009; Cheng and Ries 2017): whether it is due to ocean tide aliasing or not.

The guide-map of this Chapter is as follows:

- Section 4.1 presents the general simulation strategy and setting in this work;
- Section 4.2 introduces the method SBASA to estimate the aliasing spectrum;
- Section 4.3 demonstrates the secondary aliasing by SBASA;
- Section 4.4 investigates the aliasing spectrum for different regions;
- Section 4.5 investigates the behaviour of single spherical harmonic coefficient regarding aliasing;
- Section 4.6 explores the influence of the recovery periods on the aliasing further, based on the discussion in section 4.3, 4.4 and 4.5 ;
- Section 4.7 discusses the relation between wave interference, especially beats, and aliasing frequencies;
- Section 4.8 summarizes this chapter briefly.

4.1 General simulation strategy

From this Chapter on, different simulations are conducted for different purposes. On one hand, these simulations follow a common strategy. On the other hand, different scenarios are designed for specific purposes. A general simulation strategy is introduced here, and the tailored setting is introduced whenever new simulations are activated.

This work in general is to investigate the ocean tide aliasing influence on the recovered gravity field and its functionals. In this sense, the effects of other signals and error sources are irrelevant. In order to avoid external effects, the *inputs* of the simulations are purely ocean tides, either the signals or the errors. No instrumental or observational noise is added to the simulations. Ocean tide signals are usually acquired by one ocean tide model, regardless of its uncertainty. Ocean tide errors are usually obtained by the difference of two ocean tide models, whose level of magnitude may be underestimated or overestimated for different regions comparing to the true ocean tide uncertainty. Nevertheless, the above assumptions are the best approximations for the ocean tide signals and errors which are currently available.

Normally, eight major ocean tide constituents, M_2, N_2, S_2, K_2, O_1, P_1, Q_1 and K_1 are included in the simulations either individually or together. The minor tides are not included for several reasons:

i) global ocean tide models have coverage of mostly the 8 major tides, the minor tides are inferred from the major tide admittances in the presence of non-linearity, which contains errors;

ii) such errors are known to be significant in shallow seas and near-coastal waters for all currently existing global models, which makes the modelling of the minor tide errors more unreliable;

iii) the magnitudes of the minor tides are relative small compared to the detection ability of the current and near-future satellite gravimetry, which is limited by the spatial resolution.

Another property of the simulation is that it runs in *closed loop*. A closed-loop simulation means the true world is known to the simulator. Ideally, the outputs are expected to be the same as the inputs. In reality, they cannot be the same. The errors, misclosure between outputs and inputs, indicate the limitation of designed **system**, satellite formation or constellation, under the condition that no other noise is included. The simulator is a software which simulates the observations and recovers the gravity fields. The observation is a simplified range acceleration by ignoring the correction of perpendicular velocity terms, as already introduced by equation (3.12).

A **system** in this work specially means a formation or a constellation of a satellite mission. Nominal orbits are assumed for all the scenarios. A nominal orbit satisfies the following requirements: circular orbit, constant inclination and J_2 perturbed secularly precessing. Least-squares estimation is applied to derive the gravity field solutions. Table 4.1 summarizes the general simulation setting.

Table 4.1: General simulation setting.

input field	purely ocean tide signal or error
noise	no
ocean tide signal	EOT08a
ocean tide error	EOT08a – GOT4.7
tidal constituent	M_2, N_2, S_2, K_2, O_1, P_1, Q_1, K_1
simulation property	closed-loop
simulator functional	observation simulation and gravity recovery
system	satellite formation or constellation
orbit	nominal orbit
observation	simplified range acceleration: $(\nabla V_B - \nabla V_A) \cdot \vec{e}_{AB}$
recovery method	least-squares estimation

4.2 Simulation-based alias spectrum analysis (SBASA)

As discussed in Chapter 3, normally ocean tides are undersampled by satellite orbits and then further undersampled by the recovery process when the recovery period does not satisfy the Nyquist sampling rule. Therefore, when the input fields of the simulation are pure ocean tides, the output fields are the aliased ocean tides. By spectral analysis of the output fields, aliasing frequencies can be derived. The power spectral density is calculated for spectral analysis. This is the basic idea to analyse the aliasing spectrum of ocean tides based on simulations and spectral analysis. Therefore, a method called *simulation-based alias spectrum analysis (SBASA)* is developed. This method estimates the alias periods based on the recovered gravity field time series, by computing the mean power spectral density (PSD) in terms of geoid height. Figure 4.1 shows the basic idea of SBASA for deriving the mean PSD in terms of geoid height:

1) acquiring tidal gravity field time series with a certain time resolution based on given orbit;

2) expressing the gravity field solutions in geoid height with specific spatial resolution;

3) forming the time series for each grid cell;

4) computing PSD for each grid cell time series;

5) averaging the derived PSD over certain region.

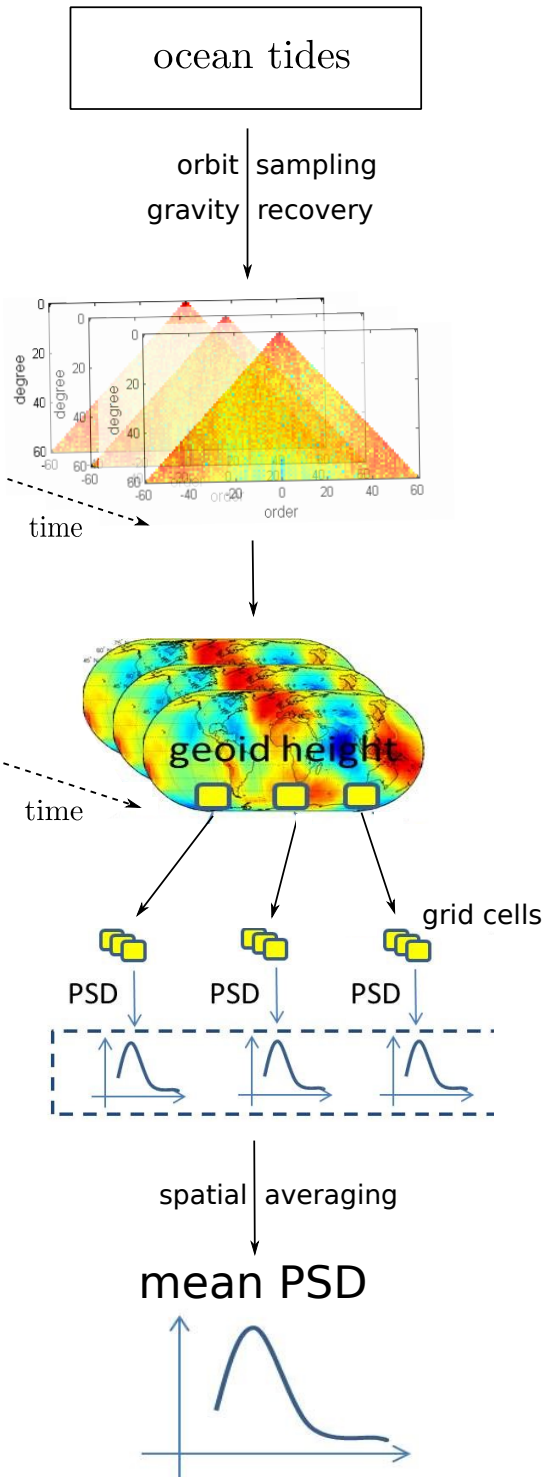

Figure 4.1: Simulation-based alias spectrum analysis.

4.3 Demonstration of secondary aliasing period

SECONDARY aliasing is due to the undersampling during the recovery process. In this demonstration, two scenarios are simulated: one is a GRACE-type formation; the other one is a Bender-type (Bender et al. 2008) constellation. A Bender-type constellation is composed of two pairs of GRACE-type low-low satellite-to-satellite tracking formations, with a polar pair and an inclined pair. See Table 4.2 for the parameter setting of the simulation scenarios.

Table 4.2: Simulation scenario.

scenario	single pair	double pair	
formation/constellation	GRACE-type	Bender-type	
	polar pair	polar pair	inclined pair
β/α	172/11	172/11	460/29
inclination	92°	92°	115°
altitude	362 km	362 km	342 km
input field	ocean tide error: EOT08a – GOT4.7		
tidal constituent	individual M_2, N_2, S_2, K_2, O_1, P_1, Q_1, K_1		
recovery period	11 days		
mission duration	5 years		

A repeat orbit is assumed for both GRACE-type and Bender-type scenarios, which means the orbits repeat after α nodal days and β revolutions. The parameters α and β are coprime positive integers. Notice that the repeat-orbit design is one way to guarantee an *absolute* homogeneous distribution of groundtracks within a α nodal days. However, the homogeneity of the groundtracks can be a relative loose constraint for the discussion of secondary aliasing, that is, *absolute homogeneity* is not a necessary requirement. Therefore, exact repeat orbits are not needed normally. Nevertheless, the repeat orbits are chosen at this stage of demonstration to simplify the case study. More advanced scenarios will be discussed later in this chapter and next chapter.

Figure 4.2 shows the global mean PSD of individual constituents for GRACE-type and Bender-type scenarios. As the input field is an individual tidal constituent, the spectral analysis of the recovered gravity fields indicates the aliasing spectrum of each corresponding constituent. Table 4.3 shows the primary and secondary aliasing periods of the simulated scenarios derived by the two-step aliasing analytical method and the main spectral line indicated by SBASA, see Figure 4.2. *It is shown that the secondary aliasing periods of the polar pair and the inclined pair coincide with the alias period derived by SBASA for most cases with an accuracy of up to 3 days, which demonstrates the secondary period well.* The inconsistent cases are marked in red. Comparing the T_a^s to T_a^{SBASA}, one can find that the smaller the aliasing period is, the closer they are. This is because of the fact that, for

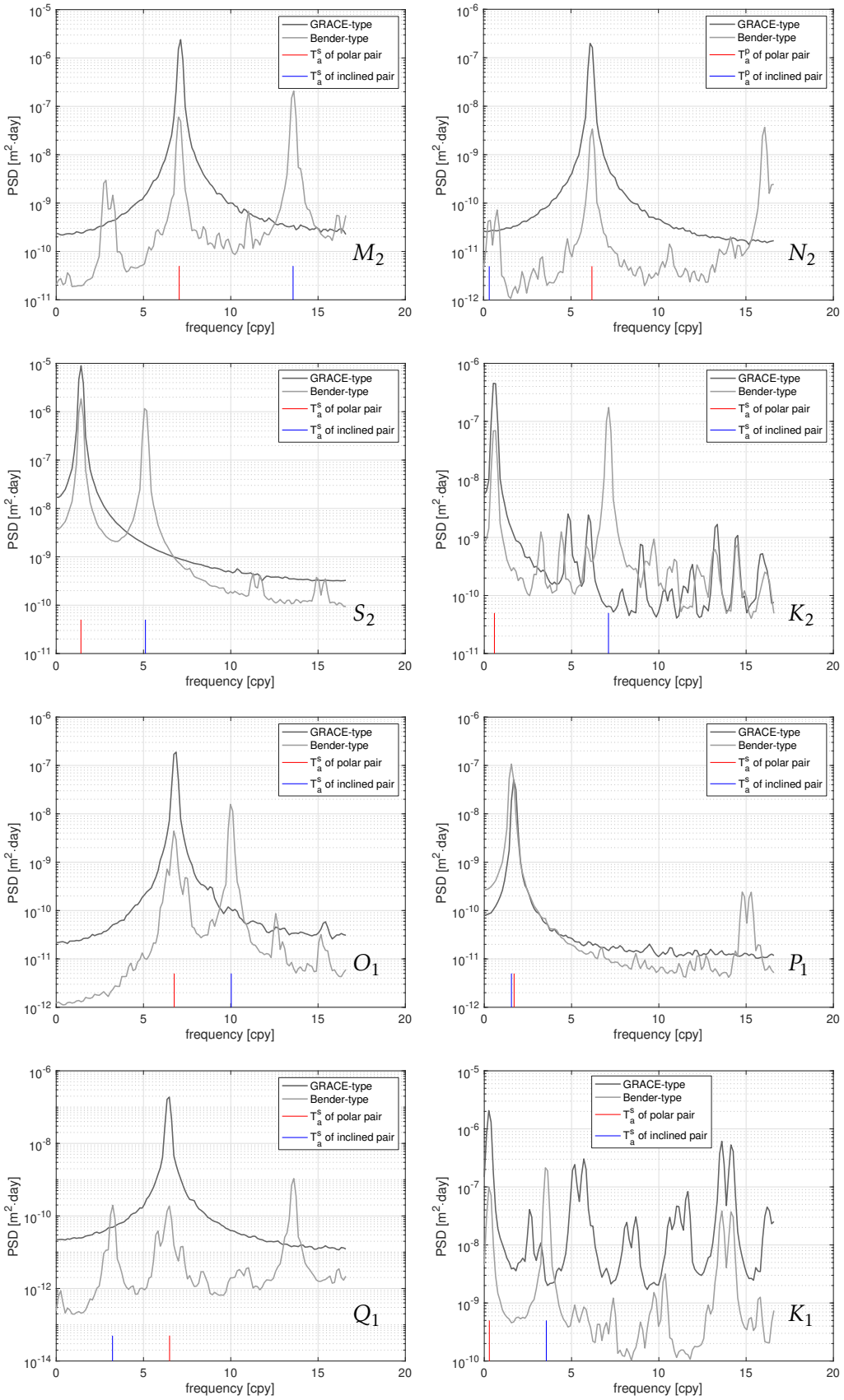

Figure 4.2: Global mean PSD of individual constituents.

the spectral analysis of the discrete signal, the ratio R_{lp} between the length of signal and the period of signal affects the spectral detecting accuracy. To be specific, larger R_{lp} can guarantee a better estimation of the spectrum of the discrete signal. This partly explains why T_a^s and T_a^{SBASA} do not match for the red marked scenarios, especially for the constituent K_2 and K_1 under the sampling of polar pair. With further insight and discussion, the abnormal phenomena in N_2 and P_1 can be fully explained in section 4.4 and 4.6.

One should also notice that the secondary alias periods of every individual pair appear for the Bender-type in most cases. In other words, although double-pair constellation combines the data sampled from two different orbit planes, sampling of individual orbit plane is well observed and is not coupled with each other. Therefore, the understanding of single pair orbit sampling can be applied to double- or multi-pair constellation. See more general discussion in section 4.7.

Table 4.3: Alias periods [day] of the simulated scenarios estimated according to the two-step aliasing and SBASA.

constituent	polar pair		inclined pair		GRACE-type	Bender-type	
	T_a^p	T_a^s	T_a^p	T_a^s	T_a^{SBASA}		T_a^{SBASA}
M_2	14.0	51.8	18.6	26.9	51.2	51.2	26.8
N_2	9.3	58.9	11.1	1115.8	58.7	58.7	22.7
S_2	257.5	257.5	71.4	71.4	256.0	256.0	72.2
K_2	628.0	628.0	51.3	51.3	563.2	563.2	51.2
O_1	13.8	54.0	15.8	36.4	54.2	54.2	36.6
P_1	213.7	213.7	234.5	234.5	216.6	–	234.7
Q_1	9.2	56.2	10.0	113.1	56.3	56.3	112.7
K_1	1256.0	1256.0	102.7	102.7	1408.2	1408.2	104.3

4.4 Aliasing for different regions

The discussion above was based on the spectral densities that were globally averaged. Figure 4.3 shows the aliasing of M_2 constituent derived by mean PSD of different regions, namely the whole globe, the Amazon, and three latitude bands. The reason to include a purely continental catchment like Amazon is because the spherical harmonic expression of the ocean by nature causes leakage of ocean tide signal onto the continent, as discussed in Chapter 2 and Chapter 3. Therefore, the same alias spectrum of the ocean tides is expected on the continent. We can see that the aliasing periods of different regions are consistent for both GRACE-type formation and Bender-type constellation, apart from slightly changed energy magnitude due to the averaging.

Figure 4.4 and 4.5 show the mean power spectral density of 8 constituents for different latitudes. For each constituent, the top panel refers to the GRACE-type scenario and the

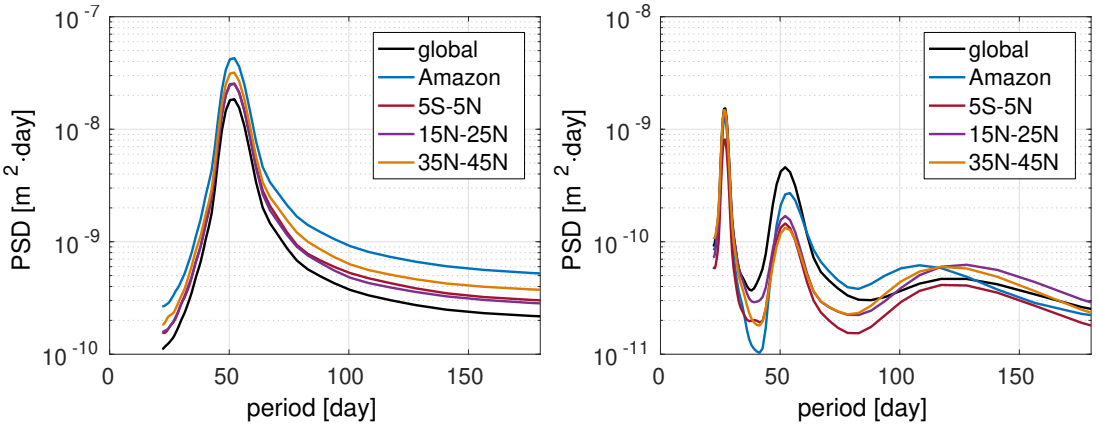

Figure 4.3: Alias periods derived by mean PSD of different regions (left: GRACE-type, right: Bender-type).

bottom panel to the Bender-type scenario. Please notice the different scale of the color bars for each plot. By analysing the PSD plots in Figure 4.4 and 4.5, several characteristics are observed.

First, all the latitudes show the same aliasing spectrum for each constituent of both scenarios for most cases. Less obvious lines at higher latitudes can be observed by scaling the power spectral density (PSD) for each latitude by its maximum per latitude. See a normalized PSD for M_2 constituent in Figure 4.6. The high energy at some latitudes means less reduction due to the recovery averaging process, which can be traced back to the *orbit sampling effects* over the tidal constituents. The *orbit sampling effect* regarding individual constituent is the combined result of two effects: (1) the density of the groundtracks, and (2) the phase sampling over the tidal constituent. These two aspects are not totally independent. More groundtracks raise the opportunity to improve phase sampling, i.e. towards more homogeneous distribution, which make the resulted magnitude smaller when averaging them, and vice versa. However, this relation is not in an absolute sense. For example, the groundtrack density has a significant influence on the high latitude when the orbit is polar or near polar. That is, for most constituents (M_2, N_2, K_2, O_1, Q_1, K_1) of GRACE-type scenarios, the high latitude (beyond $\pm 60°$) has relative low energy compared to the other latitude. However, this is not exactly the case for S_2 and P_1. The energy distribution of the S_2 GRACE-type scenario shows asymmetry between the the northern hemisphere and southern hemisphere, which should have the same groundtrack pattern at the corresponding symmetry latitude. For the P_1 constituent, highest energy shows up at latitudes beyond-60° towards the south pole, but not at the corresponding latitudes towards the north pole. This demonstrates that the overall tidal phases at the sampling epochs play a very important role in magnitude reduction.

Secondly, part of the aliasing frequencies of Bender-type scenarios align with the aliasing frequencies of GRACE-type scenarios, which shows the same pattern as the global mean

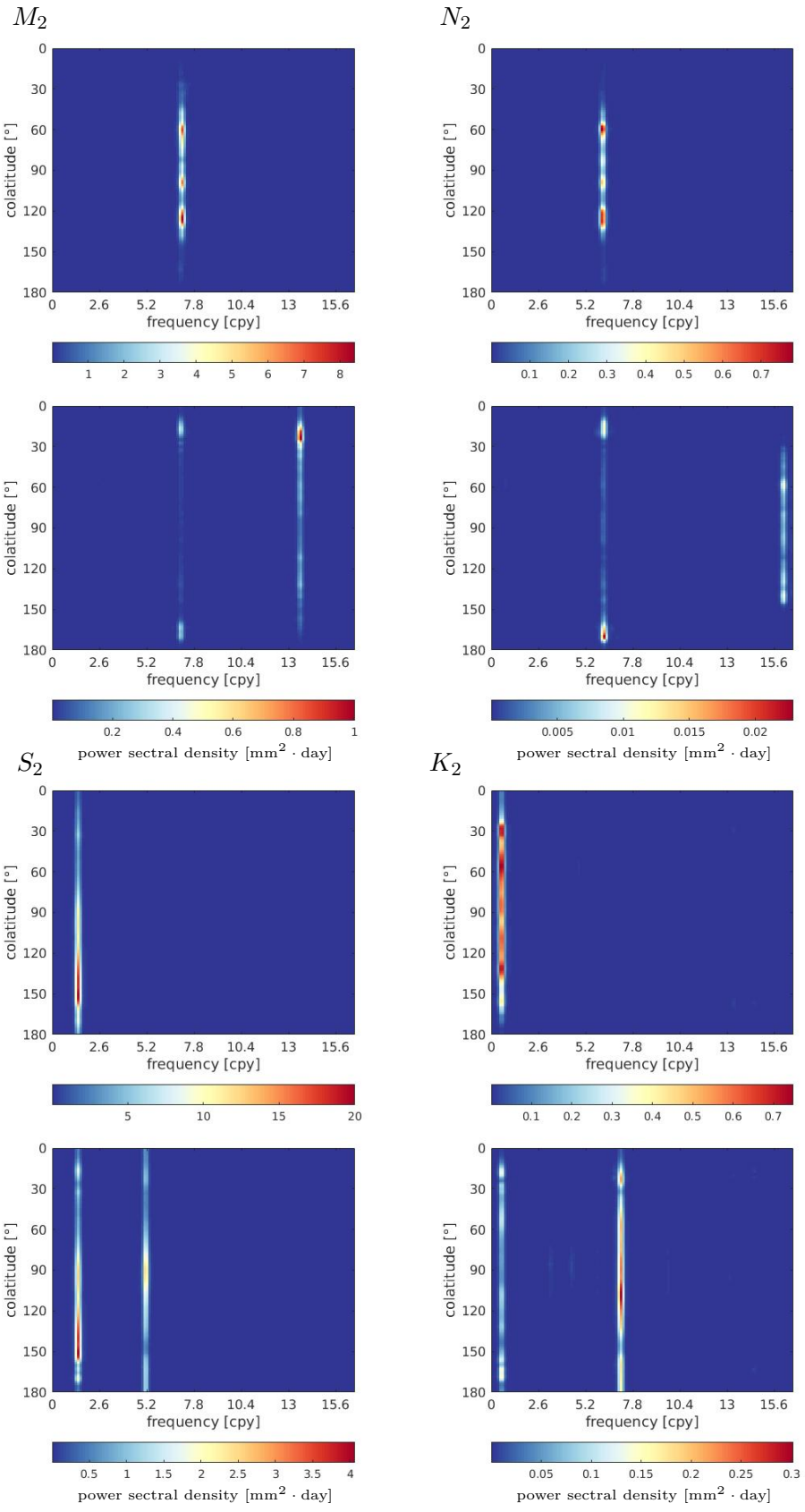

Figure 4.4: Mean power spectral density of each latitude for semi-diurnal tides. For each constituent, the top is from GRACE-type and the bottom is from Bender-type. Please note the different scales in the colorbars.

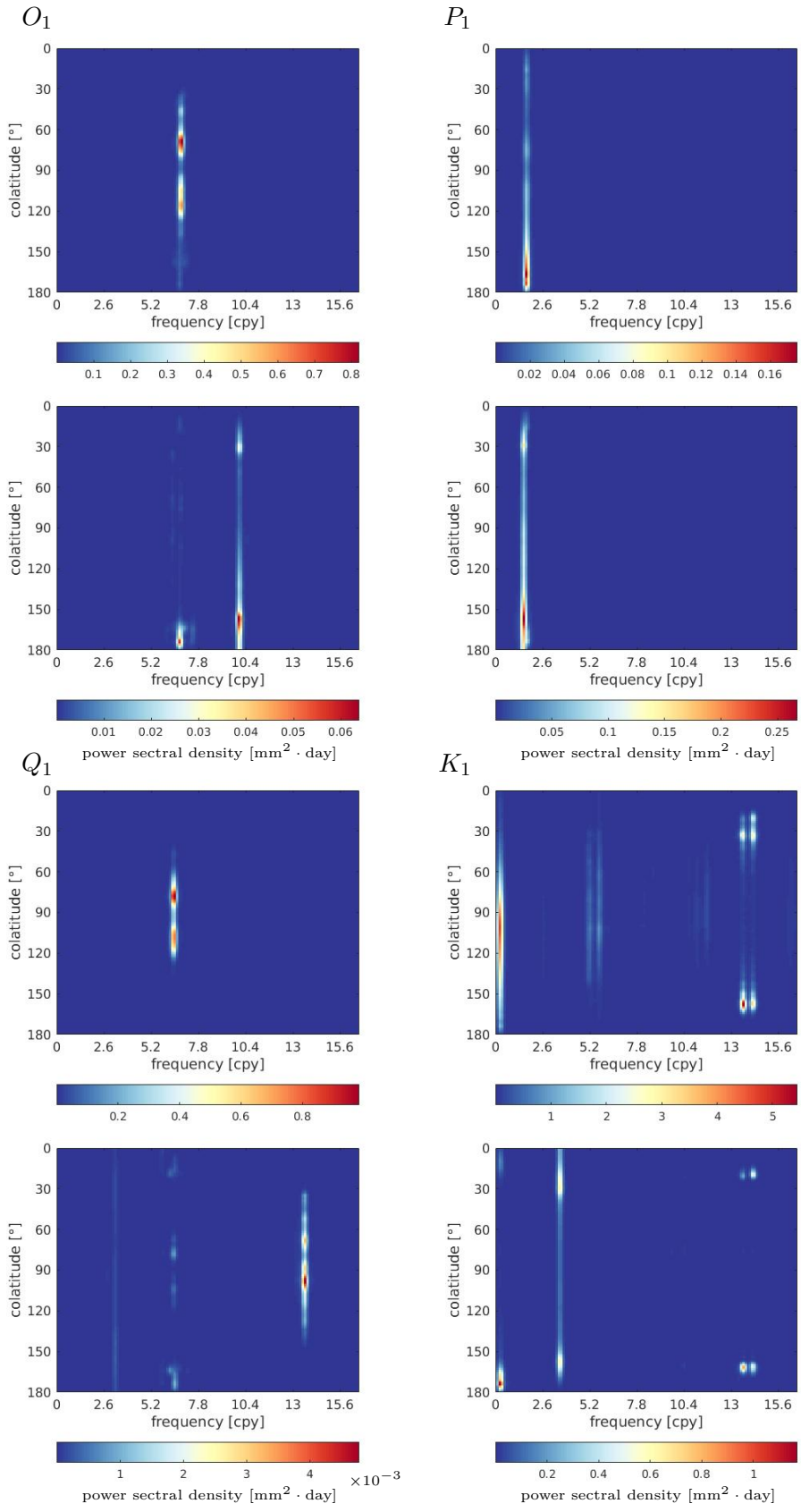

Figure 4.5: Mean power spectral density of each latitude for semi-diurnal tides. For each constituent, the top is from GRACE-type and the bottom is from Bender-type. Please note the different scales in the colorbars. Be aware that 10^{-3} multiplier is only applied on the colorbar of Bender-type of Q_1 constituent.

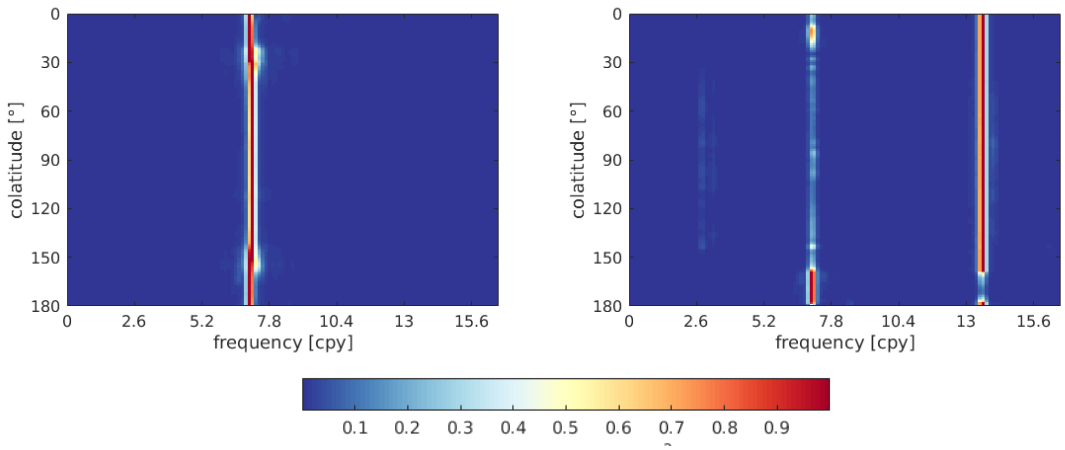

Figure 4.6: Scaled power spectral density of each latitude for M_2 constituent, the left one is GRACE-type and the right one is Bender-type.

PSD distribution. Apart from that, the latitude-mean PSD is consistent with global-mean PSD, cf. Table 4.3, Figure 4.4 and 4.5. This proves that the global mean does not compress or distort the spectrum. Therefore, the global mean represents the spectrum that is derived by spatial time series fields sufficiently.

Thirdly, a richer spectrum can be found in the Bender-type P_1 scenario compared to the GRACE-type, as the spectral "line" of the former is slightly wider than the latter. Therefore, the absent aliasing period of Bender-type $T_{\mathrm{a}}^{\mathrm{SBASA}}$ (see Table 4.3) can be explained. That is, the low frequency resolution of the spectral analysis "merges" the two aliasing frequencies of inclined pair and polar pair. Actually, this follows the signal separation quantified by the **Rayleigh criterion**. The Rayleigh criterion for tides argues that two signals can be separated only when they differ in phase at least by one cycle over the analysed time span (e.g Smith 1999):

$$T_{\mathrm{Ray}} \left| f_{\mathrm{a}_1} - f_{\mathrm{a}_2} \right| \geq 1 \,, \tag{4.1}$$

in which T_{Ray} is called Rayleigh period, f_{a_1} and f_{a_2} are two aliasing frequencies. To separate the aliasing period 213.7 days and 234.5 days, the secondary aliasing periods of polar pair and inclined pair (see Table 4.3), more than 6.6 years are needed. A simulation with 5 years is obviously not enough. The inconsistency of K_2 and K_1 can also be explained similarly, that is, the *real* secondary aliasing periods calculated by the analytical formula cannot be separated from the *virtual* aliasing periods estimated with spectral analysis.

4.5 Aliasing of single spherical harmonic coefficient

One may have a question regarding the SBASA: why not calculate the aliasing period via spectral analysis on spherical harmonic coefficients? We know that the geoid height is a linear combination of spherical harmonic coefficients, so alias periods derived

by mean PSD in geoid height should be equivalent to the alias period derived in spherical harmonic domain. This section investigates the aliasing spectrum by directly analysing the time series of spherical harmonic coefficients. Figure 4.7–4.10 show the scaled PSD of all coefficients, the order mean and the degree mean, which are corresponding to the left column, the middle column and the right column. The overall coefficients are arranged in order-wise, namely C_{l0}, S_{l1}, C_{l1}, S_{l2}, C_{l2} and so on. The scaling is performed for each single coefficient, degree or order by its maximum. The scaled PSD is preferred because the coefficient energy of different degree and order varies over several orders of magnitude, which is not good for the visualization.

In general, the analysis of spherical harmonic coefficients presents a richer spectrum than the spatial analysis, comparing Figure 4.7–4.10 to Figure 4.4 and 4.5. One of the reasons could be that the normalized power spectral density makes the frequencies with weaker energy emerged. Nevertheless, the pattern in the coefficient-frequency plots confirms the tiny peaks in global mean PSD plots in Figure 4.2, especially the "twin" peaks, two peaks close to each other with almost the same magnitudes, shown in the plots of e.g. Bender-type of S_2, P_1 and K_1 as well as GRACE-type of K_1.

The spectrum lines are "fuzzy" in the all-coefficient plots (left column), which may indicate a hidden pattern in degree-wise or in order-wise. This speculation is confirmed by the degree-mean or order-mean vs frequency plots. Usually, a smoother spectrum is seen in the middle and left column plots. That is to say, some frequencies are order-dependent and some frequencies are degree-dependent. For example, for Bender-type of S_2 scenario, the alias period around 71.4 days is more order-dependent and the alias period about 257.5 days is more degree-dependent.

Another interesting point is that the energy does not always spread equally to the whole degree or order span at a certain frequency. The energy can be high-degree dominant (e.g. M_2 of Bender-type), low-degree dominant(e.g. N_2 of Bender-type), high-order dominant or low-order dominant (e.g. two periods from Q_1 of Bender-type). Nevertheless, this mostly happens to the Bender-type scenarios, which may be due to the difference in orbit sampling of inclined pair within subsequent 11-day periods. For the GRACE-type formation, the same power of certain aliasing frequency is seen for all the coefficients for most constituents (K_2 and K_1 are the exceptional). If 161 days is the aliasing period of the S_2 tide sampled by GRACE, it should persist for all the spherical harmonic coefficients, including $C_{2,0}$. Whether the corresponding tidal signal can be observed or not, depends on the relative power of the aliasing signal to the other geophysical signal.

As two exceptions, the energy of K_2 and K_1 spreads out from single secondary aliasing frequency to many frequencies even with GRACE-type scenarios. Both K_2 and K_1 have relative large aliasing periods and therefore inaccurate spectral estimates, as already discussed in section 4.3 and 4.4. The limited accuracy of frequency detection due to data

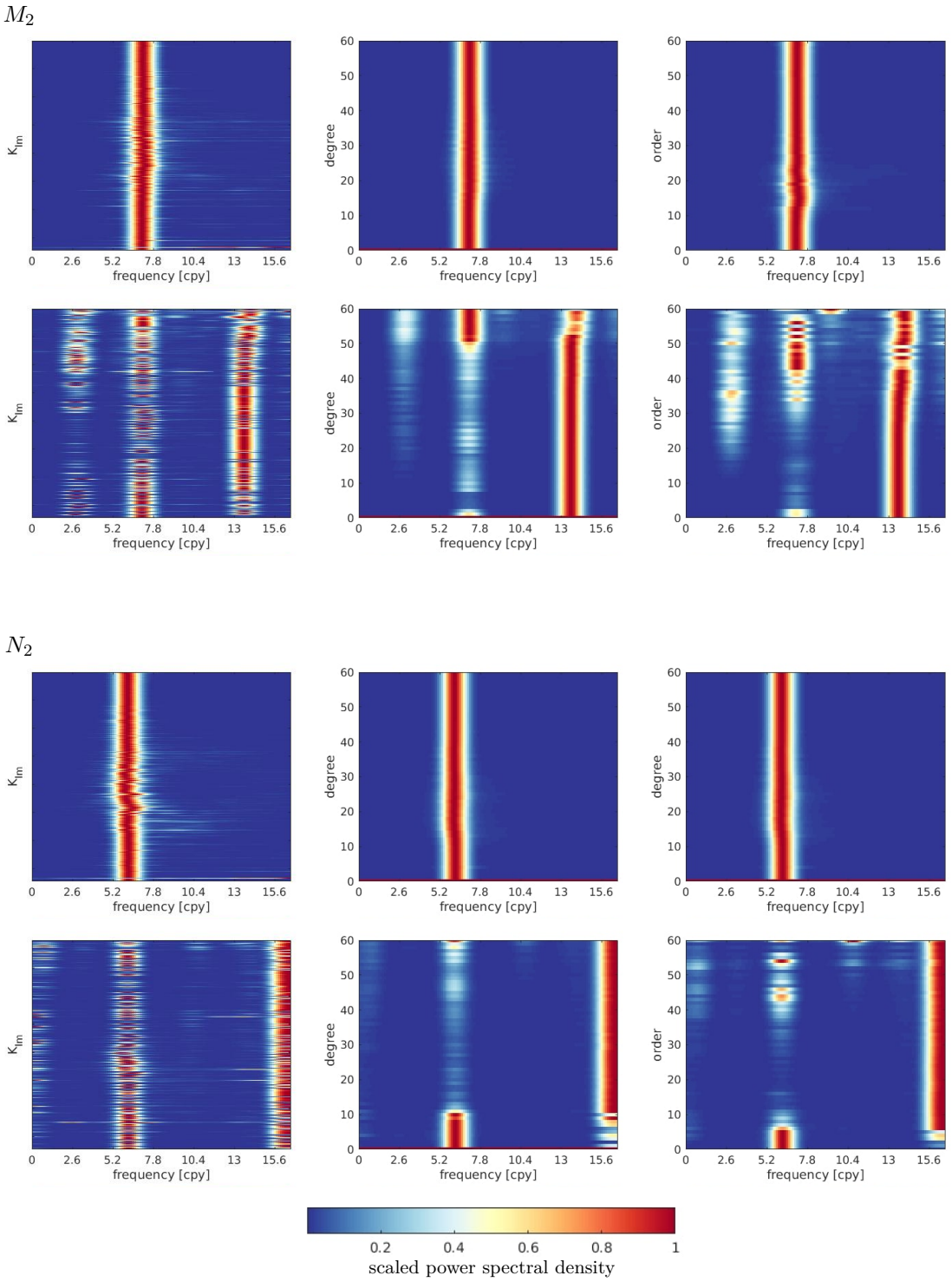

Figure 4.7: Scaled power spectral density of individual spherical harmonic coefficient, degree mean and order mean. For each constituent, the top row is the GRACE-type scenario, the bottom row is the Bender-type scenario.

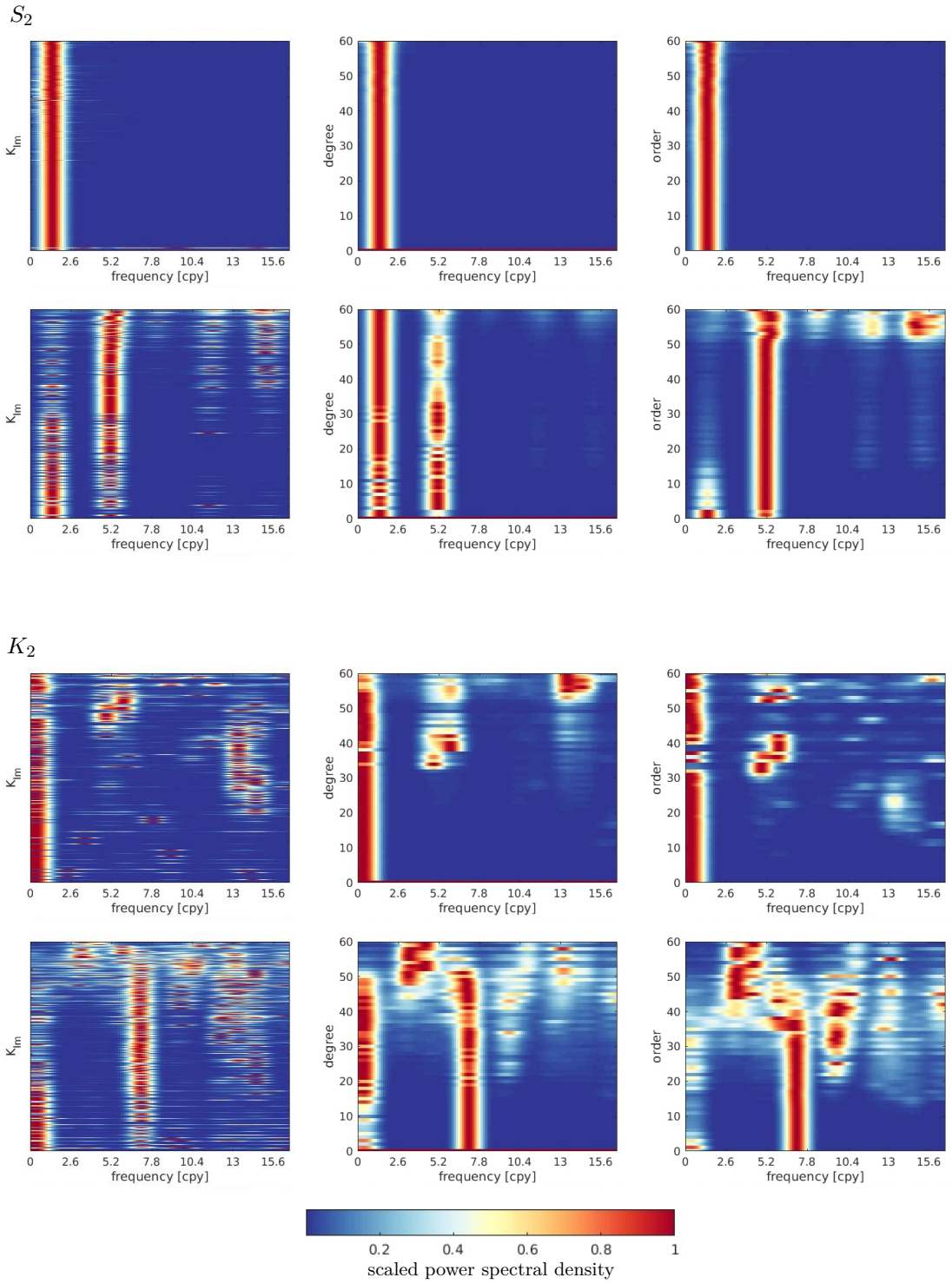

Figure 4.8: Scaled power spectral density of individual spherical harmonic coefficient, degree mean and order mean. For each constituent, the top row is the GRACE-type scenario, the bottom row is the Bender-type scenario.

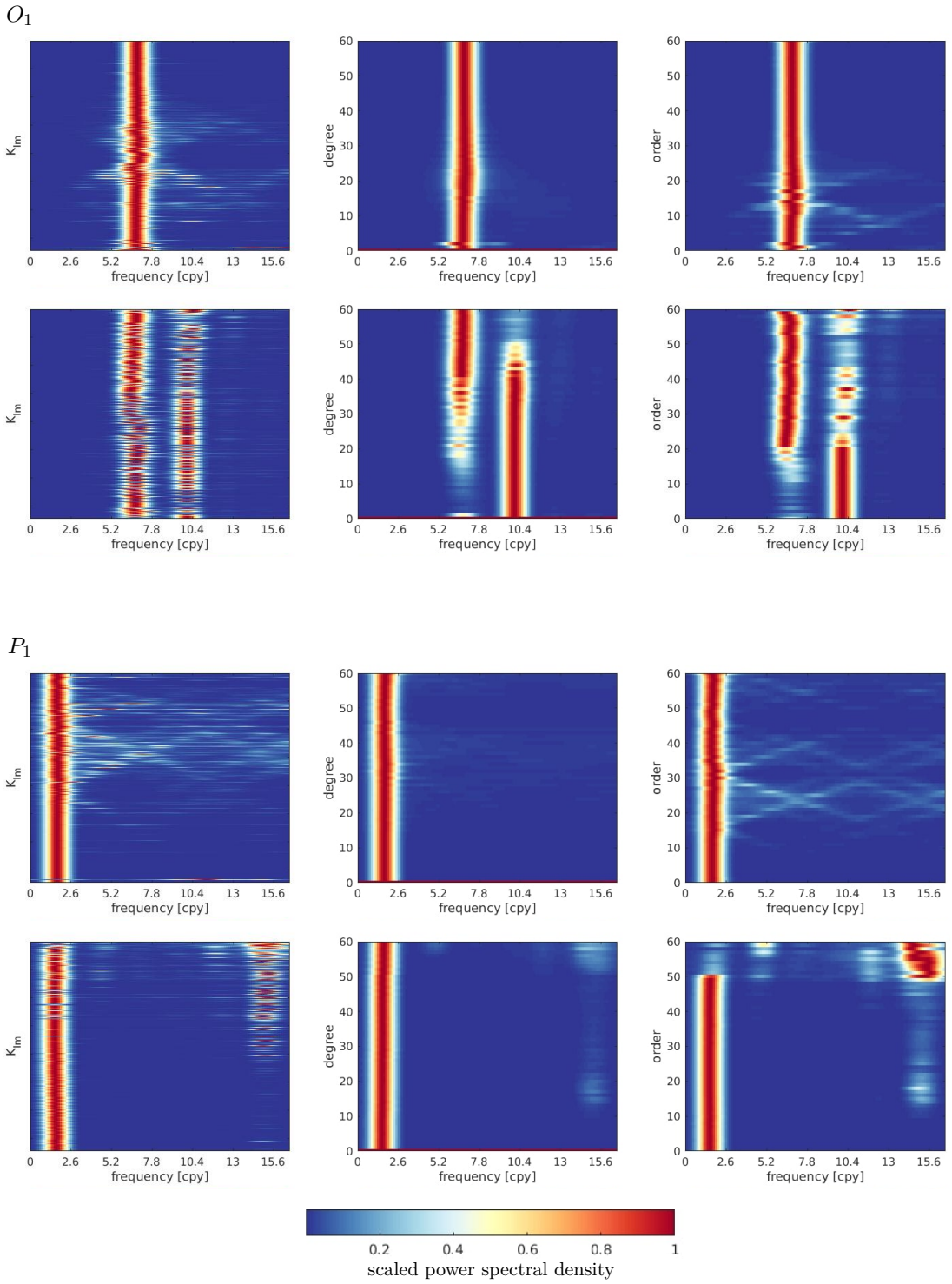

Figure 4.9: Scaled power spectral density of individual spherical harmonic coefficient, degree mean and order mean. For each constituent, the top row is the GRACE-type scenario, the bottom row is the Bender-type scenario.

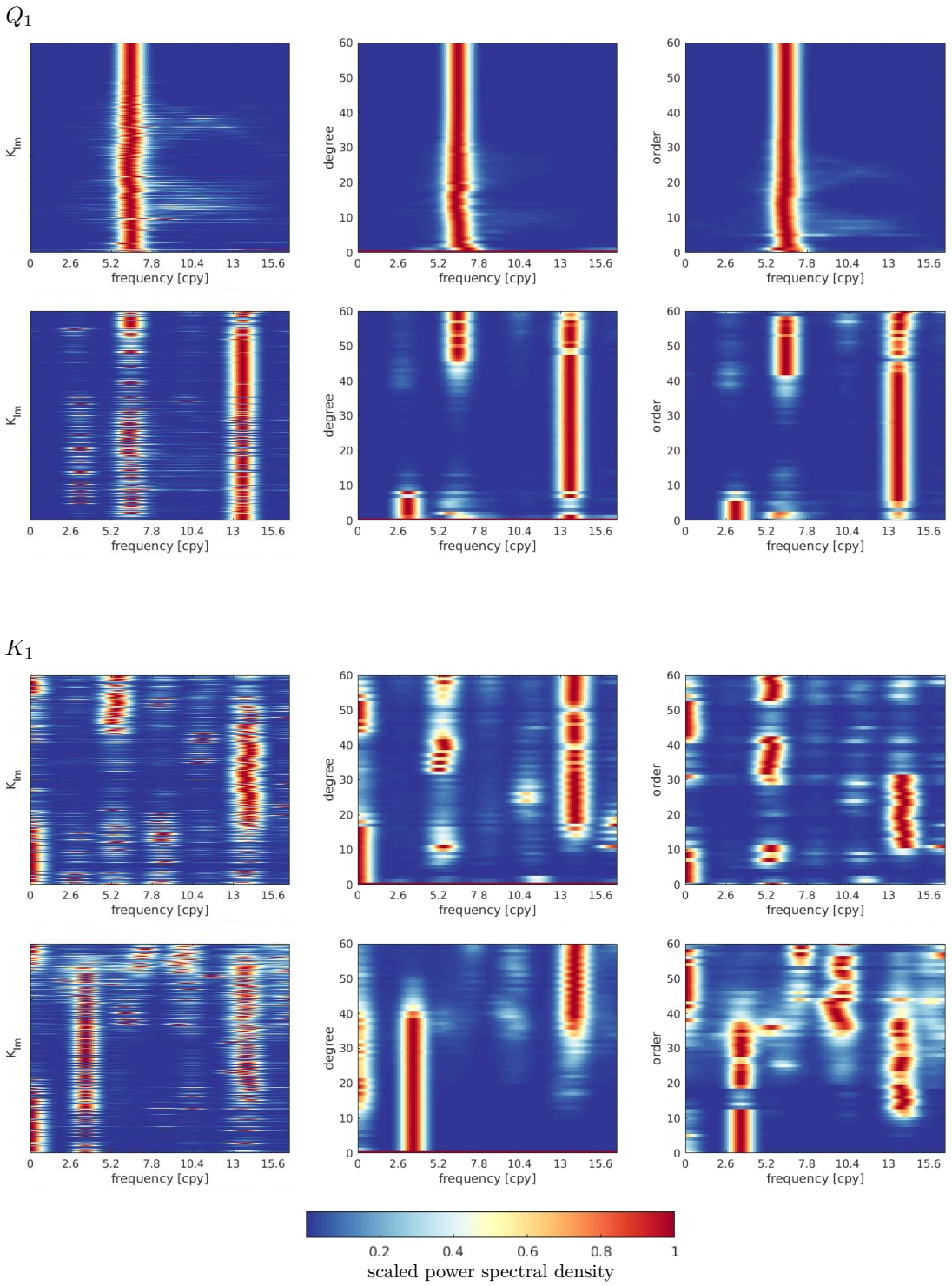

Figure 4.10: Scaled power spectral density of individual spherical harmonic coefficient, degree mean and order mean. For each constituent, the top row is the GRACE-type scenario, the bottom row is the Bender-type scenario.

length may cause the energy of certain frequency leak to other frequencies while applying spectral analysis.

4.6 Recovery periods vs orbit sampling: more complex cases

In the previous three sections, the discussion and demonstration is based on the concept of repeat orbits. However, as already mentioned in section 4.3, repeat orbits, or the absolute homogeneity of groundtracks, is not a necessity for the secondary aliasing discussion. In this section, the understanding of the secondary aliasing is explained in a more general sense.

To understand secondary aliasing fully, the first question could be what is the real meaning to take the recovery period as the secondary sampling period. As we know, gravity recovery from satellite missions *combines* data from different regions and different epochs to derive global solutions. For a single solution, the maximum degree and order of the spherical harmonic coefficients indicate the spatial resolution and the recovery period indicates the temporal resolution. The *combination* can be considered as an averaging process for the data within different spatial scales and within the recovery period. However, the recovery period only marks the sampling interval in the time domain "automatically", which is naturally correct as the temporal aliasing is the research objective. The averaging outcomes do not come automatically with a given recovery period.

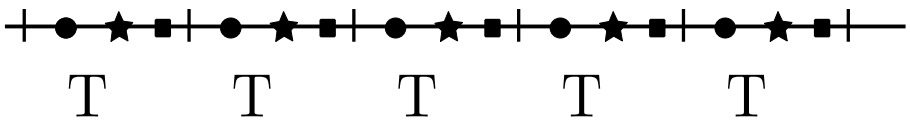

Figure 4.11: Sketch map of the sampling interval.

Let us start with the most simplified situation. A simple example is given by Figure 4.11. Suppose the horizontal line indicates a continuous signal in time domain. The constant T's stands for a time span between two neighbouring vertical lines. Corresponding to the gravity recovery, T is equivalent to the recovery period and the overall representation of this time period T is equivalent to one gravity field solution. The assumed epoch of the solution can be anywhere within the time span T as long as the spacing of the successive solutions is kept in T. It means either type of the marker in Figure 4.11 is accepted as the epoch marker.

The above-mentioned example is a pure temporal sampling without consideration of the averaging process within the period T. When a certain temporal averaging within each

interval T is taken into account, the averaging strategies should be considered. As long as the averaging strategies are the same for all the investigated time periods, the averaging itself does not change the spectrum property of the signal, that is: (1) the averaged signal has the same spectral lines as the original signal; (2) the same sampling frequency applied to both averaged signal and original signal gave same aliasing frequencies.The complexity of aliasing pattern increases when the averaging strategies are different for different averaged periods, which may happen when spatial averaging is involved. This is exactly the case of gravity recovery, which contains three aspects:

1) **sampling interval**: the recovery period;

2) **temporal averaging** within the recovery period;

3) **spatial averaging** based on the spatial sampling, namely the groundtrack distribution pattern.

Notice that the above three aspects are coupled and the induced effects cannot be separated easily. However, a discussion of individual aspect sequentially in a more general sense helps understanding the coupled case better.

The reason of the added complexity due to spatial averaging is that it has the potential to change the spectrum of averaged signal comparing to the original signal when the spatial sampling is not consistent among different recovery periods. One case is that the recovery period does not equal the repeat period of the repeat orbits. In this case, the groundtrack pattern of different recovery periods can be either very similar or largely different depending on whether: (1) the recovery period is a subcycle of the repeat period; (2) the recovery period is an (approximate) integer multiple of the repeat period. If the groundtrack pattern is similar, then the averaged signal will be similar to the original signal in terms of spectral characteristics. Otherwise, the spectrum of the averaged signal can be largely different from that of the original signal.

Figure 4.12 shows an example of a sinusoid wave and its averaged results depending on different averaging strategies. The original signal, y, and its averaged, $y1$, $y2$ and $y3$ in time domain are shown at the top panel, the spectrum of all signals is shown at the bottom panel. Different types of averaging are applied as follows:

- $y1$: moving averaging with a constant window length $L\mathrm{w} = 2.5T$;
- $y2$: moving averaging with a regularly changed window length, $L\mathrm{w} = xT$, with x varying from 0.1 to 2.5 repeatedly with a step of 0.2;
- $y3$: moving averaging with a randomly changing window length, $L\mathrm{w} = xT$, with x varying randomly between 0.1 and 2.5,

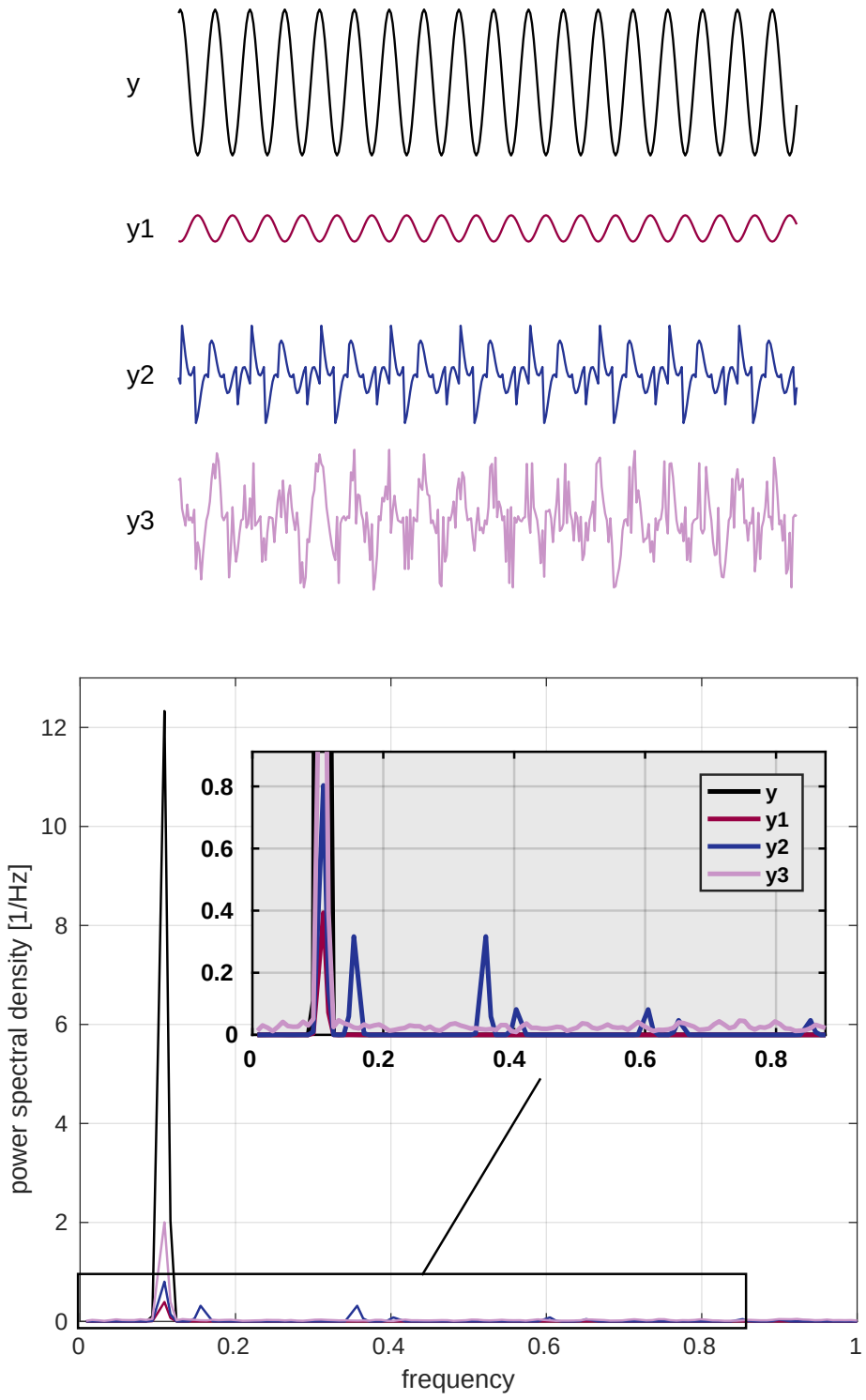

Figure 4.12: A sinusoid signal and its averaged results. The top panel is the signals in time domain, the bottom is the spectrum of corresponding signals. Among all the signals, y is the original signal, $y1$, $y2$ and $y3$ are the moving average of y, with the averaging window length as a constant ($y1$), regularly changing ($y2$) and randomly changing ($y3$). To be specific, the window length can be expressed as $L_w = xT$, in which T is the period of the original signal, and $x = 2.5$ ($y1$), x changing from 0.1 to 2.5 repeatedly with a step of 0.2 ($y2$) and x changing randomly between 0.1 and 2.5 ($y3$).

in which T is the period of the original signal y. From Figure 4.12 we can see that in general averaging causes a reduction in amplitude (top) and therefore a reduction of the total energy (bottom). Averaging with consistent window length does not change the spectral characteristics, comparing $y1$ with y. However, averaging with changing window length causes the spectrum to change, comparing $y2$ and $y3$ with y.

Notice that only averaging is involved for the above example, sampling is after the averaging and is conducted on the averaged signal. For the gravity field recovery, the groundtracks pattern within each recovery period is very important. If the groundtracks distribute inhomogeneously and inconsistently for different recovery time span, it means different averaging strategies are applied among different recovery solutions, similar to or even more complex than $y2$ and $y3$. Therefore, the averaged signal spectrum is different from the original signal spectrum, normally changing from single frequency to multi frequencies. Undersampling of the multi-frequency signal makes the aliasing much more complex, as the multi frequencies cannot be predicted easily and therefore the aliasing frequencies cannot be estimated accordingly.

For a specific example in gravity recovery according to the phenomenon discussed above, the following simulations are conducted, as shown by Table 4.4. The corresponding secondary aliasing frequency can be estimated according to the recovery period (if we ignore the averaging effects temporarily), see Table 4.5. Figure 4.13–4.15 show the power spectral density of the different recovery periods. From Figure 4.13 we can see that the spectrum of the recovered fields time series is largely different among different recovery period solutions. Except for $T_{\mathrm{sol}} = 14$, the secondary aliasing frequencies of all other scenarios, derived by the two-step aliasing mechanism, are all consistent with the aliasing spectrum at low degree and order. Please be aware that the recovered fields are the outcome of the aliasing fields of the input ocean tide errors. In other words, the spectrum of the solution time series contains the aliasing frequencies. Figure 4.13 also shows that the averaging reduces the total power dramatically when the recovery period increases from 5 days gradually up to 120 days.

Figure 4.14 and 4.15 show the main spectrum as indicated by the latitude-frequency plots (Figure 4.13) as well as other frequencies regarding individual coefficient, degree mean or order mean. For 11-day or 22-day recovery, the "integer" times (1 or 2) of the repeat period guarantee the same groundtracks pattern for different recovery solutions, therefore the same spatial averaging is guaranteed for different solutions and *an approximately single* aliasing frequency is seen. This is corresponding to the simplified case of $y1$ in Figure 4.12. An approximately single frequency rather than an absolute single frequency is seen because the repeat period is 11 *nodal days* and the recovery period is 11 or 22 *solar days*. Because of the difference between nodal day and solar day, 11 and 22 solar days are not an *exact* multiple of 11 nodal days. The slight difference causes the aliasing frequency shift slightly for the coefficients with order about 10–30.

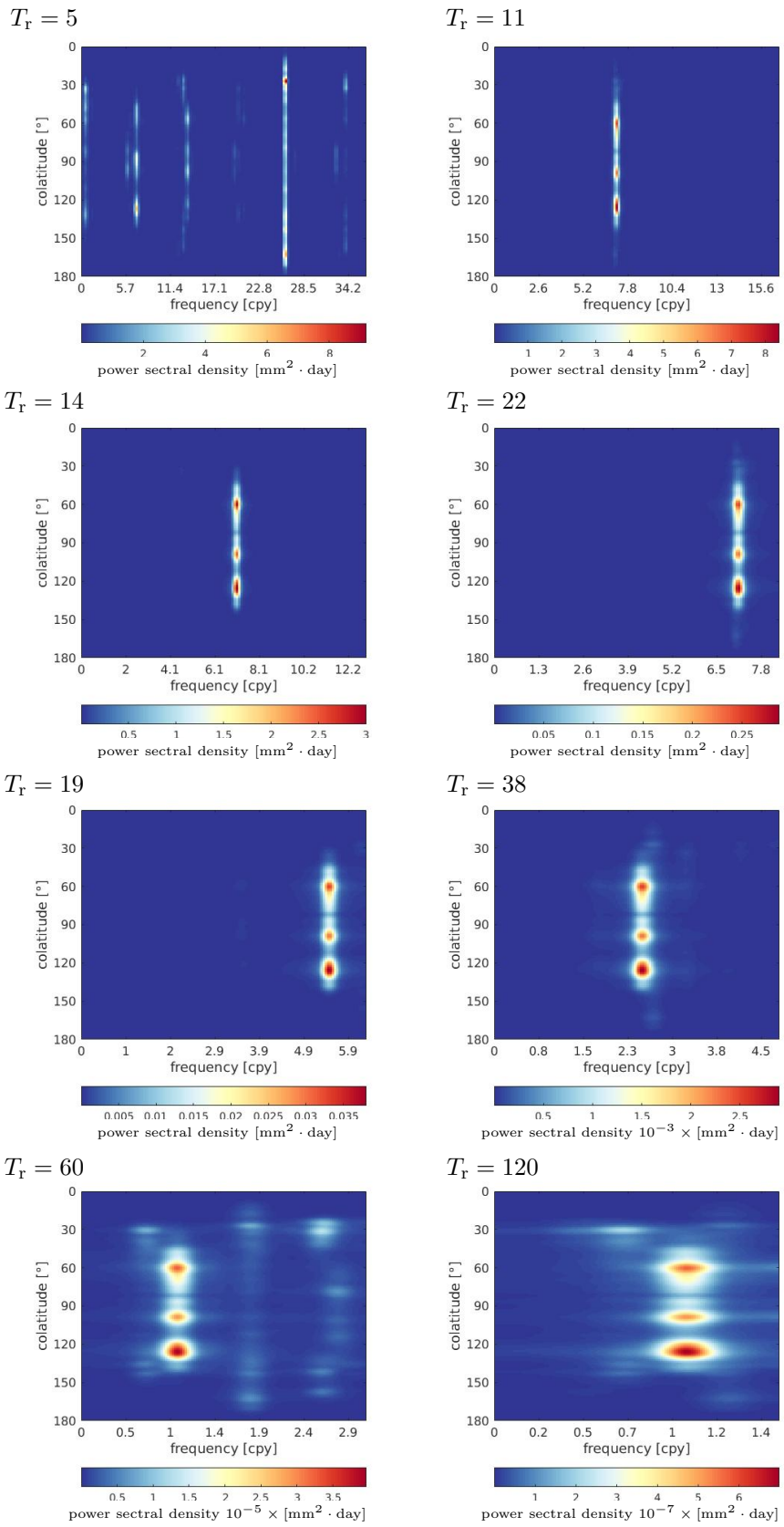

Figure 4.13: Mean power spectral density of each latitude for different recovery periods. Please note the different scales of the colorbars and frequency axis.

Table 4.4: Simulation setup for different recovery periods.

scenario	RPS
formation	GRACE-type
β/α	172/11
inclination	92°
altitude	362km
input field	EOT08a-GOT4.7 7
tidal constituent	M_2
recovery period [day]	5,11,14,22,29,38,60,120
mission duration	5 years

Table 4.5: Secondary aliasing periods for different recovery periods of scenario RPS.

T_r [day]	5	11	14	22	29	38	60	120
T_a^s [day]	14.0	51.8	5521.8	51.8	378.2	136.3	202.3	295.0

For the remaining recovery periods, richer spectra are shown in Figure 4.14 and 4.15. Different from the latitude-frequency PSD, which suppresses the frequencies with low power, the coefficient-frequency PSD shows the influence of the different groundtrack pattern on the aliasing spectrum of coefficients. To be specific, the spectrum is separated for different degree and order. Shorter recovery period (5 days) produces the richest spectrum as (1) the groundtrack coverage different from solution to solution, and (2) less averaging effect comparing to the longer recovery periods. However, although the power is largely reduced by strong averaging, longer recovery periods still have the rich spectrum as the groundtrack patterns of different solutions are different. Actually, the Bender-type scenarios discussion in previous scenarios is a case in point, as the repeat period of the inclined pair is 23 nodal days and the recovery period is 11 solar days.

To summarize, three aspects affect the secondary aliasing in satellite gravimetry:

- the recovery period,
- the temporal averaging within the recovery periods, and
- the spatial averaging within the recovery periods.

The recovery period can be easily understood as the sampling interval, i.e. the sampling frequency. Usually, sampling is applied directly on the signal. However, in the gravity recovery context, the sampling is applied on the averaged signal. In this case, the average strategies should be the same among different recovery periods to keep the spectrum of the averaged signal unchanged compared to the original signal. During gravity recovery, the average is composed of two parts: temporal average and spatial average. Regardless of the spatial characteristic of the gravity field, the temporal averaging remain the same

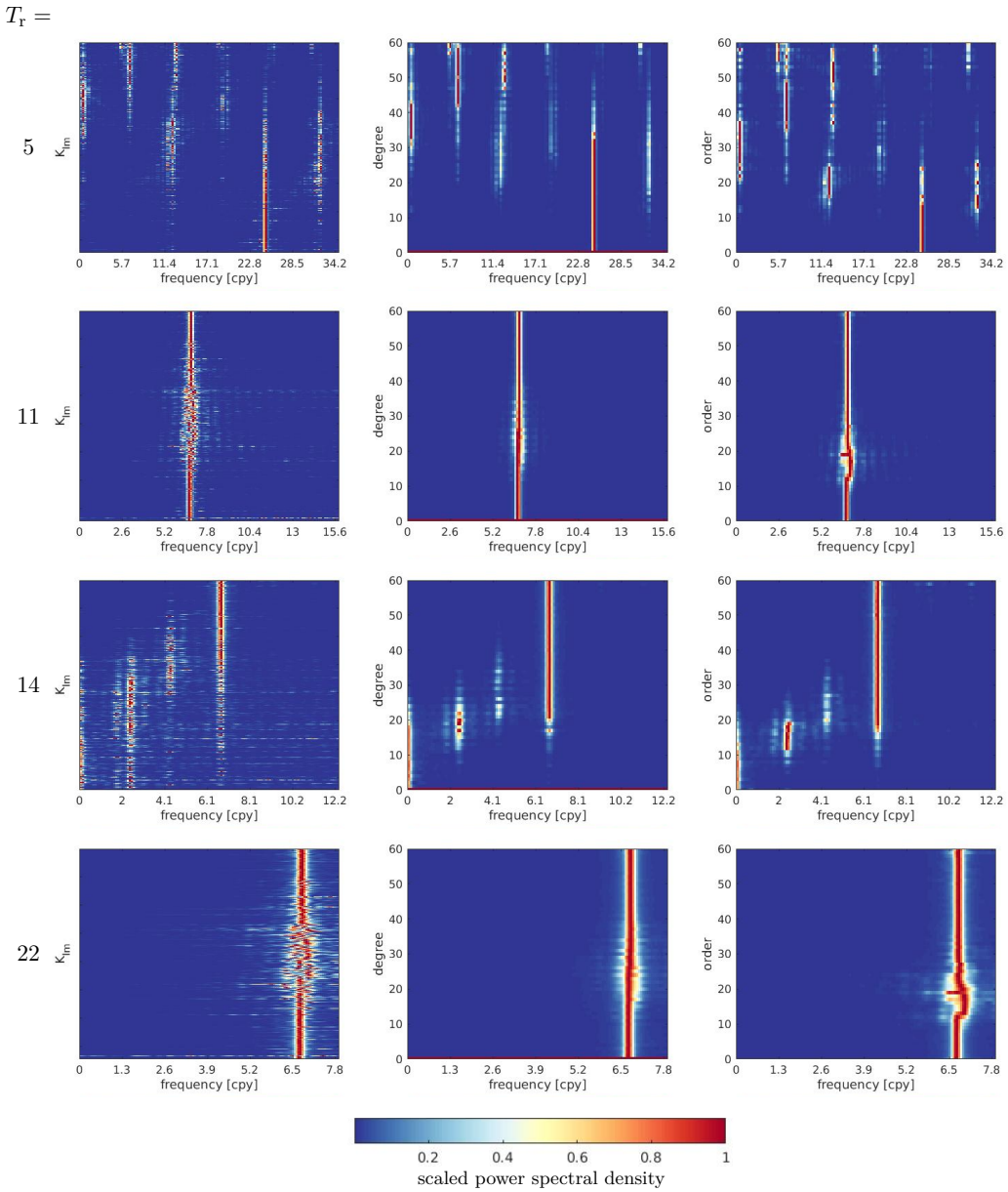

Figure 4.14: Normalized power spectral density of individual spherical harmonic coefficient, degree mean and order mean for different recovery periods, $T_r = 5, 11, 14, 22$. Please notice the different scales of the frequency axis.

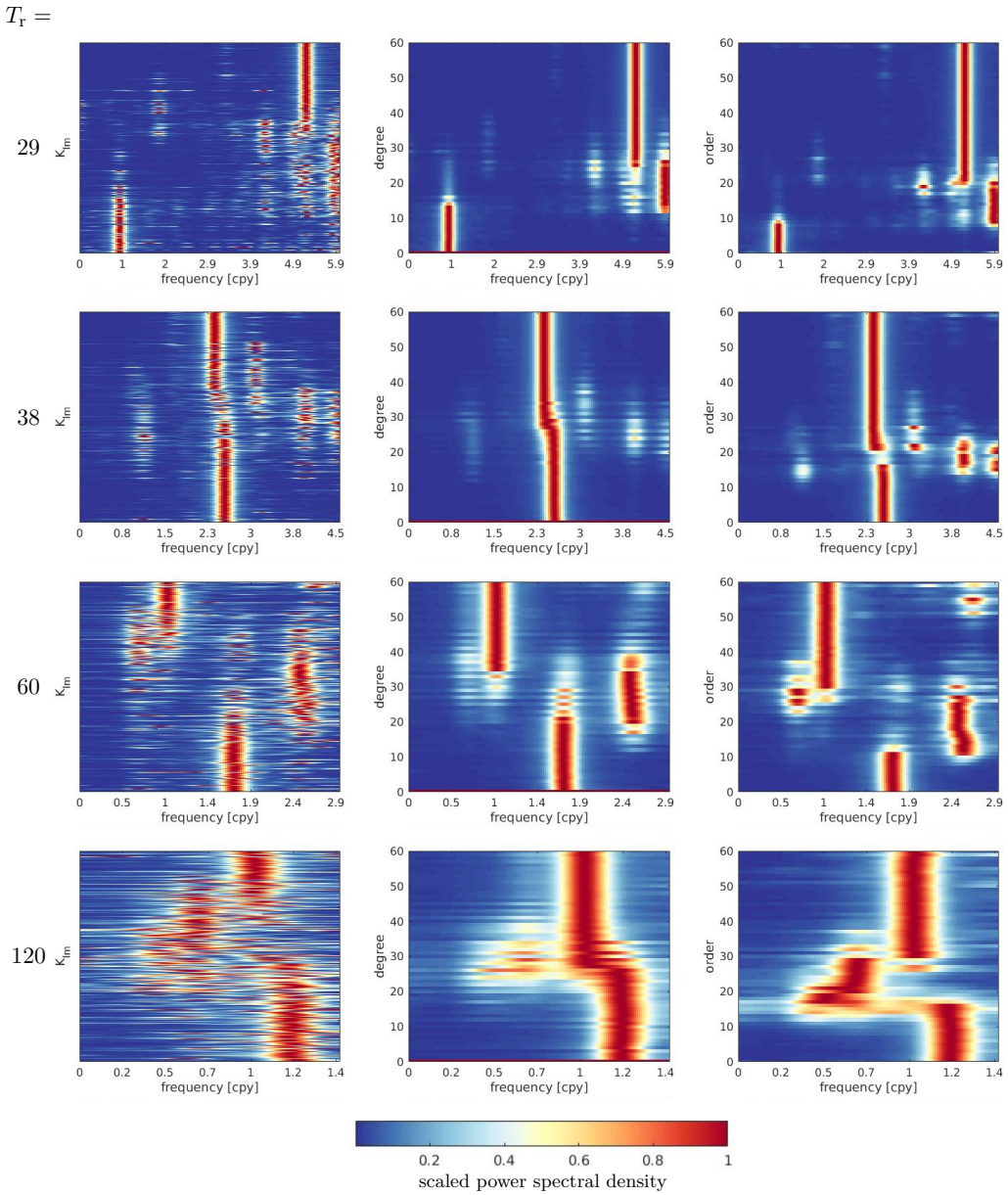

Figure 4.15: Normalized power spectral density of individual spherical harmonic coefficient, degree mean and order mean for different recovery periods, $T_r = 29, 38, 60, 120$. Please notice the different scales of the frequency axis.

when the recovery period remain the same, for instance N-day recovery for the whole investigated time.

Considering the spatial characteristic, one can find that the averaging strategy cannot always be kept the same when the recovery period is a constant N. The spatial distribution of the groundtracks, meaning the spatial sampling of the original fields, must be taken into account. Only when the groundtrack patterns are kept the same among different solutions, can the average strategies be called the same. *Therefore, the secondary aliasing caused by the recovery period sampling is coupled with the orbit sampling by the overall groundtrack sampling pattern within each recovery period.* The secondary aliasing frequency estimate is valid under the condition that the groundtrack patterns among different recovery periods are the same to some extent. Either a changing recovery period or a changing groundtrack pattern within a certain constant recovery period is not feasible for the secondary aliasing frequency estimation by equation (3.19).

4.7 Beats and aliasing

It is easy to connect the double-pair sampling scheme with the phenomenon of *wave interference*. Therefore, whether interference plays a role in double-pair sampling and aliasing should be investigated. Wave interference is a phenomenon in which two waves meet while travelling along the same medium and superpose to form a resultant wave. A special example in case is the *beats* in acoustics. A beat is an interference pattern between two waves of slightly different frequencies, perceived as a periodic variation in volume with the rate, beat frequency, as the difference of two frequencies. Figure 4.16 shows examples of general wave interference and beats. In the case of double-pair scenarios, the aliasing frequency of individual pair can be considered as the frequency of a single wave. Two assumed waves of certain aliasing frequencies can form an interference. In terms of the resulted aliasing error magnitude, similar to the volume in acoustics, it can be enhanced or reduced. However, in terms of the frequency of aliasing error, spectral analysis of the interference product gives the frequency of individual wave. This is also demonstrated by comparing column 3, 5 with 7 and 8 in Table 4.3. Therefore, although the sampling of two different pairs can be considered as the interference of two waves for each constituent, *this interference does not change the nature of the sampling by individual pair*. The aliasing frequency can be derived individually for each pair. This can be extended to more than two pairs: *the aliasing frequency can be derived independently for each pair which forms the multi-pair constellation*.

Furthermore, nearby aliasing frequencies of two constituents sampled by the same orbit, for instance the preliminary aliasing periods of M_2 and O_1 for a polar pair, can also form beats. Beats are the summation effect and do not affect the aliasing of the individual constituent. When two frequencies are too close, the estimated coefficients have high

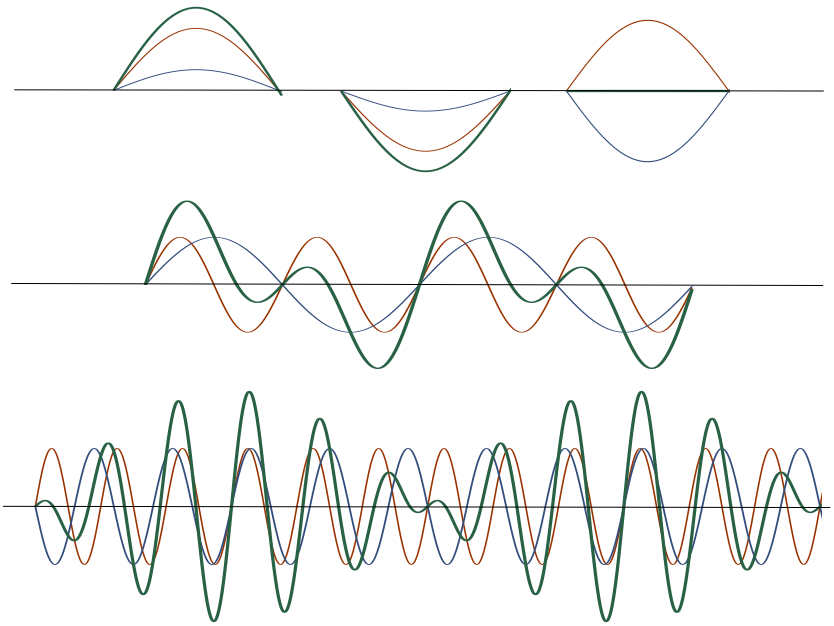

Figure 4.16: Wave interference and beats. The thick green lines are the interference (superposition) of the thin red and the thin blue. The interfered wave (green) can be either enhanced or reduced (top). The middle plot shows a general example of wave interference. When the frequencies of two waves are close, a beat occurs (bottom) and the beat frequency equals the frequency difference of the two original signals.

correlation which makes the separation of according constituents more difficult. If the aim is to remove the aliasing errors, wave interference never hurts the results. If the aim is to subtract the ocean tide signals, one should consider the difficulty of the separation quantified by Rayleigh criterion (4.1).

4.8 Summary

At the beginning of this chapter, the overall simulation setting for the whole thesis is elaborated. Following that, the SBASA method to estimate the aliasing frequency is introduced. Afterwards, the secondary aliasing is cross-validated by the spectral analysis of the gravity field time series. The PSDs regarding global mean, latitude mean, individual coefficient, degree mean and order mean demonstrate the secondary aliasing estimated by two-step aliasing mechanism for most cases. The exceptional cases happen when the simulation period is not long enough for the spectral analysis to derive a reliable estimation of the spectrum. The underlying conditions are discussed for using equation (3.19) to estimate the secondary aliasing frequency, that is: the spatial and temporal averaging should not change the spectrum characteristic of the averaged signal comparing to the original signal. In specific, the groundtrack patterns of different recovery periods should not have large differences. Considering the aliasing signal as a wave with aliasing

frequency, two waves of close aliasing frequencies can form beats. Those two waves can be either from the same constituent sampled by two different orbits or from the different constituents sampled by the same orbits or different constituents sampled by different orbits. The formed beats do not affect the individual wave, and aliasing analysis can be conducted on individual constituent and individual satellite pair.

Chapter 5

Aliasing error mitigation in post-processing

Ocean tide aliasing errors can be *mitigated* in three ways: (1) co-estimating the tides in the recovery process, (2) estimating and removing the errors in post-processing, and (3) designing a mission with a self-dealiasing property. Co-estimating is not the scope of this work. Orbit design will be discussed in next chapter. This chapter discusses the tidal aliasing error mitigation based on the aliasing frequencies *in post-processing*. To be specific, section 5.1 introduces the mitigation methods in the spatial domain and the spectral domain. Section 5.2 estimates the aliasing errors for the scenarios simulated in Chapter 4 and analyses the results. In the end, section 5.3 discusses all the cases and summarizes the keys to better remove the ocean tide aliasing errors.

5.1 Method

Mitigation of ocean tide aliasing errors in post-processing is to remove the aliasing errors from the recovered solutions. The aliasing errors can be estimated in two ways: either in the spherical harmonic domain, namely based on K_{lm}, or in the spatial domain at individual grid cells.

K_{lm}-based de-aliasing De-aliasing in the spherical harmonic domain is feasible because the spherical harmonic expansion is a *linear* decomposition of the spatial signal, which does not change the inherent frequencies of the decomposed signal. Given the aliasing frequencies of each constituent, the aliasing errors can be estimated by a least-squares analysis of the residuals of the recovered field time series (Visser et al. 2010; Liu et al.

2016). To be specific, the following observation equations are applied:

$$\begin{aligned} C_{lm}(t) &= \sum_{n=1}^{N} [A^n_{c,lm} \cos \frac{2\pi}{T^n_{\mathrm{a}}} t + B^n_{c,lm} \sin \frac{2\pi}{T^n_{\mathrm{a}}} t] \\ S_{lm}(t) &= \sum_{n=1}^{N} [A^n_{s,lm} \cos \frac{2\pi}{T^n_{\mathrm{a}}} t + B^n_{s,lm} \sin \frac{2\pi}{T^n_{\mathrm{a}}} t], \end{aligned} \tag{5.1}$$

where $C_{lm}(t)$ and $S_{lm}(t)$ is the recovered field time series, t is the time in the middle of each T_{r}-day recovery, T^n_{a} is the aliasing period, N is the total number of aliasing periods, amplitudes $A^n_{c,lm}$, $B^n_{c,lm}$, $A^n_{s,lm}$, $B^n_{s,lm}$ are the unknowns to be estimated. After estimating the amplitudes, the corresponding aliasing errors $\hat{C}^{\mathrm{alias}}_{lm}(t)$, $\hat{S}^{\mathrm{alias}}_{lm}(t)$ can be calculated and removed from the original fields $C_{lm}(t)$, $S_{lm}(t)$ to get the de-aliased fields:

$$\begin{aligned} \hat{C}^{\mathrm{dealiased}}_{lm}(t) &= C_{lm}(t) - \hat{C}^{\mathrm{alias}}_{lm}(t) \\ \hat{S}^{\mathrm{dealiased}}_{lm}(t) &= S_{lm}(t) - \hat{S}^{\mathrm{alias}}_{lm}(t). \end{aligned} \tag{5.2}$$

As the input field is only ocean tide for the simulations in this thesis, the recovered fields can be used at the left side of equation (5.1) directly. For real data processing, the left side of (5.1) should be the residual fields $\triangle C_{lm}(t)$ and $\triangle S_{lm}(t)$ by removing static field, either using the mean field of the field time series or a static gravity field model. The residual fields are needed for a better estimation of the aliasing errors because normally the ocean tides aliasing errors are much smaller than the static signals and even the temporal signals like hydrology. However, it should be reminded that if the alias periods are close to relevant periods of the interested temporal signals, the estimation can mistakenly remove such other important signals. Accordingly, the same removed static field should be added back after deriving the de-aliased *residual* fields estimated by equation (5.2).

Spatial-based de-aliasing It is straightforward *in theory* to estimate the aliasing errors in the spatial domain as the ocean tides are spatial signals. However, in practice, de-aliasing in the spatial domain needs more calculation than de-aliasing in the spherical harmonic coefficients. The main procedure is as follows:

1) applying the spherical harmonic synthesis to derive spatial map, e.g. geoid;

2) forming the time series for each grid cell;

3) estimating the aliasing error amplitudes at given aliasing frequencies for each grid cell;

4) calculating the aliasing errors with estimated amplitudes for each grid cell;

5) applying spherical harmonic analysis to derive the aliased spherical harmonic coefficients;

6) subtracting the aliased coefficients from the original coefficients to get the de-aliased solutions.

Similar equations as equation (5.1) can be applied for the step 3), with $C_{lm}(t)$ and $S_{lm}(t)$ replaced by the grid data, e.g. geoid height $N(\theta, \lambda, t)$, at the left side of the equation. Equation (5.2) changes accordingly for step 4). Similar to de-aliasing in the spherical harmonic domain, if the recovered fields contains signals other than ocean tides, a remove-restore procedure should be applied carefully.

5.2 Aliasing errors estimation: case studies

In this section, ocean tide mitigation in the post-processing is investigated. The scenarios under discussion are the GRACE-type formation and Bender-type constellation simulated in Chapter 4. As the input fields are ocean tide errors (see Table 4.2), the recovered fields represent ocean tide errors too. As discussed already, the recovered fields are the joint effect of the orbit sampling and the gravity recovery processing. Orbit sampling affects the recovered fields in two aspects: (1) undersampling of given fields causes aliasing, and (2) the inclination of the orbit indicates the orientation of the observation sensitivity of the ll-SST missions to the gravity fields. The second aspect causes the well-known stripes in GRACE-derived solutions. Gravity recovery processing affects the output fields by the temporal and spatial averaging of the observed fields. The temporal averaging is described by the recovery periods, T_r, and the spatial averaging is described by the spherical harmonic degree and order. Several key points need to be covered and clarified:

- the difference or common ground of de-aliasing in spherical harmonic domain and in spatial domain;
- the relation between aliasing and striping;
- the relation between the primary aliasing and secondary aliasing;
- the relation between the primary/secondary aliasing and the spherical harmonic degree and order;
- the comparison between the GRACE-type formation and the Bender-type constellation regarding the above-mentioned aspects.

In order to compare the K_{lm}-based de-aliasing and spatial-based de-aliasing, scenarios given in Table 4.2 are analysed. All the scenarios are de-aliased on spherical harmonic coefficients and on grid cells separately using the same aliasing periods. The primary aliasing periods T_a^p and secondary aliasing periods T_a^s shown in Table 4.3 (column 2, 3, 4, 5) are used for the de-aliasing procedures by applying equation (5.1) and (5.2) for K_{lm}-based de-aliasing and corresponding modified version for the spatial-based de-aliasing. Figure 5.1 shows degree RMS in geoid height of two constituents, M_2 and K_1. The light

grey lines indicate the recovered fields. The dark grey lines are the fields after spatial-based de-aliasing and the dashed black lines shows the fields after K_{lm}-based de-aliasing. Figure 5.1 indicates that *de-aliasing in spherical harmonic domain and in spatial domain is*

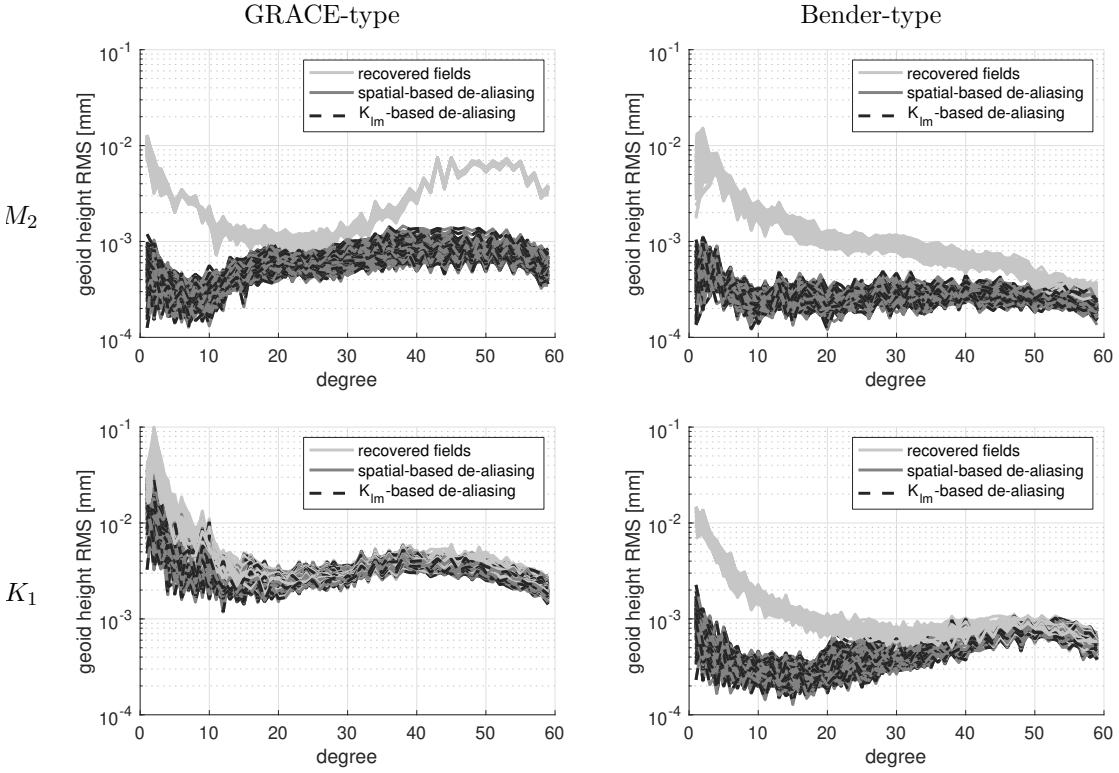

Figure 5.1: Error degree RMS of M_2 and K_1 constituent for GRACE-type formation and Bender-type constellation. The fields are derived from: gravity recovery, de-aliasing with respect to grid cells and de-aliasing with respect to spherical harmonic coefficients.

equivalent when using the same aliasing periods. These results are expected as the spherical harmonic transformation is a linear operation, which does not change the spectral lines. This is also demonstrated by the power spectral density plots in Chapter 4 showing the same major frequencies for a given scenario, either derived regarding latitudes or regarding spherical harmonic coefficients.

In general, de-aliasing in the spherical harmonic domain is more straightforward in practice as (1) the gravity field solutions are usually expressed as spherical harmonic expansion, and (2) it is more convenient to give the de-aliasing fields in spherical harmonic coefficients for further application. By comparison, the spatial-based de-aliasing requires additional spherical harmonic synthesis and analysis. However, de-aliasing in spatial domain may have the advantage of separating the signals between land and ocean, therefore avoiding the disturbance of ocean tide aliasing errors on other physical signals which may have close periods to the aliasing periods. This possible advantage needs

further investigation by more realistic simulations with other temporal gravity fields included, which is out of the scope of this thesis. *The de-aliasing processing is conducted in the spherical harmonic domain from now on.*

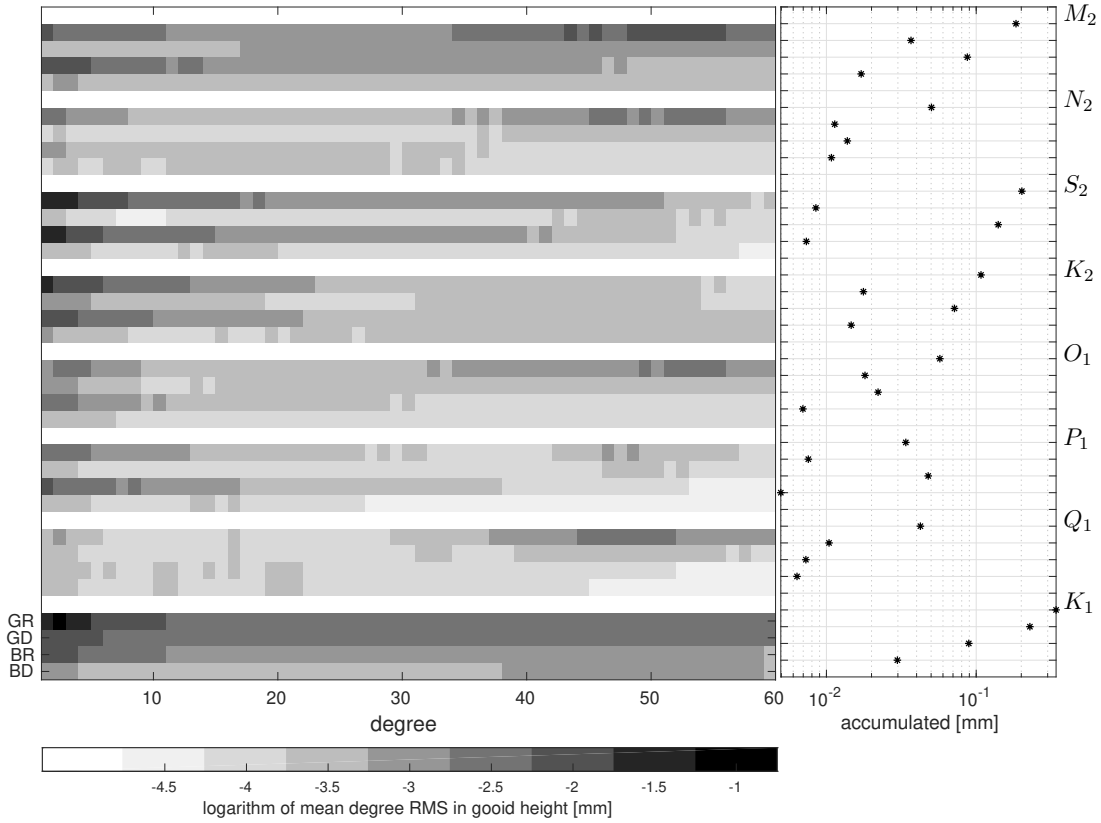

Figure 5.2: Logarithm of mean error degree RMS in geoid height [mm] for 8 major tidal constituents. Each constituent has four fields: GRACE-type recovery (GR), GRACE-type de-aliasing (GD), Bender-type recovery (BR) and Bender-type de-aliasing (BD). The white rows are to separate neigbouring constituents. The constituents are labelled at the right side of the figure. The scatter plot in beteen shows the accumulted mean degree RMS for each field.

Figure 5.1 gives the spectral behaviour of two constituents, in which lower error magnitudes are shown for the de-aliased fields in general. However, for a given constituent, the energy distributions of the aliased fields and de-aliased fields are different for GRACE-type formation and Bender-type constellation. For a given mission, the energy distributions of different constituents are also different. Figure 5.2 shows the mean degree RMS in geoid height for 8 major tidal constituents. Every four rows under a white row represent four fields of one constituent, which is labelled at the right side of the figure. From the top to the bottom, the four fields are: GRACE-type recovery (GR), GRACE-type de-aliasing (GD), Bender-type recovery (BR) and Bender-type de-aliasing (BD). The scatter plot shows the accumulated magnitudes in geoid height for each field. From Figure 5.2

we can see that in general all recovery fields of the Bender-type scenarios have lower error magnitudes than that of the GRACE-type scenarios, comparing the fields BRs with the fields GRs at the left and the accumulated values at the right. However, the better behaviour of Bender-type scenarios do not show up for the whole spherical harmonic spectrum. For instance, one can see the same magnitude for degree 14–24 of M_2, degree 8–29 of N_2, degree 9–15 of S_2, degree 24–53 of K_2, degree 12–29 of O_1, degree 17–28 of P_1 and degree 22–29 of Q_1.

One special constituent is K_1, i.e., the Bender-type scenario is better than the GRACE-type for the whole spectrum. In general, Bender-type constellation is better than the GRACE-type formation at higher degrees, which may be because (1) Bender-type constellations reduce the strong correlation among degrees for a given order, which is shown in GRACE-type fields, and (2) more observations improve the precision of the estimated fields for small regions, corresponding to higher degree. Further investigation is shown later on.

After de-aliasing with respect to the primary aliasing periods and secondary aliasing periods, the errors can be reduced by about 0.5 to 3 levels of magnitude in general. There are some exceptions which show no improvement, e.g.

- GRACE-type and Bender-type of K_2 for degree above 31;
- GRACE-type of Q_1 for degree 6–29;
- GRACE-type of K_1 for degree above 11;
- Bender-type of N_2 for most degrees;
- Bender-type of O_1 for degree above 31;
- Bender-type of Q_1 for most degrees;
- Bender-type of K_1 above degree 38.

If comparing those exceptions with the spectral distributions of individual coefficient and the degree mean and order mean, one can find: they have more spectral lines except for the primary and secondary frequencies. Another interesting phenomenon is that the de-aliased fields of GRACE-type (GD's) are quite comparable to or even better than the recovered Bender-type (BR's), especially for the semi-diurnal tides. This is a positive sign to reduce the error budget by using GRACE-type formation if the error level of de-aliased fields of GRACE-type is already below the precision of the minimum detectable gravity signals.

To get further understanding of the different performance of the de-aliased fields with respect to different degrees, especially the influence of stripes and aliasing on higher degrees and orders, the recovered fields are now de-aliased separately with respect to primary aliasing frequencies and secondary aliasing frequencies. Apart from that, de-striping (Swenson and Wahr 2006) is applied to the recovered fields and de-aliased fields. Taking the M_2 constituent as an example, Figure 5.3 shows the error degree RMS in geoid

height for

- recovered fields,
- de-aliased fields,
- firstly de-aliased and then de-striped fields,
- de-striped fields, and
- firstly de-striped and then de-aliased fields.

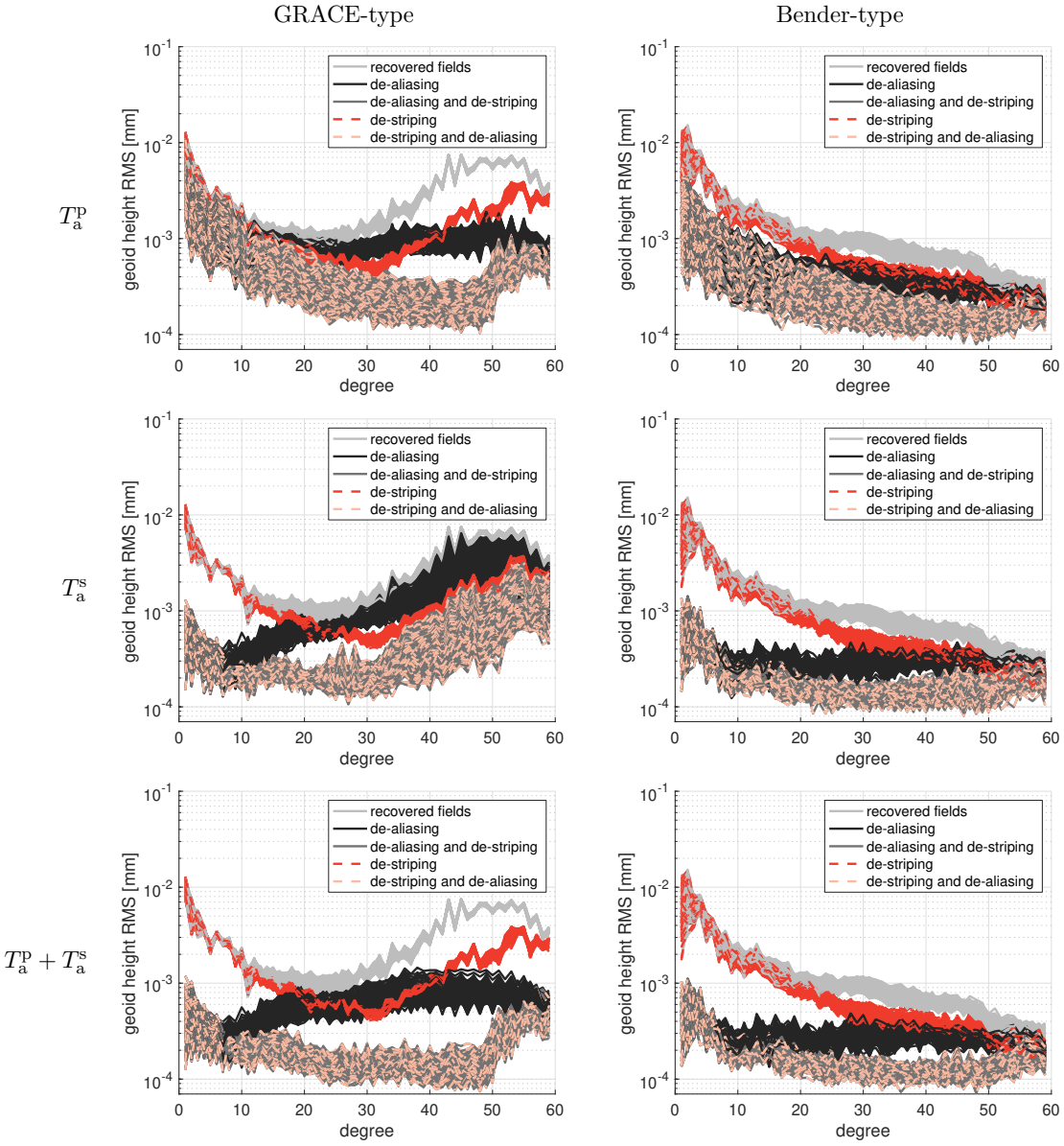

Figure 5.3: Error degree RMS of M_2 of the recovered, the de-striped and the de-aliased fields. De-aliasing is applied with respect to the primary aliasing period T_a^p (top), secondary aliasing period T_a^s (middle), and both T_a^p and T_a^s (bottom).

We can see that the primary aliasing has more influence on the higher degrees while the

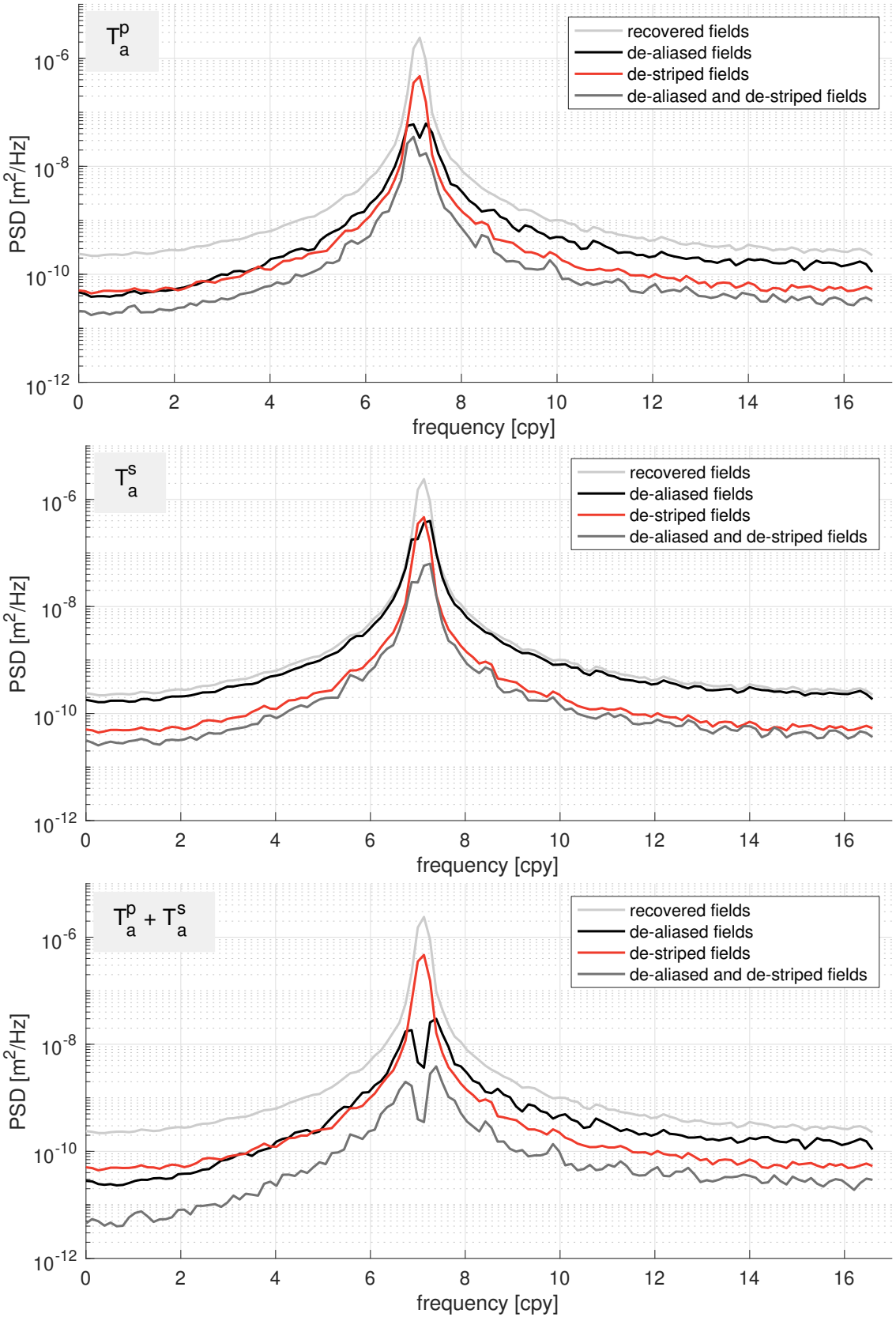

Figure 5.4: Power spectral density of M_2 for GRACE-type formation, and the frequency is in cycle per year (cpy). De-aliasing is conducted with respect to the primary aliasing period (top) or secondary aliasing period (middle) in sequence or together (bottom). De-striped fields (red) and de-aliased and de-striped fields (gray) are also shown.

secondary aliasing has a greater effect on lower degrees. Stripes have more influence on higher degrees than lower degrees for GRACE-type formation, and are reduced largely for Bender-type constellation, as expected. Apart from this, the order of de-aliasing and de-striping does not influence the final estimated fields. That also means that the striping phenomenon does not change the spectral lines of the recovered fields, and the aliasing does not change the correlation relation among degrees.

Figure 5.4 shows error power spectral density of the recovered, de-aliased and de-striped fields for GRACE-type formation of M_2 constituent, which also demonstrates that the de-striping processing reduces the energy over the whole spectra but does not change the shape of the spectrum. De-aliasing with respect to the primary aliasing reduces the energy over the whole spectra. In comparison, de-aliasing with respect to the secondary aliasing only reduces the energy locally around the de-aliased frequency. By combining the de-striping and de-aliasing, the error can be reduced by about two orders of magnitude.

Figure 5.5 shows mean degree rms in geoid height for all the scenarios with the following fields: recovered field (RF), de-aliasing with respect to primary aliasing periods (D1), de-aliasing with respect to secondary aliasing periods (D2), de-aliasing with respect to primary and secondary aliasing periods (D12), de-striping (DS), de-aliasing with respect to primary and secondary aliasing periods and de-striping (D12S). For the scenarios whose primary and secondary aliasing periods are the same, only four fields are included, namely RF, D12, DS and D12S. Figure 5.5 indicates that it is common for all the constituents that the primary aliasing has a more significant influence on higher degrees than lower degrees, while secondary aliasing periods has a more significant influence on lower degrees than higher degrees. This phenomenon is prominent especially for the GRACE-type formation. Apart from that, only primary aliasing periods or only secondary aliasing periods are not enough to model the aliasing errors. The combined primary-secondary de-aliasing is a necessity to better model the aliasing errors. In general, the magnitudes of striping errors are smaller than the magnitudes of aliasing errors, comparing the de-striped fields (DS's) and the de-aliased fields (D12's) with the recovered fields (RF's) individually.

Figure 5.6 shows the de-aliasing with respect to the aliasing periods from the SBASA comparing to the de-aliasing with respect to two-step aliasing derived aliasing frequencies. The frequencies detected by the SBASA which are corresponding to the secondary aliasing frequencies, are called *main frequencies*, with periods indicated by the 6-8th column of Table 4.3 accordingly. The remaining frequencies detected by the SBASA apart from main frequnecies are called *side frequencies*, which are shown in Figure 4.2, 4.7, 4.8, 4.9 and 4.10.

It should be reminded that according to the Nyquist sampling rules, the spectral analysis can only detect the periods above twice of the sampling periods. For instance, the detected

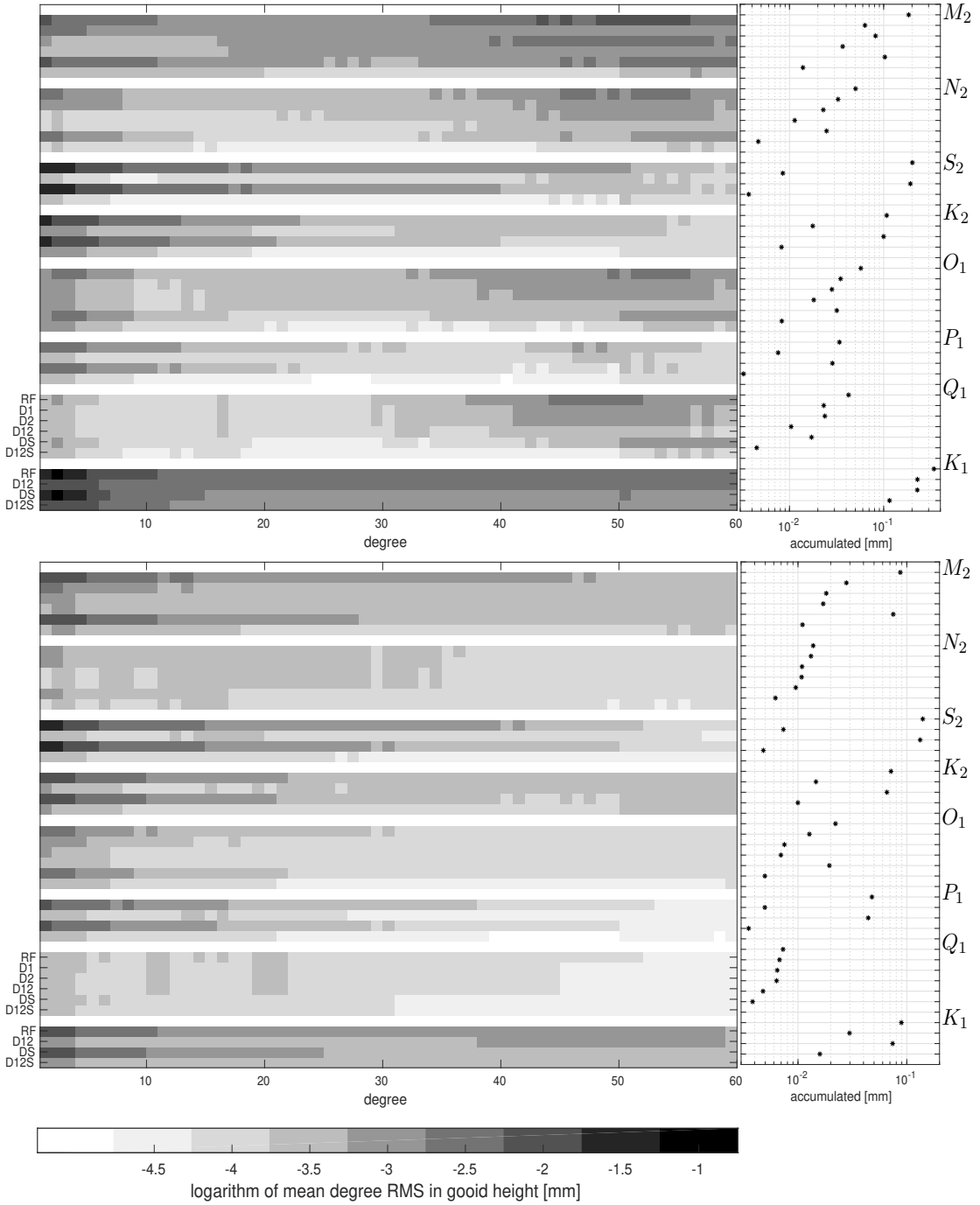

Figure 5.5: Logarithm of mean error degree RMS in geoid height [mm] for 8 major constituent of GRACE-type (top) and Bender-type (bottom). The involved fields are: recovered field (RF), de-aliasing with respect to primary aliasing periods (D1), de-aliasing with respect to secondary aliasing periods (D2), de-aliasing with respect to primary and secondary aliasing periods (D12), de-striping (DS), de-aliasing with respect to primary and secondary aliasing periods and de-striping (D12S). The remaining setting is the same as Figure 5.2.

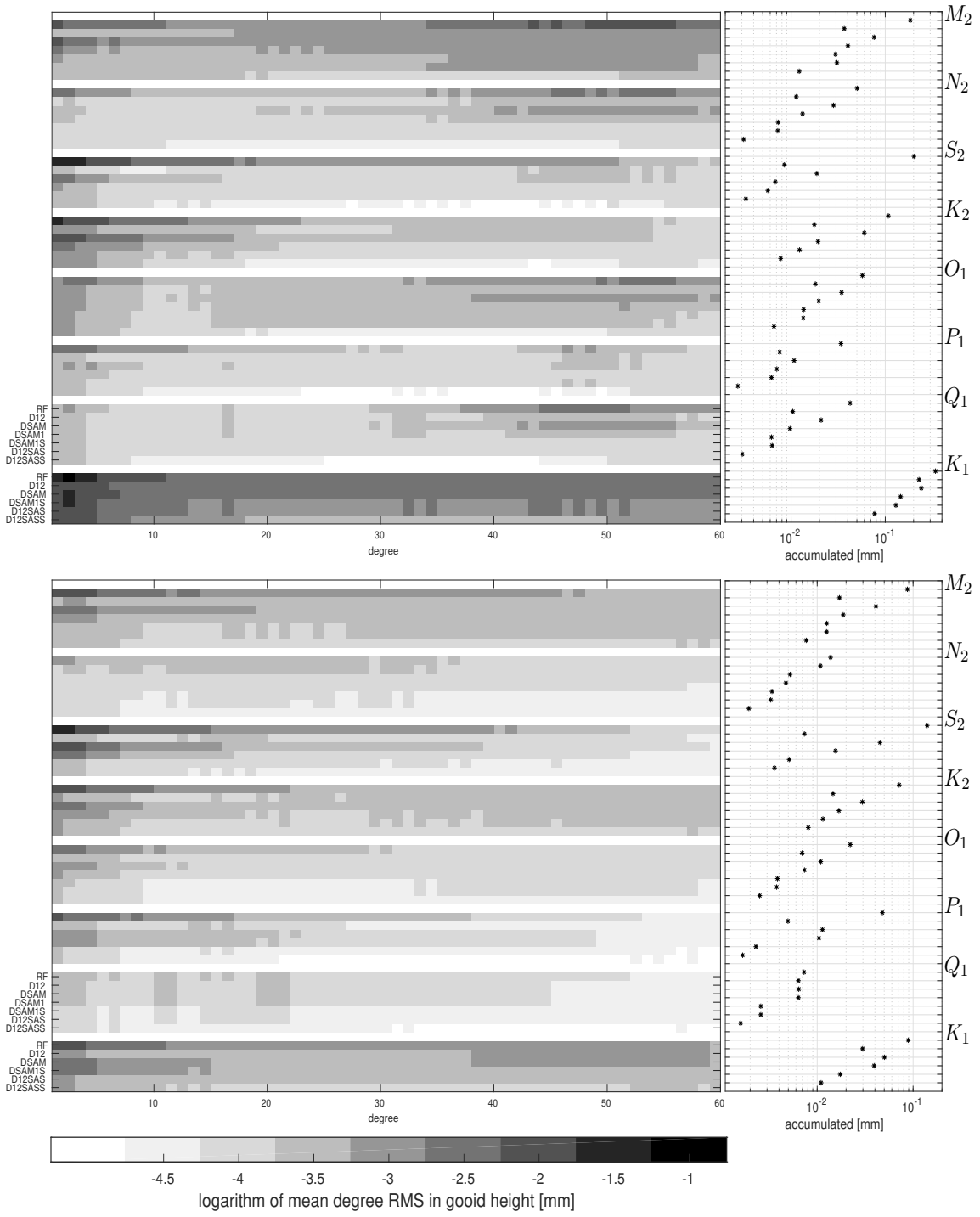

Figure 5.6: Logarithm of mean error degree RMS in geoid height [mm] for 8 major constituent of GRACE-type (top) and Bender-type (bottom). The involved fields are: RF, D12, de-aliasing with respect to the main frequencies of spectral analysis (DSAM), de-aliasing with respect to the main frequencies and primary aliasing frequencies (DSAM1), de-aliasing with respect to the main frequencies, primary aliasing frequencies and side frequencies (DSAM1S), de-aliasing with respect to the primary aliasing frequencies, secondary aliasing frequencies and side frequencies (D12SAS), de-aliasing with respect to the primary aliasing frequencies, secondary aliasing frequencies, side frequencies and de-striping (D12SASS). The remaining setting is the same as Figure 5.2.

periods in the currently discussed simulations are above 22 days as the sampling period is 11 days. In theory, an aliased signal can be fully represented by its aliasing frequency, and no original frequency is needed. Corresponding to the currently discussed simulations, that is, the secondary aliasing frequencies should contain all the information of aliased ocean tides. However, it is obviously not the case for the analysis above: de-aliasing with respect to either secondary aliasing periods (fields D2's in Figure 5.5) or main frequencies derived by SBASA (fields DSAM's in Figure 5.6) cannot fully remove the aliasing errors. *Therefore, the aliased fields contain the harmonics of primary aliasing and secondary aliasing synchronously.* This is due to the following *facts*:

- a certain tidal constituent has different distribution patterns for different locations,
- a certain tidal constituent experiences different orbit sampling patterns within different spatial scales.

The second point above induces different averaging strategies for different spatial scales, corresponding to the spherical degree and order, when recovering the gravity fields from the orbit samples. This also tells why the spectral analysis with respect to spherical harmonic coefficients shows much richer spectral lines than the estimated aliasing frequencies by the two-step aliasing mechanism. To summarize, the presence of primary aliasing periods is reasonable because of the above *facts* and *modelling of the aliasing errors with the primary aliasing periods is a must*.

As shown in Table 4.3, the main frequencies detected by SBASA can be slightly or largely different from the secondary periods according to the Rayleigh criterion, which was discussed in Chapter 4. In general, the de-aliasing with respect to the two-step primary and secondary aliasing periods outperforms (fields D12s in Figure 5.6), either slightly or largely, the de-aliasing with primary aliasing periods and a substitution of secondary aliasing periods by the main frequencies derived by SBASA (fields DSAM1's). A distinct exception is N_2 constituent of Bender-type, where the DSAM1 field outperforms the D12 field significantly. According to the two-step aliasing mechanism, the primary aliasing of the inclined pair is about 11.1 days (see Table 4.3), which is very close to the secondary sampling period, 11 days. Therefore, the estimated secondary aliasing period by equation (3.19) is about 1115.8 days. However, the power spectral density plots given by Figure 4.7 shows very strong energy at period about 22.7 days. This can be explained by the complexity of the real tidal fields as well, similar to the existence of harmonics at the primary aliasing periods. Because of the complexity, the signal with *about* 11.1-day period may be present itself at a *real* period closer to about *twice* or even *triple* of its *original* 11.1-day period. If so, the 11-day sampling is *not* an undersampling and the *real* period can be detected. Therefore, a 22.7-day harmonic shows up rather than a harmonic with long aliasing period of 1115.8 days. Consequently, the de-aliasing with respect to the *real* 22.7 days outperforms de-aliasing with respect to the *fake* aliasing period of 1115.8 days.

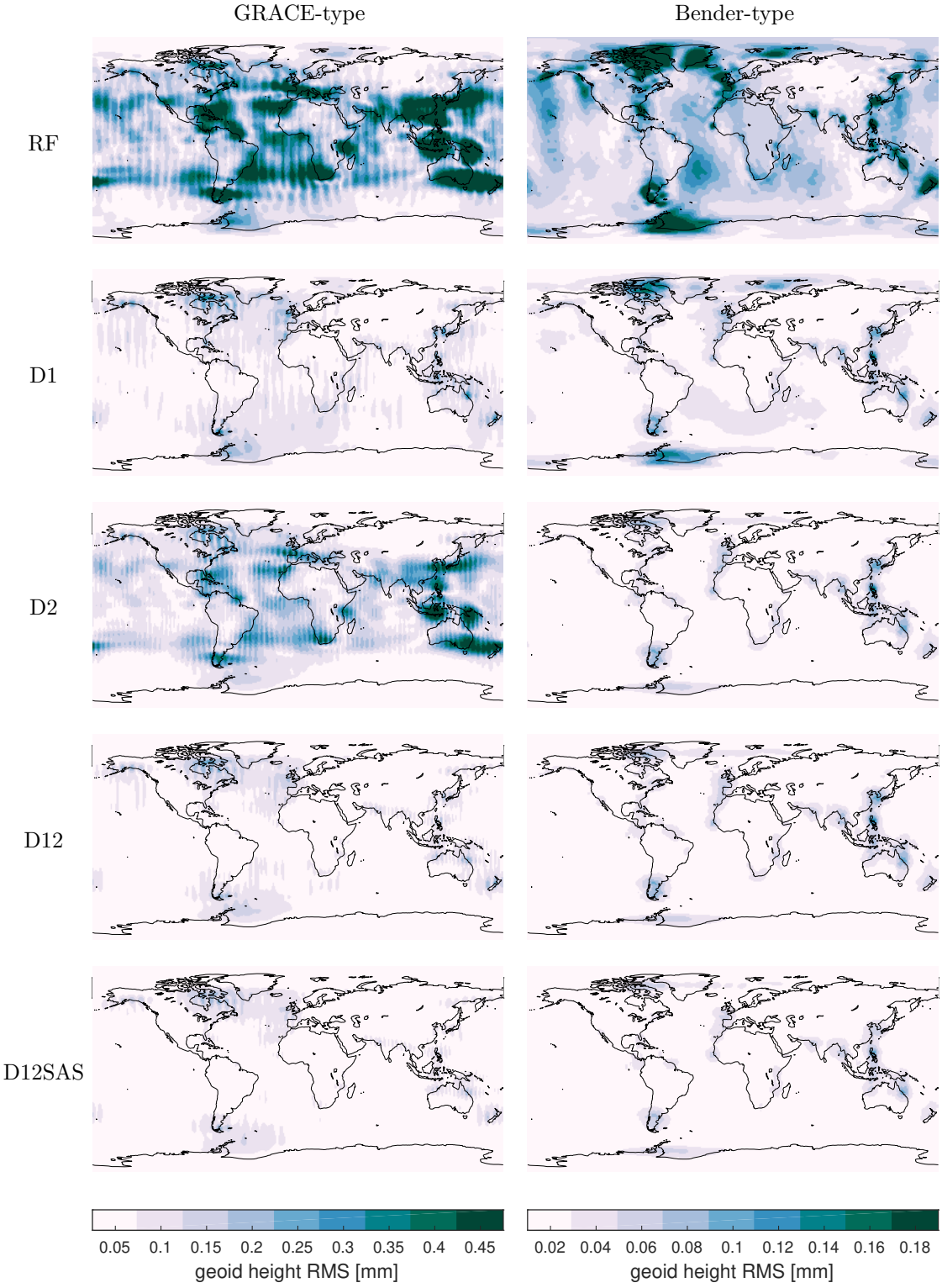

Figure 5.7: Geoid height RMS [mm] of M_2 for five fields: RF, D1, D2, D12 and D12SAS. Each colorbar is valid for its column. Please note the different colorbar ranges for GRACE-type scenarios and Bender-type scenarios.

The side frequencies derived by SBASA are also evaluated by de-aliasing together with the main frequencies and the primary aliasing frequencies (fields DSAM1S's) or the primary and secondary aliasing frequencies (fields D12SAS's). It is further demonstrated when comparing DSAM1S's with D12SAS's, that the main frequencies are not better than the secondary aliasing frequencies in terms of modelling the aliasing errors. Comparing D12SAS's with D12's, one can find that the side harmonics help to remove part of the aliasing errors and improve the de-aliased results further in general, especially for the scenarios with a rich spectrum, e.g. K_1 of Bender-type improved by almost one level of magnitude in terms of accumulated degree RMS. Despite the good performance of de-aliasing processing, the de-striping processing further improves the fields, comparing fields D12SAS's and D12SASS's. This is to say, stripes are still hidden in the fields *with a reduced magnitude* and de-striping is needed when the magnitude of errors is significant in the real data processing.

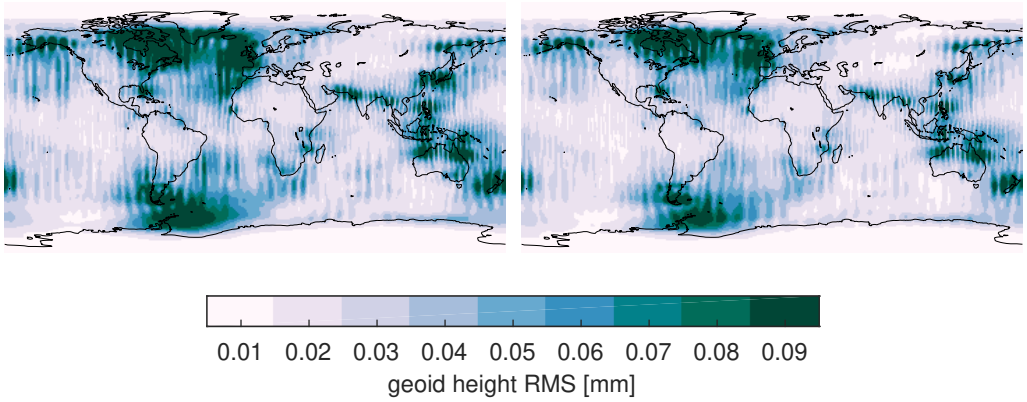

Figure 5.8: Geoid height RMS [mm] of de-aliased fields D12 (left) and D12SAS (right) of GRACE-type M_2 scenario, the same fields as in Figure 5.7 with smaller colorbar range.

In the previous discussion, the de-aliasing performance of different aliasing periods are investigated by comparing the mean degree RMS. What has not been shown is the spatial pattern of the related fields and the spectral pattern of each spherical harmonic coefficient. Based on the discussion and corresponding conclusions above, the following fields are of highest interest to show the fine spatial and spectral patterns: RF, D1, D2, D12, D12SAS. Taking M_2 as an example, Figure 5.7 shows the spatial pattern of each field for GRACE-type and Bender-type scenarios in terms of geoid height RMS. For both types of scenarios, the de-aliased fields D12's have a significant improvement globally comparing to the recovered fields RF's. The recovered field of GRACE-type has larger errors at low and middle latitudes and smaller errors at high latitudes. The recovered fields of Bender-type shows the opposite. This behaviour is expected as the GRACE-type polar pair has denser orbit sampling at high latitude, while the added inclined pair of Bender-type brings more sampling at low latitude within the coverage of the inclined orbits. The typical stripes show up in the recovered fields of GRACE-type scenarios, which are not so obviously

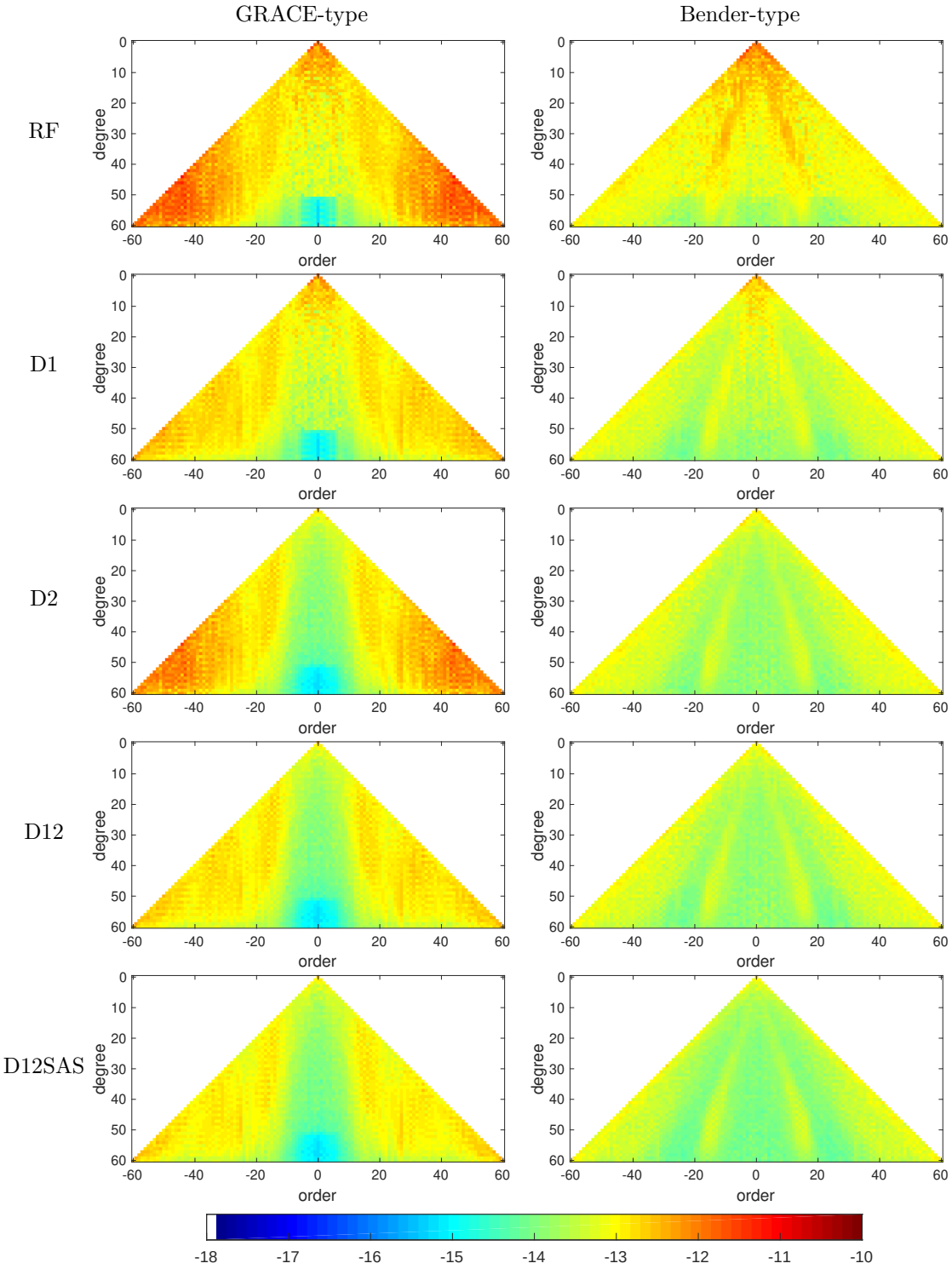

Figure 5.9: RMS of individual spherical harmonic coefficients of M_2 for five fields: RF, D1, D2, D12 and D12SAS.

observed in the recovered fields of Bender-type scenarios. As discussed before, the de-aliased fields are still influenced by the striping errors, with a lower magnitude though. This can be observed when changing the colorbar into a proper range. For instance, Figure 5.8 shows the stripe pattern of de-aliased fields, D12 and D12SAS, of GRACE-type scenario by reducing the maximum colorbar magnitude to 0.09 mm. The other constituents show a similar behaviour when comparing the recovered fields with the de-aliased fields, and Bender-type scenarios with GRACE-type scenarios, see Appendix A.

Figure 5.9 gives the RMS of each spherical harmonic coefficient of M_2 scenarios for different fields. Comparing D1 and D2 with RF one can find that the secondary aliasing affects the zonal and low order tesseral coefficients mostly, while the primary aliasing has more influence on the remaining coefficients. To understand this behaviour, the meaning of the two-step aliasing mechanism should be reminded:

- primary aliasing is based on the orbit sampling at the latitude circles, with the *longitudinal uniform assumption* of the ocean tides;
- secondary aliasing is caused by *the undersampling of the primary aliasing signals*;

To emphasize, *a similar* spatial averaging should be followed for a certain region among different recovered solutions to guarantee a consistent behaviour of secondary aliasing. Naturally, the secondary sampling is better fitted in a large region than in a small region. This was discussed in detail in section 4.6. Now if we consider the real ocean tides within different scales corresponding to the spherical harmonics, the secondary aliasing within a latitude band (corresponding to zonal harmonics) and large scale tesseral area (low order tesseral harmonics) is easier and better fulfilled than a longitudinal band (sectorial harmonics) and a small tesseral area (high order tesseral harmonics), regardless of the influence of the ecliptical obliquity (see the discussion in section 3.5). It is also understandable that the de-aliasing with respect to the primary and secondary aliasing frequencies can not remove all the errors:

- the assumption of longitudinal uniform ocean tides only holds to a limited extent,
- the temporal and spatial averaging are not strictly consistent for regions at all scales.

Therefore, the side frequencies derived by the spectral analysis aid the de-aliasing to some extent (see the further discussion below), c.f. D12SAS's. The RMS of spherical harmonic coefficients of the remaining constituents is given in Appendix A.

Figure 5.10 shows the overall mean geoid height RMS for all 8 major tides with GRACE-type and Bender-type simulations. On two sides of the bars are the relative improvements (Ip in %), in terms of mean geoid height RMS of each de-aliasing case relative to individual recovery field, namely

$$Ip(F) = \frac{RF - F}{RF}, \tag{5.3}$$

in which F can be D1, D2, D12 or D12SAS. From Figure 5.10 we can see that *in general*

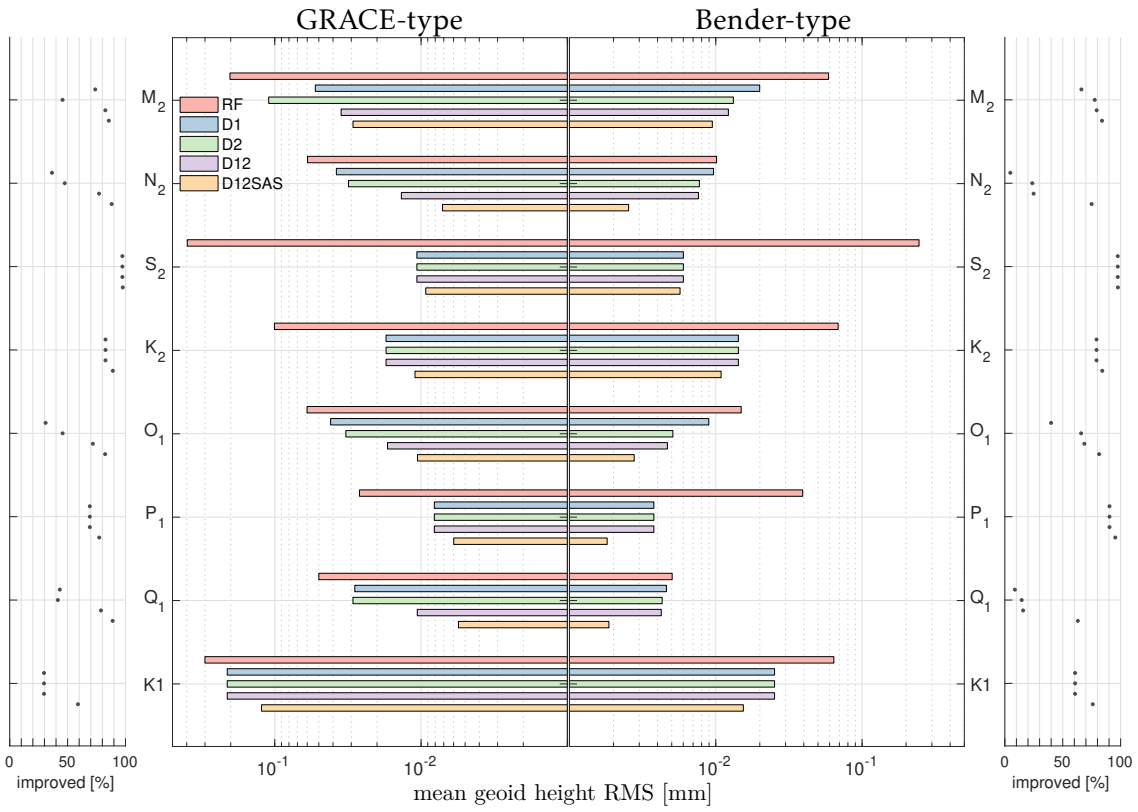

Figure 5.10: Mean geoid height RMS [mm] for 8 major tides of five fields: RF, D1, D2, D12 and D12SAS. The left half shows the simulations from GRACE-type formation. The right half shows the simulations from Bender-type constellation. The scatter plots shows the improvement of each de-aliasing strategy regarding the recovery field.

the Bender-type constellation outperforms GRACE-type formation if we compare all five fields accordingly. The statistics of improvement from a GRACE-type to a Bender-type are not given as they vary a lot due to the different orbit design. There are several exceptions:

- the Bender-type is slightly worse than the GRACE-type for the recovery field of P_1, though the de-aliased fields are reduced largely for Bender-type, also see Figure A.8;
- the Bender-type is slightly better than the GRACE-type for the recovery field of K_2, and the de-aliased fields of both scenarios are very close, Figure A.5.

That is to say, not all constituents benefit from adding a second-pair. Although adding an extra pair means having more samples, those samples do not always bring improvement to the final estimated fields. Furthermore, the well de-aliased fields of GRACE-type scenarios can be better than the recovery fields of Bender-type, for instance comparing the D12 or even D12SAS of GRACE-type to the RF of Bender-type for M_2 constituent. Therefore, with careful treatment of the aliasing errors, the improvement of the GRACE-type formation can be very promising.

Another point to emphasize is that the contribution of primary aliasing and secondary aliasing are equally important. One should always consider them together for optimal de-aliasing. The improvement of de-aliasing with both primary and secondary aliasing frequencies can be more than one order of magnitude for some constituent, e.g. S_2.

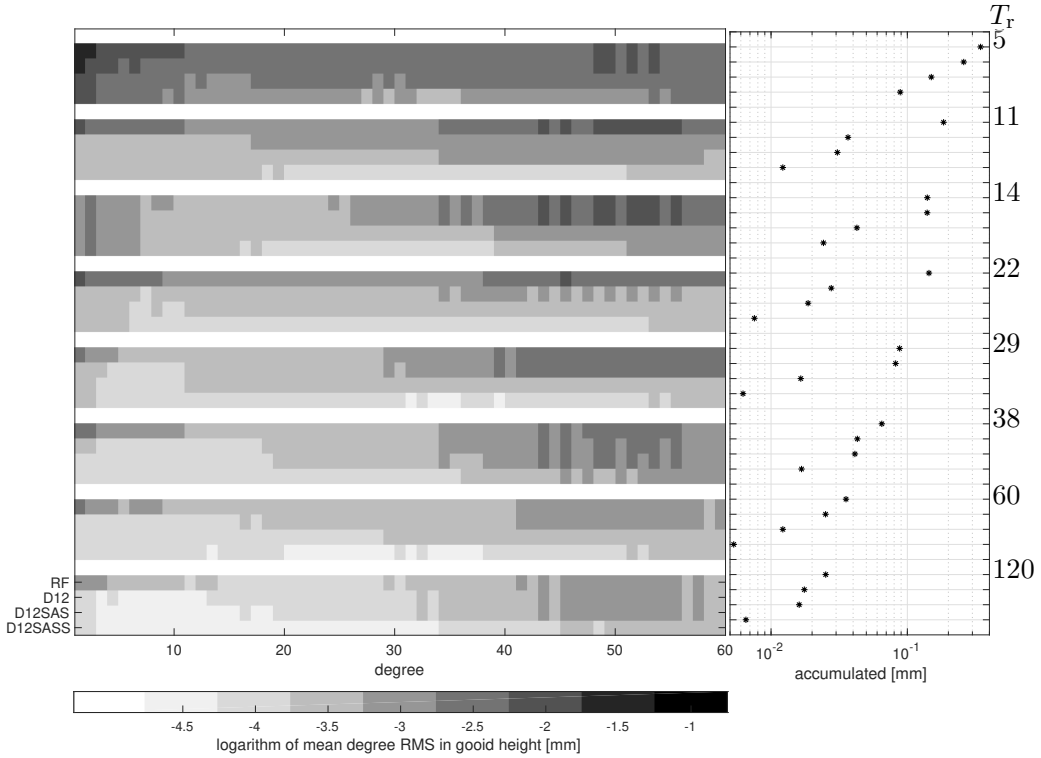

Figure 5.11: logarthim of mean error degree RMS in geoid height [mm] of M_2 for different recovery periods. The involved fields are: recovered field (RF), de-aliasing with respect to primary aliasing periods (D1), de-aliasing with respect to primary and secondary aliasing periods (D12), de-aliasing with respect to primary, secondary and spectral analysis derived aliasing periods (D12SAS), and de-aliasing with respect to primary, secondary and spectral analysis derived aliasing periods and de-striping (D12SASS). The recovery periods are labelled at the right side of the figure. The remaining setting is the same as Figure 5.2.

By adding the side frequencies estimated by SBASA for de-aliasing, i.e. comparing the fields D12SAS to D12, the improvement is about 10% in general. For the most troublesome constituent K_1, the improvement is about 30–60% for GRACE-type and 60–75% for Bender-type. However, the overall error magnitudes are still very high compared to the other constituents.

From section 4.6 we know that the orbit sampling and recovery periods together affect the behaviour of aliasing spectrum. Figure 5.11 shows the recovered and de-aliased fields for the scenarios given in Table 4.4. The pattern of scenario $T_r = 5$ proves that the sampling pattern is very important. Although all the side spectral lines derived from SBASA (see

Figure 4.14) are estimated together with the primary and secondary aliasing frequencies, the de-aliased fields still shows large errors in the whole spectrum.

It should be reminded that the primary aliasing period of the simulated scenarios is about 14.0 days. The pattern of scenario $T_r = 14$ confirmed that, if recovery period is close to the primary aliasing period, the de-aliasing with primary and secondary aliasing periods cannot guarantee a good reduction of errors in the de-aliased fields. The spectral analysis is needed to get the real spectral lines.

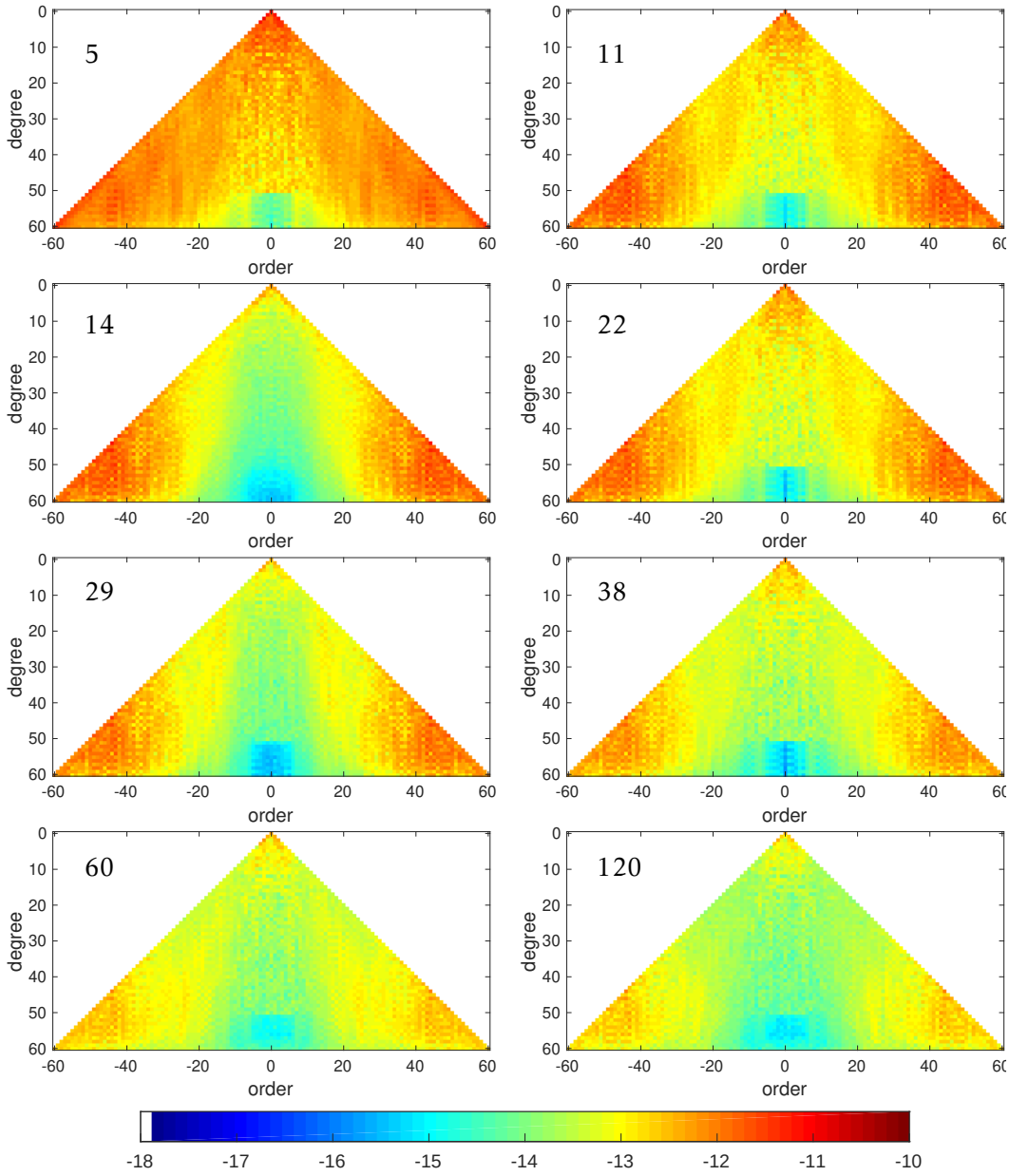

Figure 5.12: RMS of spherical harmonic coefficients of recovered fields. The numbers at the north west are the recovery periods.

Long recovery periods will *average out both the tidal signals and the errors*, especially for the lower degrees, comparing all the different recovery periods. In other words, the estimation of tides will get relative small magnitudes within a large recovery period.

Figure 5.12 indicates that when the recovery periods equal the primary aliasing periods, the zonal coefficients and low order teressal coefficients are reduced significantly due to the averaging effect. This averaging effect can also be achieved when the recovery periods are very large, e.g. scenario T_r = 120 days, or the recovery periods are relative large but close to integer times of primary aliasing periods, e.g. scenario T_r = 29 whose zonal and low tesseral coefficients in general are smaller than the corresponding coefficients of scenario T_r = 38 and T_r = 60. This happens because the large scale regions and latitudinal bands can easily cover the sampling homogeneously and averaging the periodic signals into a significant reduction. For the small regions, only when the recovery period is large enough, can this averaging effect reach a high efficiency, comparing the high degree and order coefficients for different recovery period scenarios.

5.3 Discussion and Summary

In this Chapter, aliasing error mitigation in post-processing is investigated in detail. Firstly, the aliasing error mitigation methods in the spatial domain and in the spherical harmonic domain are introduced. Then, the de-aliasing results are analysed from different views. The following conclusions can be drawn from the discussion in the previous sections:

- De-aliasing in the spatial domain and in the spherical harmonic domain are equivalent when applying the same aliasing periods. However, they do have some difference in the real data processing. On the one hand, the spatial-based de-aliasing needs extra spherical harmonic synthesis and analysis than K_{lm}-based de-aliasing. On the other hand, the spatial-based de-aliasing may have the advantage of reducing the influence on the continental signals which have periods that are close to aliasing periods of tidal constituents, by de-aliasing locally;
- Aliasing does not change the correlation of the degrees for a given order, which induces stripes, and the striping does not change the aliasing spectral lines. However, the magnitudes of the striping errors are reduced after de-aliasing, and vice versa. Some coefficients at high degree and order still have large magnitude after de-aliasing due to the striping effects;
- The primary aliasing affects the whole spherical harmonic spectrum in general, and the secondary aliasing affect the zonal and low order tesseral coefficients significantly. Both primary and secondary aliasing are needed to be considered for de-aliasing;
- The aliasing spectral lines change to different extent when the sampling patterns

within a recovery period vary from one recovery interval to another interval. Spectral analysis needs to be applied to find the side aliasing frequencies apart from the primary and secondary aliasing frequencies. In addition, larger recovery periods also reduce the ocean tide error magnitudes more significantly due to (1) the periodic characteristics of ocean tides, (2) the longitudinal uniform distribution of ocean tides to some extent, and (3) the temporal and spatial averaging of the spherical harmonic analysis;

- The spectral analysis has limitations: (1) some side frequencies cannot be detected when the recovery period is large according to the Nyquist sampling rules, and (2) some frequencies are not precisely estimated according to the Rayleigh criteria;
- In general, the Bender-type scenarios have smaller magnitudes of ocean tide aliasing errors than the GRACE-type scenarios. However, for a few constituents, adding the second inclined pair does not always reduce the magnitudes of original aliased fields or even the de-aliased fields. The same de-aliasing processing for single pair can be applied to the aliasing fields due to two-pair sampling, with the aliasing frequencies derived for the individual pairs.

Chapter 6

Orbit design considering ocean tide aliasing

This work till now has clarified the ocean tide aliasing mechanism in satellite gravimetry and discussed the reduction of the ocean tide aliasing errors in post-processing. A further question can be posed: *how can future satellite missions benefit from this newly gained knowledge?* In this chapter, future mission orbit design considering the ocean tide aliasing will be discussed based on what has been learned in the previous chapters. One needs to define the aims of a future mission before starting the orbit design. Regarding ocean tides, the aim can be either aliasing error mitigation or signal extraction. Different criteria need to be met for different aims, which may have some aspects in common, but mostly not. It should be reminded that it is impossible to remove the aliasing errors and to improve the ocean tide models at the same time.

For the aliasing error mitigation, the best situation is removing the ocean tide errors by orbit design, combining different orbit samplings in a way that the errors cancel each other. In reality, the errors cannot be removed for all the constituents or for one constituent at all locations. Therefore, to compensate, post-processing is needed to reduce the errors. For that purpose, the aliasing periods should be as small as possible in order to remove the aliasing errors as soon as possible. It was also shown that the recovery period should avoid being too *close to* the primary aliasing period, e.g. less than one day difference between them, to cause the unpredictable secondary aliasing frequencies or very low secondary aliasing frequencies which cannot be removed easily in post-processing.

This Chapter focuses on aliasing error mitigation for future mission design. The ocean tide signal extraction will be discussed as a trigger for future investigation in next chapter. Specifically, section 6.1 discusses the relation between phase sampling of the ocean tides

and the nodal difference of two or more orbits. Section 6.2 presents possible ways to achieve a good groundtrack pattern. Section 6.3 shows the relations between aliasing periods and the orbit altitude and inclination. Based on the discussion in the first three sections, section 6.4 simulates several scenarios and analyse the results. In the end, section 6.5 summarizes this chapter.

6.1 Phase sampling of ocean tides

As discussed in section 3.3, the sampling of an individual tidal constituent along the orbit shows a periodic pattern in the u-t cyclogram. This characteristic can be used to design orbits for mitigating ocean tide aliasing errors. Ideally, if the ocean tides are sampled *out-of-phase*, the samples will cancel each other when combined to recover the fields. As a result, ideally aliasing errors would not exist in the final gravity field products. As already discussed, the periodic patterns correspond to the primary aliasing periods, which depend on the orbital nodal rate. For a circular nominal orbit, the nodal rate is defined only by the altitude and inclination.

In order to have the minimal ocean tide aliasing errors, the out-of-phase sampling should be kept for the whole mission duration. This can only be achieved when the orbit precession of the satellites are the same. The easiest scenario is two pairs of satellites with the same altitudes and inclinations, but different in argument of latitudes, Δu, or right ascensions of ascending nodes, $\Delta\Omega$. In theory, the out-of-phase sampling can be achieved by either designing Δu or $\Delta\Omega$, or even combining both of them, under the condition of nominal orbits and two pair satellites. However, when the scenario becomes more complex, real orbit or more pairs, Δu is not so straightforward when ocean tide sampling is considered. Therefore, $\Delta\Omega$ is considered as the only variable for phase sampling design from now on, by default setting $\Delta u = 0$.

In terms of a double-pair mission, out-of-phase means the phase difference $\Delta\phi$, sampled by two satellite orbits, is 180°. The corresponding $\Delta\Omega$ can be calculated as

$$\Delta\Omega = \frac{\Delta\phi}{\phi_{1d}}, \tag{6.1}$$

in which ϕ_{1d} can be calculated by equation (3.9) for a given constituent. The resulting $\Delta\Omega$ for all 8 major constituents are shown in Table 6.1.

Table 6.1: Nodal difference of the double-pair formation.

constituent	M_2	N_2	S_2	K_2	O_1	P_1	Q_1	K_1
$\Delta\Omega$ [deg]	93.4	95.2	90.2	90.0	194.2	181.0	202.1	180.0

Figure 6.1 shows the pattern of the observations along the orbits for S_2 and K_1. Tides S_2 and K_1 are sampled individually by two orbits with the same orbit parameters except for

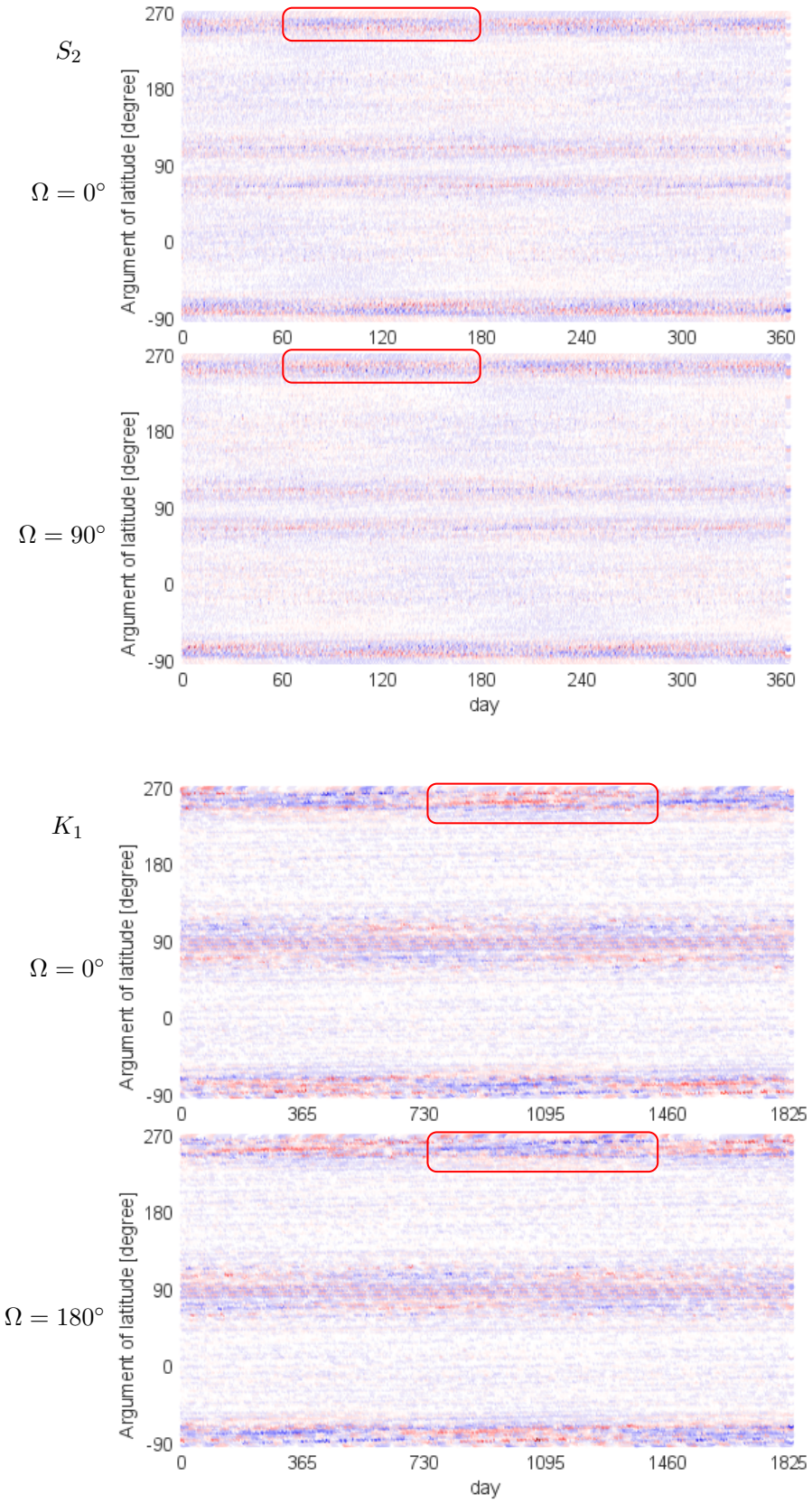

Figure 6.1: Phase sampling of the constituent S_2 and K_1.

ascending nodes difference, $\Delta\Omega = 90°$ and $\Delta\Omega = 180°$ respectively, at the initial epoch. The out-of-phase patterns are clearly seen comparing the two orbit sampling for each constituent. For instance, the red boxes of S_2 shows three layers, from top to bottom, of red-blue-red pattern for scenario $\Omega = 0°$ and blue-red-blue pattern for scenario $\Omega = 90°$. Similar out-of-phase patterns can be seen for the K_1 constituent, e.g. red-blue pattern for scenario $\Omega = 0°$ and blue-red for scenario $\Omega = 180°$ in the red boxes from top to bottom.

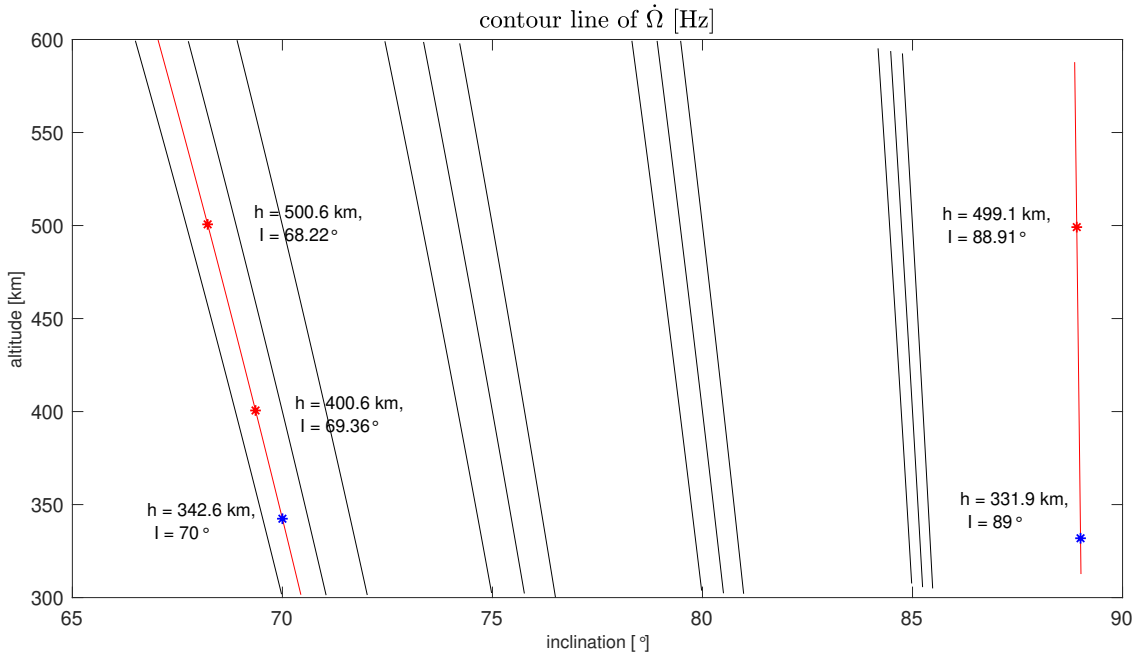

Figure 6.2: Contour line of nodal rate $\dot{\Omega}$ regarding altitude and inclination.

Apart from setting the same altitudes and the inclinations for two-pair satellites, the altitudes and inclinations can be changed in a certain way to keep the same nodal rate. Figure 6.2 shows the contour line of nodal rate $\dot{\Omega}$ regarding altitude and inclination. The following information is indicated by Figure 6.2:

- the same $\dot{\Omega}$ can be achieved by changing the inclination slightly while considerably changing the altitude;
- for the same inclination variation, the altitude change should be larger for (near-) polar orbits than for inclined orbits.

This characteristic can be interpreted further that for two satellites with large difference in altitude, the same orbit precession can be kept by tuning the inclination within a small range. This can be used to combine a newly designed satellite mission with a mission already in service to form a new constellation which was not planned for the mission already in orbit.

Table 6.1 shows that different constituents have different optimal $\Delta\Omega$'s. Therefore, a compromise must be made for a given satellite mission as not every constituent can be

served. Different criteria can be followed to achieve a compromise, e.g.

- minimizing the aliasing errors of the constituent with largest magnitude, namely M_2;
- minimizing the aliasing errors of the constituent which is supposed to have largest errors in ocean tide modelling;
- minimizing the aliasing errors of the constituent whose aliasing periods are close to the periods of important temporal signals;
- minimizing the overall aliasing errors.

Different criteria will lead to different self-dealiasing performances of the mission. The remaining aliasing errors, if they are still significant enough compared to other error sources or the signals, can be removed in post-processing.

Furthermore, three pairs with the same $\dot{\Omega}$ are considered. For a single constituent, the periodic pattern can be modelled by a sinusoid harmonic. For a triple-pair sampling, the object function to minimize the aliasing errors for an arbitrary constituent is

$$\sin\left(f_{\mathrm{a}}^{\mathrm{p}} t + \phi_1\right) = -\left(\sin\left(f_{\mathrm{a}}^{\mathrm{p}} t + \phi_2\right) + \sin\left(f_{\mathrm{a}}^{\mathrm{p}} t + \phi_3\right)\right), \tag{6.2}$$

in which $f_{\mathrm{a}}^{\mathrm{p}}$ is the primary aliasing period of the specific constituent, and ϕ_1, ϕ_2 and ϕ_3 are the phases of the three orbits at the initial epoch. Applying the sum-to-product formula to the right side of (6.2) gives

$$\sin\left(f_{\mathrm{a}}^{\mathrm{p}} t + \phi_1\right) = -2\sin\left(f_{\mathrm{a}}^{\mathrm{p}} t + \frac{\phi_2 + \phi_3}{2}\right)\cos\left(\frac{\phi_2 - \phi_3}{2}\right). \tag{6.3}$$

Rewriting equation (6.3) one gets

$$2\cos\left(\frac{\phi_2 - \phi_3}{2}\right) = -\frac{\sin\left(f_{\mathrm{a}}^{\mathrm{p}} t + \phi_1\right)}{\sin\left(f_{\mathrm{a}}^{\mathrm{p}} t + \frac{\phi_2+\phi_3}{2}\right)}. \tag{6.4}$$

For an arbitrary epoch t, the numerator and denominator at right side of the equation (6.4) can vary from -1 to $+1$, but the left side of the equation, $2\cos\left(\frac{\phi_2-\phi_3}{2}\right)$, is a constant. Therefore, only when

$$2\cos\left(\frac{\phi_2 - \phi_3}{2}\right) = \pm 1, \tag{6.5}$$

equation (6.4) is independent of time variation. Therefore,

$$\frac{\sin\left(f_{\mathrm{a}}^{\mathrm{p}} t + \phi_1\right)}{\sin\left(f_{\mathrm{a}}^{\mathrm{p}} t + \frac{\phi_2+\phi_3}{2}\right)} = \mp 1, \tag{6.6}$$

holds accordingly. Solving equation (6.5) and (6.6) together by setting one initial value, e.g. $\phi_1 = 0°$, gives one set of possible initial phases

$$\begin{aligned} \phi_1 &= 0° \\ \phi_2 &= 120° \\ \phi_3 &= 240°. \end{aligned} \tag{6.7}$$

Table 6.2: Right ascension of ascending nodes for triple-pair constellation, with $\Omega_1 = 0°$.

constituent	M_2	N_2	S_2	K_2	O_1	P_1	Q_1	K_1
Ω_2 [deg]	62.3	63.5	60.2	60.0	129.5	120.7	134.7	120.0
Ω_3 [deg]	124.5	126.9	120.3	120.0	258.9	241.3	269.4	240.0

Applying the equation (6.1) by replacing $\Delta\phi$ by ϕ_1, ϕ_2 and ϕ_3 accordingly gives the corresponding right ascension of ascending nodes for individual constituent, as listed in Table 6.2 with $\Omega_1 = 0°$.

For a Bender-type constellation, containing a polar pair and a inclined pair, the nodal rates $\dot{\Omega}$ of two orbits are different. Therefore, the constant out-of-phase sampling can not be kept for the whole lifetime of the mission. Strictly speaking, the discussion above is not fully applicable. However, the numerical simulation and analysis will show that a similar idea discussed in this section also helps in the orbit design of a constellation with orbits of different $\dot{\Omega}$, e.g. Bender-type.

6.2 Groundtrack patterns

Based on the discussion in section 4.6 and 5.2, the groundtack pattern within a recovery period, *homogeneity*, and among different recovery periods, *consistency*, is very important for forming the aliasing frequencies and then affecting the de-aliasing performance. Therefore, a (relative) homogeneous and consistent groundtrack pattern is proposed for a future mission to mitigate the aliasing errors both with the self-dealiasing orbits and in post-processing. The easy way to fulfil these requirements is a repeat orbit. A repeat orbit means the satellite performs β revolutions and evenly samples the Earth for each given latitude in α nodal days, which is also called a repeat cycle. After that, the ground tracks start repeating themselves, which is the beginning of the next repeat cycle. A repeat orbit gives homogeneous and consistent ground track pattern. However, a repeat orbit is not the first choice for satellite gravimetry which aims at modelling the temporal gravity fields as well as the static gravity fields, as a high spatial resolution and a high temporal resolution can not be fulfilled at the same time for a repeat orbit. As we know, the spatial resolution R_s and temporal resolution R_t of a repeat orbit fulfils

$$R_s \times R_t = C, \tag{6.8}$$

which means temporal resolution and spatial resolution are inversely proportional for a given repeat orbit.

To keep a relative high temporal resolution, meanwhile improve the spatial resolution in a long run, Christian Siemes (personal communication) has proposed a type of drift orbit with a constant λ-shift $\Delta\lambda$, e.g. 1.3° within a certain time interval, called *drift cycle* T_{dc}.

The *drift* is defined as

$$D = \frac{\Delta\lambda}{T_{\mathrm{dc}}}, \tag{6.9}$$

with the unit degree/cycle, e.g. 1.3°/cycle. For this type of drift orbit, a similar groundtrack pattern among different drift cycles, the consistency, can be guaranteed as the groundtracks within a drift cycle are shifted as a whole to one direction after a drift cycle, by definition. The homogeneity, H, of the groundtracks, can be evaluated by the ratio of maximum and minimum gaps, $\Delta\lambda_{\mathrm{max}}$ and $\Delta\lambda_{\mathrm{min}}$, between neighbouring groundtracks at the equator, namely

$$H = \frac{\Delta\lambda_{\mathrm{max}}}{\Delta\lambda_{\mathrm{min}}}. \tag{6.10}$$

When $H = 1$, the orbit is a repeat orbit. The closer H is to 1, the more homogeneous the groundtracks are. Figure 6.3 shows an example of the groundtrack homogeneity for orbits of inclination $I = 70°$ and $I = 89°$, changing with the altitude and period.

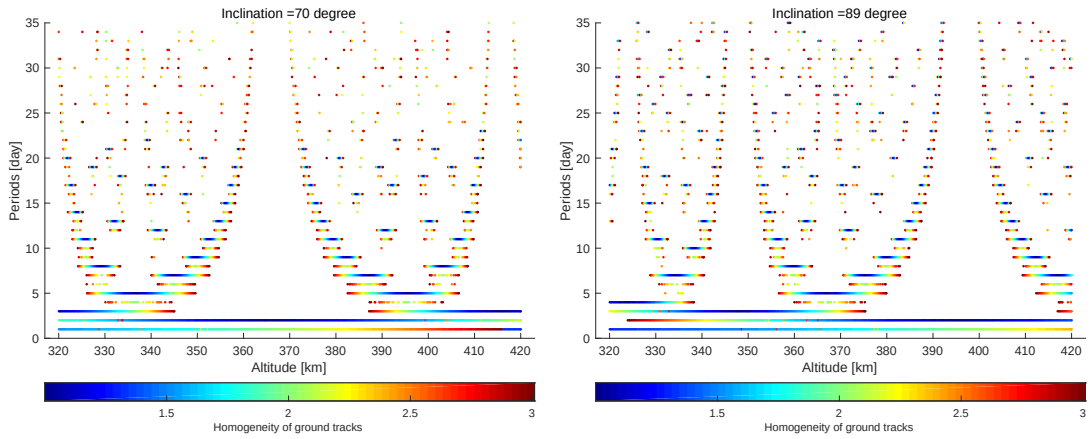

Figure 6.3: The homogeneity of the orbits with inclination of 70° and 89°.

For a mission containing more than one pair of satellites, the *interleaving* should be considered between different orbits. In other words, one needs to put one pair of satellites in between the groundtracks of the other pair(s) to avoid the overlap of the groundtracks from different orbits. This consideration can guarantee a better spatial resolution. Actually, interleaving is the key to improve the spatial resolution in a given time span by double- or multi-pair satellite missions. If this condition is not imposed, the expected improvement of spatial resolution by adding extra pairs cannot be guaranteed.

6.3 Aliasing periods, altitude and inclination

In order to remove the aliasing errors in the post-processing in a short time, the aliasing periods should be small. As already discussed, the primary aliasing period depends on the nodal precession, which is decided by the orbit altitude and inclination. The

secondary aliasing periods depend on the primary aliasing periods and the recovery periods. In this section the distribution of the primary aliasing periods and secondary aliasing periods are investigated with respect to orbit altitude, inclination and recovery period.

Figure 6.4 shows the variation of primary aliasing periods with respect to the altitude and inclination change for 8 major constituents. Figure 6.4 indicates that the altitude variation affect the primary aliasing periods marginally and the influence of inclination variation on primary aliasing periods are relatively significant, especially for the constituent S_2, K_2, P_1 and K_1. In general, polar orbits induce larger primary aliasing periods than the inclined orbits. Comparing the two constituents of each column except for the last one, they tend to have close aliasing periods for an orbit with given altitude and inclination, e.g. M_2 and O_1. In a wide sense, four constituents, M_2, N_2, O_1 and Q_1, have very close aliasing periods. This is irrelevant for the aliasing periods removal as the errors are removed anyway despite the correlation among the estimated coefficients of different constituents, namely $A^n_{c,lm}$, $B^n_{c,lm}$, $A^n_{c,lm}$ and $B^n_{c,lm}$ in equation 5.1. However, a relative long dataset is needed to separate those constituents when one wants to extract the tidal signals. For polar and near polar orbits, primary aliasing periods of S_2 and P_1 are close to the semi-annual period, which may affect the estimation of the semi-annual geophysical signals. When the inclination is above $\sim 84°$ (K_1) or $\sim 87°$ (K_2), the primary aliasing periods of K_1 and K_2 are more than 1 year which means more than 1 year of data is needed to remove the corresponding aliasing errors. Special attention should be paid to the boundary case in which the primary aliasing periods of K_2 and K_1 are about one year when $I \simeq 87°$ or $I \simeq 84°$, respectively, which will mix into the annual geophysical signals.

As the altitude affects the primary aliasing periods marginally, an arbitrary altitude, 300 km, is taken as an example to show the pattern of secondary aliasing periods with respect to the variation of the inclination and recovery period, see Figure 6.5. In general, the secondary aliasing periods of M_2, N_2, O_1 and Q_1 are less than one year, except for the cases when the recovery periods are very close to the integer multiple of the primary aliasing periods, see the bright stripes. Those are the worst cases which should be avoided, when designing the orbit and deciding the recovery period. This is because the errors either alias into very low frequencies, and thus needing long time series to remove them, or the spectral analysis should be conducted to check the possible aliasing frequencies, as discussed in section 4.6 and 5.2. For S_2, the problem of semi-annual aliasing emerges when the orbit is near polar for the whole range of investigated recovery periods, as well as when the orbit is about 65–75° and the recovery period is about 27–35 days, see the top and the bottom right corner of the S_2 plot. The secondary aliasing periods of K_2, P_1 and K_1 are the same as their primary aliasing periods for the investigated cases, because the recovery periods are always smaller than the primary aliasing periods.

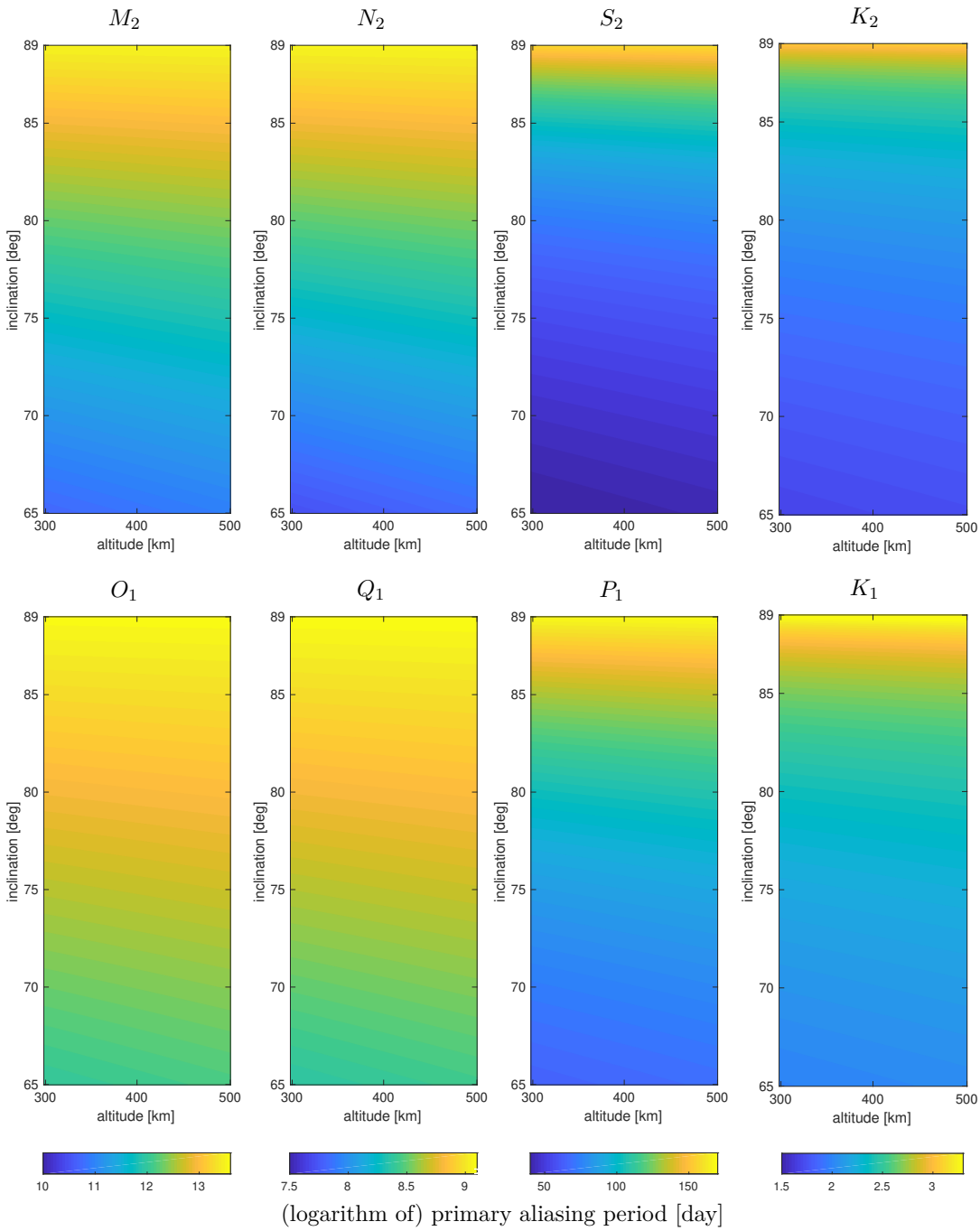

Figure 6.4: Primary aliasing periods variation with respect to the altitudes and inclinations for 8 major tides. Please note the difference of colorbar ranges. For K_1 and K_2, the colorbars stand for the logarithm of the primary aliasing periods, and the rest stands for the primary aliasing periods themselves.

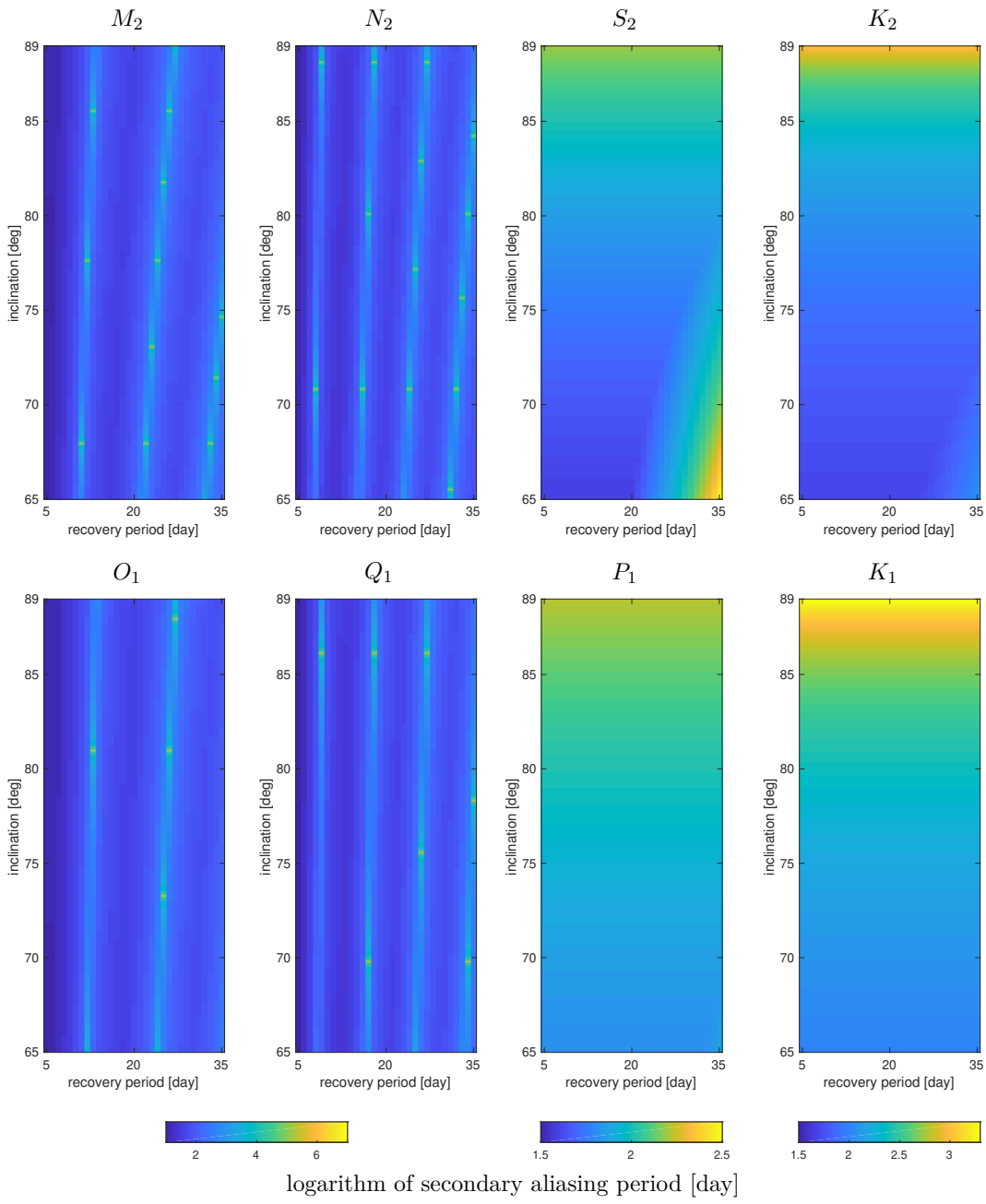

Figure 6.5: Logarithm of secondary aliasing periods variation with respect to the inclinations and recovery periods for 8 major tides.

Table 6.3: Basic information of simulated orbits.

basic orbit	altitude	inclination	drift cycle	drift rate
BO-p	331.9 km	89°	7 days	1.3°/ cycle
BO-i	342.6 km	70°		

6.4 Simulations and analysis

In this section, two basic orbits are chosen to form double-pair and triple-pair constellations to show the influence of phase sampling of the ocean tides on the recovered tidal fields. The basic orbits are shown in Table 6.3. One is a polar orbit (BO-p) and the other one is an inclined orbit (BO-i). Both of them are drifting orbits with a 7-day drift cycle and a drift rate of 1.3°/cycle. The drift cycle and the homogeneity are shown in Figure 6.3.

The simulated constellations are listed in Table 6.4. The simulation includes the single-pair GRACE-type (S-p), double-pair with two polar orbit (D*-pp), Bender-type (B*-pi), Triple-pair (T*). The orbits are separated by the optimal nodal difference of M_2 for double-pair (see Table 6.1) and triple-pair (see Table 6.2), being perpendicular or parallel. Please see more information about scenario designations and brief descriptions in Table 6.4.

All the constellations in Table 6.4 are simulated with two types of inputs: (1) M_2, and (2) all 8 major tides. The simulation length is 182 days, which covers all the aliasing periods of each constituent except for the K_1 and K_2 regarding polar pair, see Table 6.5. The inputs are the ocean tide errors, EOT08a – GOT4.7, and the outputs are the aliased fields of ocean tide errors. Therefore, smaller magnitudes of the recovered fields indicate better self-dealiasing of the mission. The recovery period is 7 days, the same as the drift cycle of the orbits.

Figure 6.6 and 6.7 show the recovered tidal aliased fields of M_2. The following results are shown:

- the double-pair optimal DOP-pp performs almost the same as the perpendicular orbits D90-pp, with the sampled phases being different only in $(93.4-90)/\phi_{1\mathrm{d}}(M_2) \simeq 1.7°$;
- the DOP-pp and D90-pp constellations are better than the constellation of parallel orbits DPL-pp, which samples the M_2 tides in phase;
- the DPL-pp field shows a similar error in magnitude as single-pair formation S-p, which demonstrates that an added pair does not improve the recovered fields if the orbit is not designed properly;
- no significant difference arises from the different orbit separations regarding the Bender-type constellation, comparing BOP-pi, B90-pi and BPL-pi. This is expected

Table 6.4: The right ascensions of ascending nodes of the simulated scenarios.

scenario designation	brief description	Ω_1	Ω_2	Ω_3
S-p	**single pair**, polar	0°	-	-
DOP-pp	**double pair** 2 polar, optimal $\Delta\Omega$	0°	93.4°	-
DPL-pp	**double pair** 2 polar, parallel	0°	180°	-
D90-pp	**double pair** 2 polar, perpendicular	0°	90°	-
BOP-pi	**double pair**, polar + inclined optimal $\Delta\Omega$ for same $\dot{\Omega}$	0°	93.4°	-
BPL-pi	**double pair** polar + inclined, parallel	0°	180°	-
B90-pi	**double pair** polar + inclined, perpendicular	0°	90°	-
TOP-ppp	**triple pair** 3 polar, optimal $\Delta\Omega$	0°	62.3°	124.5°
T90PL-ppp	**triple pair**, 3 polar perpendicular + parallel	0°	90°	180°
T90OP-pip	**triple pair** polar + inclined + polar perpendicular + optimal $\Delta\Omega$	0°	90°	266.6°
T90PL-pip	**triple pair** polar + inclined + polar perpendicular + parallel	0°	90°	180°
T90OP-pii	**triple pair** polar + inclined + inclined perpendicular + optimal $\Delta\Omega$	0°	90°	183.4°
T90PL-pii	**triple pair** polar + inclined + inclined perpendicular + parallel	0°	90°	270°
T3POP-pip	**triple pair** polar + inclined + polar optimal $\Delta\Omega$ for same $\dot{\Omega}$	0°	62.3°	124.5°
T90PL-pii	**triple pair** polar + inclined + inclined optimal $\Delta\Omega$ for same $\dot{\Omega}$	0°	62.3°	124.5°

Table 6.5: Aliasing periods [day] of 8 major constituent for each orbit.

orbit	aliasing periods	M_2	N_2	S_2	K_2	O_1	P_1	Q_1	K_1
BO-p	T_a^p	13.5	9.1	155.2	1035.1	13.6	167.8	9.1	2070.1
	T_a^s	14.6	30.9	155.2	1035.1	14.5	167.8	30.4	2070.1
BO-i	T_a^p	10.9	7.8	41.0	52.8	12.1	66.9	8.4	105.7
	T_a^s	19.7	69.3	41.0	52.8	16.6	66.9	41.8	105.7

as no constant out-of-phase sampling can be kept for two orbits with different nodal rates;

- the Bender-type constellation is better than the single pair GRACE-type formation and double-pair DPL-pp, while it is worse than the double pair out-of-phase-sampling scenarios DOP-pp and D90-pp;
- for triple-pairs with two identical polar pairs and one inclined pair, or two identical inclined pairs and one polar pair, choosing the optimal orbit separation between the identical orbits always produces better results than the remaining options. The constellations with two identical orbits in parallel perform the worst;
- globally, triple-polar pairs with the optimal right ascensions of ascending nodes are the best in terms of the ocean tide self-dealiasing;
- in general perpendicular polar orbits improve the zonal and low order tesseral coefficients, and the perpendicular inclined orbits improve the sectoral and high order tesseral coefficients.

The scenarios with inputs of all 8 major tides show the same behaviour as M_2, which can be explained by the dominant magnitudes of M_2 compared to the rest for 8 major tides. As already shown in the first bullet of the above results, a small shift of the sampling phase does not affect the results significantly. Therefore, in general, the perpendicular orbits are better for the semi-diurnal tides and the parallel orbits are better for the diurnal tides. Comparing the parallel orbits with the (quasi) perpendicular orbits, e.g. DPL-pp and D90-pp, or T90PL-pip and T90OP-pip (quasi perpendicular), the perpendicular orbits are always better than the parallel orbits. This demonstrates that the semi-diurnal tides errors are larger than the diurnal tides and need special attention if minimizing the overall aliasing errors is one of the aims of future missions.

6.5 Summary

This chapter discussed the future mission design in terms of ocean tide mitigation. By making use of the orbit sampling of the ocean tide phases, a proper mission can be designed with the property of self-dealiasing. This is a promising view to mitigate the troublesome ocean tide aliasing errors without doing any data processing, which will be beneficial for the recovered gravity fields, especially for the possible application with

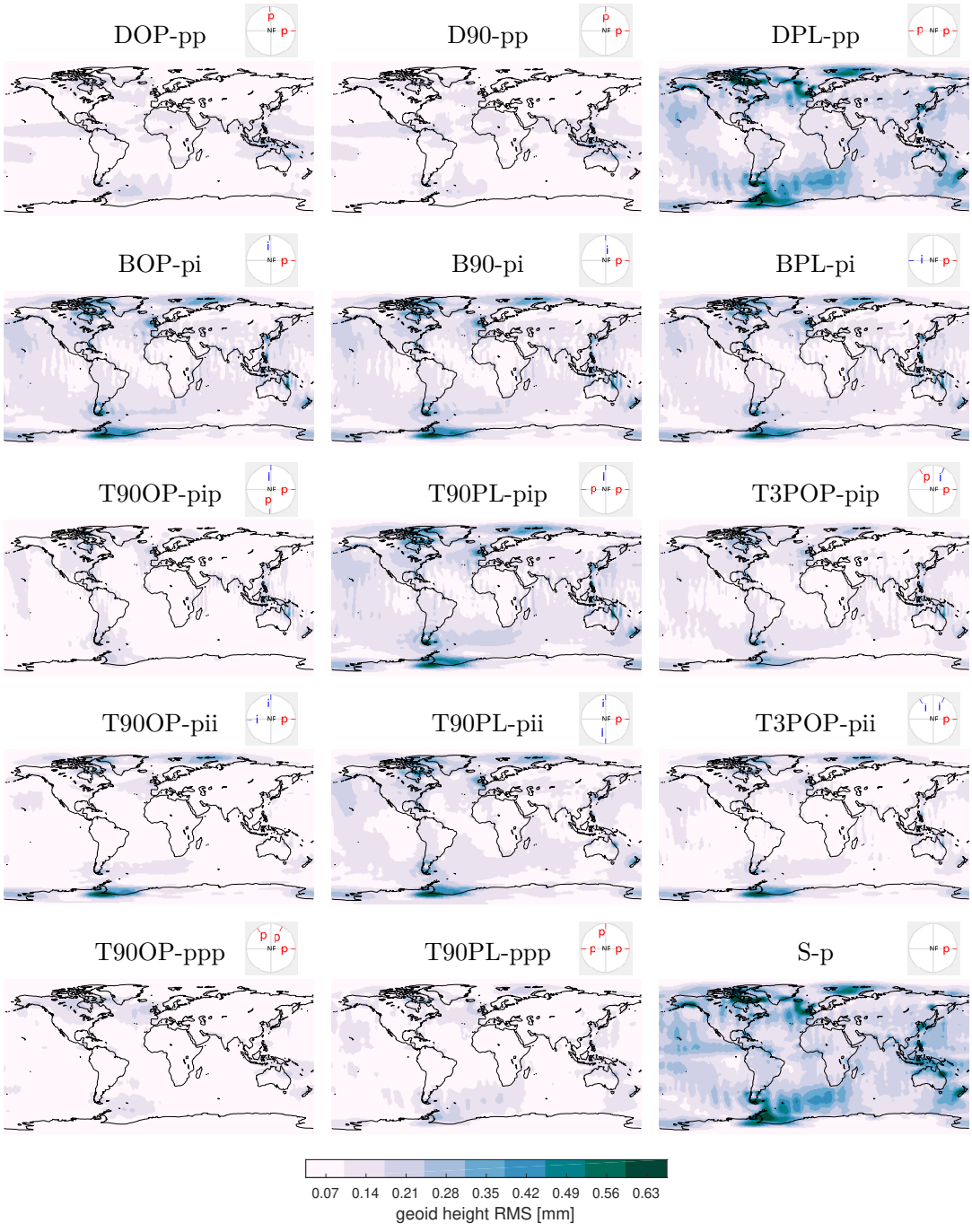

Figure 6.6: Geoid height RMS of the recovered fields for M_2. The sketch map at the top right of each single plot indicates the relative positions of the simulated orbits seeing from the north pole. The letter p stands for the polar orbit BO-p, and the letter i stands for the inclined orbit BO-i.

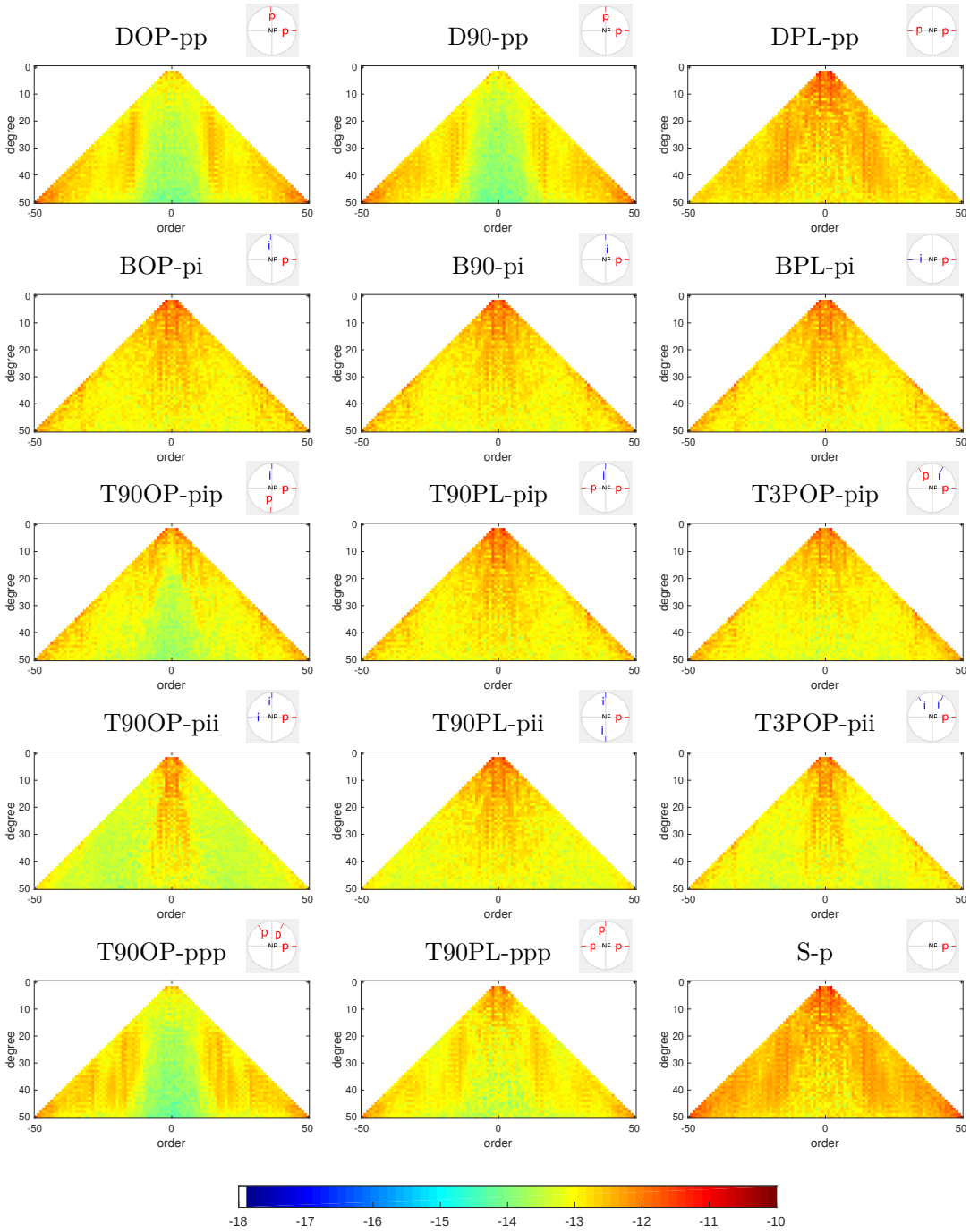

Figure 6.7: RMS of the individual spherical harmonic coefficients of the recovered fields for M_2. The sketch map at the top right of each single plot indicates the relative positions of the simulated orbits seeing from the north pole. The letter p stands for the polar orbit BO-p, and the letter i stands for the inclined orbit BO-i.

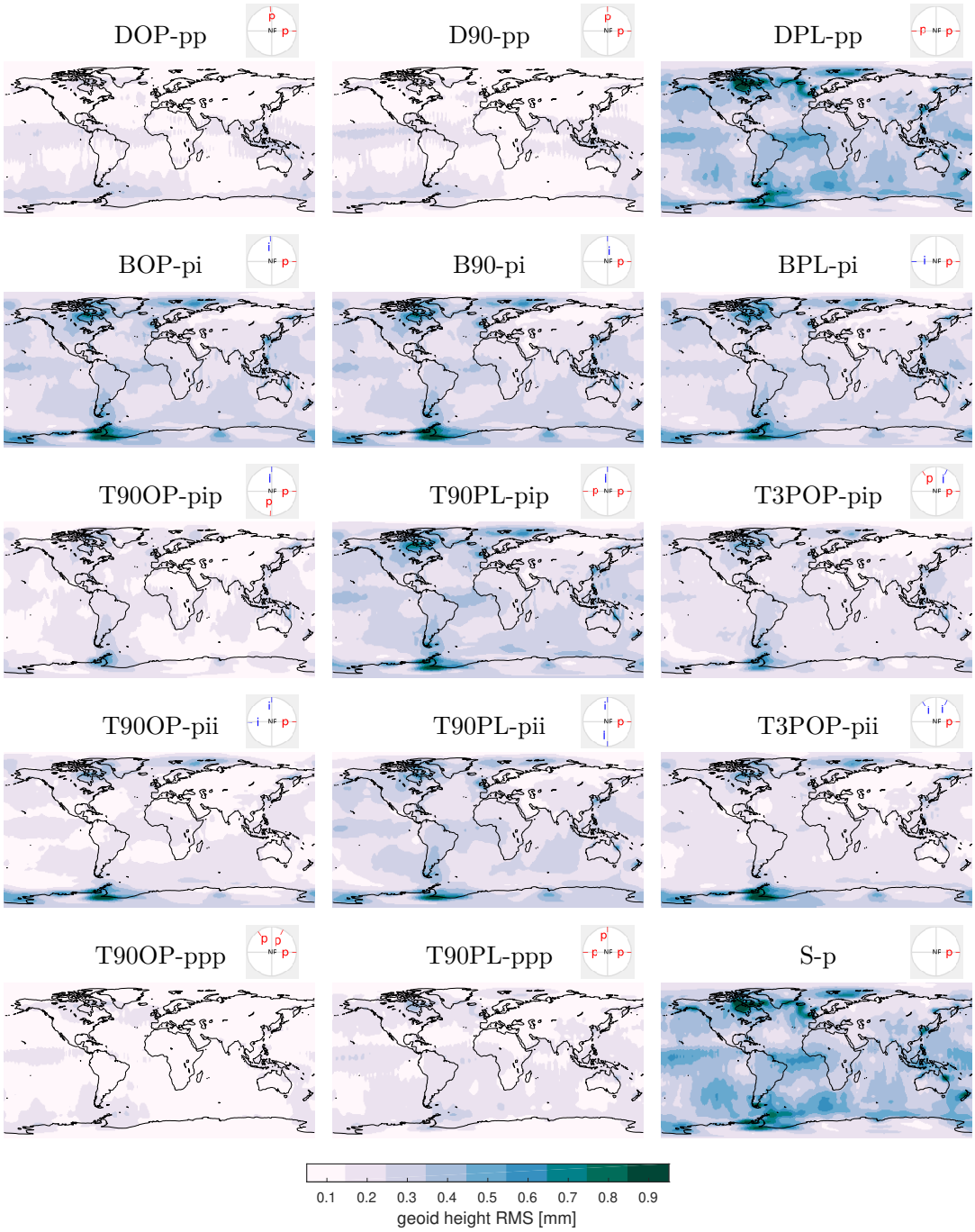

Figure 6.8: Geoid height RMS of the recovered fields for all 8 major tides. The sketch map at the top right of each single plot indicates the relative positions of the simulated orbits seeing from the north pole. The letter p stands for the polar orbit BO-p, and the letter i stands for the inclined orbit BO-i.

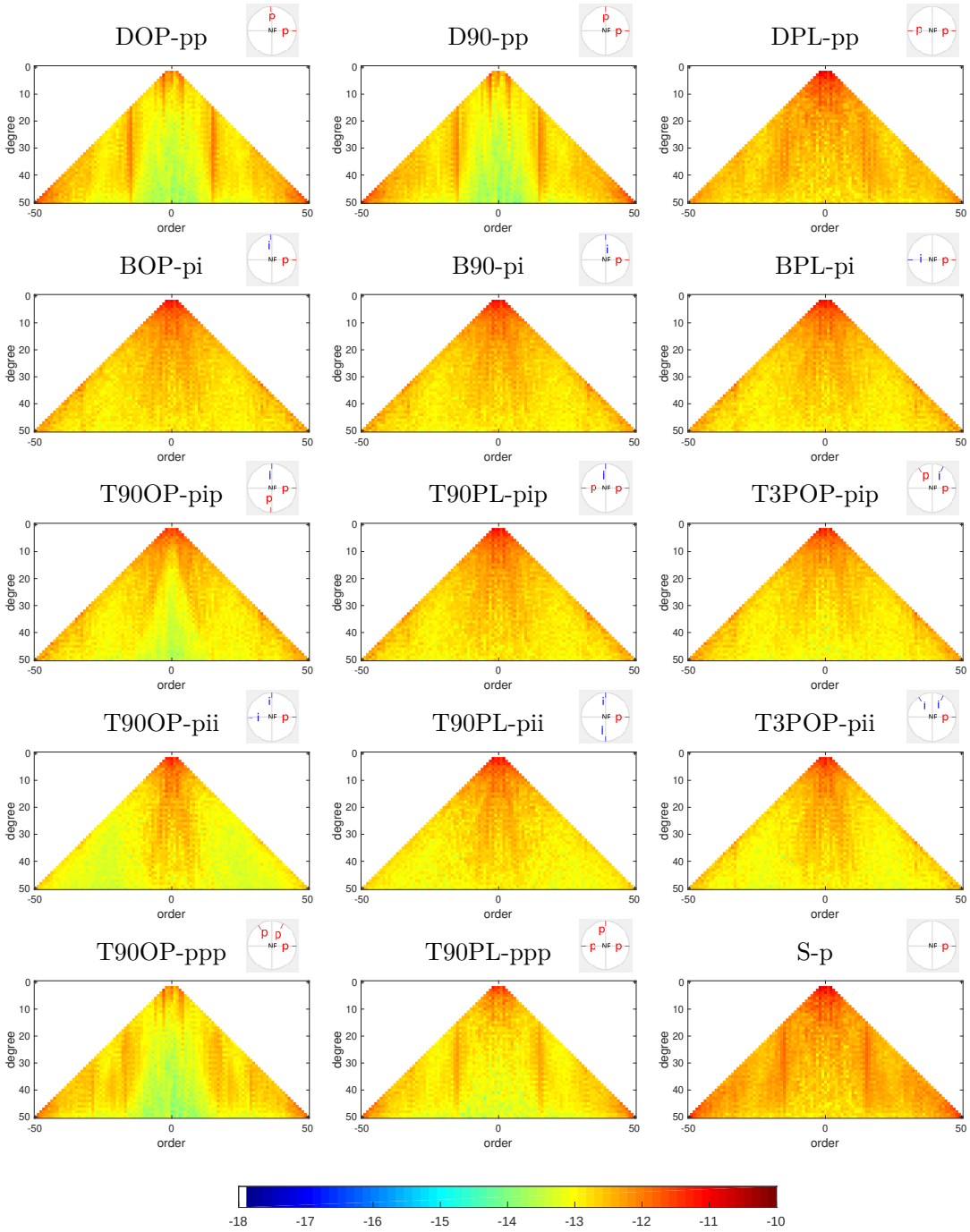

Figure 6.9: RMS of the individual spherical harmonic coefficients of the recovered fields for all 8 major tides. The sketch map at the top right of each single plot indicates the relative positions of the simulated orbits seeing from the north pole. The letter p stands for the polar orbit BO-p, and the letter i stands for the inclined orbit BO-i.

high timeliness, which may not allow the co-estimation or post-processing of the tides to remove the tidal aliasing effect. By designing the orbits with a proper $\Delta\Omega$ between orbits, the aliasing errors can be mitigated significantly automatically by the constellation itself. Same nodal rates of the orbits are needed to keep the designed out-of-phase sampling. Therefore, in terms of a double pair constellation, well-designed two identical polar pairs outperform the Bender-type for ocean tides self-dealiasing. In order to minimize the overall aliasing errors by orbit design, perpendicular orbits are better than the parallel orbits. Nevertheless, different aims can be chosen for the future mission in terms of dealing with ocean tide aliasing, as discussed in section 6.1.

CHAPTER 7

CONCLUSION AND OUTLOOK

7.1 Conclusion

THIS dissertation has systematically investigated the ocean tide aliasing problem in satellite gravimetry. Three main parts are included.

The first part, mainly covered by Chapter 3 and Chapter 4, is to understand the mechanism of the ocean tide aliasing. This includes elaborating a two-step mechanism of tide aliasing: primary aliasing and secondary aliasing. A primary aliasing is caused by the undersampling of the oceans tides by orbits. To achieve the primary aliasing, the ocean tides are considered as longitudinal uniform signals, which means the differences in amplitudes and phase lags for a given constituent at different longitudes are ignored. As the orbit sampling depends on the orbit precession, the primary aliasing periods depend on the orbit precession as well. The primary aliasing periods are demonstrated by the observations along the orbits, with the clear periodic patterns shown in the u-t cyclogram. These periodic patterns reflect the phase sampling of the the ocean tides by the orbits. The phase sampling by orbits can be used to design future missions aiming at mitigating ocean tide aliasing.

A secondary aliasing is due to undersampling of the primary aliased fields by gravity recovery process. In general, gravity recovery averages the data within the recovery periods at different spatial scales. The secondary aliasing occurs when the recovery period is no less than half the primary aliasing period, according to the Nyquist sampling rule. For some constituents under a given orbit sampling, the recovery period can be much smaller than the primary periods, e.g. K_2 and K_1 sampled by polar orbits. Strictly speaking, no secondary aliasing happens in this case. However, the same periods as the primary

aliasing are referred to for the secondary aliasing for better understanding and easier discussion. Another special case is that the orbits do not undersample the ocean tides but the recovery process undersamples them. This can happen to some long period tides with certain orbit sampling and recovery periods, which is not discussed specifically in this work. However, despite of the difference, those cases can follow the basic idea discussed in this work.

The aliasing behaviour of different regions and different spherical harmonic coefficients are investigated by spectral analysis of the recovered solutions. According to the Nyquist sampling rule, the spectral analysis can detect the spectral lines lower than two multiples of the recovery periods. Therefore, the spectral analysis only shows the spectrum of the secondary aliasing. The primary aliasing spectral lines can not be seen in the spectral analysis. Analysis shows that the energy distribution of different latitude bands are different. However, despite of different energy magnitudes, same spectral lines are shown for all the regions. The spectral analysis of spherical harmonic coefficients shows a richer spectrum than the spatial-wise analysis. This is because different coefficients are related to different spatial scales. The averaging of the orbit samplings at different spatial scales can be different in reality because of the complexity of the real ocean tides.

More complex cases occur when the recovery periods together with the orbit samplings generate solutions which contain different sampling combinations within different recovery intervals. This can be described by two aspects:

- the homogeneity of the groundtrack pattern within the single recovery periods;
- the consistency of the groundtrack patterns among different recovery intervals.

When the homogeneity and consistency of the groundtrack patterns are not satisfied, unique primary and secondary periods are not guaranteed. As a result, side aliasing frequencies show up due to the complex sampling and aliasing strategies among different solutions at different spatial scales. The side aliasing frequencies can only be detected by the spectral analysis of the residual gravity fields. However, the spectral analysis has its limitations:

- the residual gravity fields contain residuals from many sources other than ocean tides, which may affect the spectral lines determination largely or slightly;
- some spectral lines can not be detected according to the Nyquist sampling rule;
- some detected spectral lines are not precise due to the limited length of the data, according to the Rayleigh criteria.

The aliasing spectrum of the Bender-type constellation is investigated along with the GRACE-type formation. Results show that a Bender-type constellation can be treated as the simple stack of individual single pairs in terms of tide aliasing. In other words, the aliasing frequencies of a Bender-type constellation can be derived by analysing the

aliasing behaviour caused by each pair separately. Although the interference among different aliasing frequencies exist as a natural phenomenon, it needs no special treatment in terms of mitigating the aliasing errors.

The second part, covered by Chapter 5, discusses the reduction of the ocean tide aliasing errors in post-processing for different constellations and different processing strategies. In general, the primary aliasing affects the spherical harmonic coefficients in the whole spectra. The secondary aliasing has more influence on the zonal and lower order tesseral coefficients, which represent the latitude bands or large regions. This is due to the fact that averaging within a latitude band or a large region can be more likely consistent for different solutions, which satisfies the consistency averaging requirements for the secondary aliasing more precisely than the small regions and longitude bands, corresponding to the high order tesseral and sectorial coefficients. The primary and secondary aliasing should be estimated simultaneously to minimize the aliasing errors. In the complex cases, the side aliasing should be considered together with the primary and secondary aliasing. In general, about 10% of relative improvement can be expected by taking the side aliasing frequencies into consideration.

The recovered fields regarding different recovery periods show a reduction in magnitudes when increasing the length of the recovered period. This can be explained by the periodic characteristic of the ocean tides. When more samples are included in the averaging process, the averaged results are closer to the real mean.

The third part, covered by Chapter 6, is the orbit design of further missions considering the ocean tide aliasing. Two distinct tasks can be targeted regarding ocean tides when design further missions, namely ocean tide error mitigation and ocean tide signal extraction. Different criteria should be followed for different aims. In this work, the optimal orbits are investigated for mitigation of the ocean tide aliasing errors. In general, self-dealiasing can be achieved for a constellation by setting the orbit sampling of the ocean tides out of phase. The permanent out-of-phase sampling can be achieved only when different orbits have the same nodal rates. The optimal nodal separations are investigated for double- and triple-pair constellation for each single constituent, which shows the best performance of aliasing error mitigation for an individual constituent. As all the tides are sampled by the same orbits simultaneously in reality, a compromise should be made for different aims. In terms of mitigating the overall aliasing errors, the perpendicular orbits are recommended over the parallel orbits. Apart from that, the aliasing periods should be short for a fast aliasing error reduction conducted in post-processing, if needed.

7.2 Discussion and outlook

THIS This work has clarified the ocean tide aliasing mechanism in satellite gravimetry, discussed the strategies of reducing the ocean tide aliasing errors in post-processing

and mitigating the aliasing errors by mission design. Some further questions can be considered under the frame of the aliasing mechanism developed in this work.

Uneven sampling effect The influence of the uneven sampling of ocean tides on the aliased fields should be evaluated. The unevenly sampling may be due to changing orbit precession, varying recovery periods or data gaps. In theory, it can be explained similar to the case of inhomogeneous or (and) inconsistent groundtrack patterns, which induces more side aliasing frequencies other than primary and secondary aliasing. The difference is that the analytical formula which needs a specific sampling frequency may not be applicable for the uneven sampling, depending on whether the averaged sampling frequency can be used or not. In this case, spectral analysis of the residual fields may be the only approach to derive the aliasing spectrum. Nevertheless, the limitations of the spectral analysis, as discussed in this work, are unavoidable.

Ocean tide signal extraction The ocean tide signal extraction can be considered in the frame of the two-step aliasing mechanism. The first concern is that the aliasing periods of different constituents should be distinct from each other considerably, depending on the time span of the data (cf. Rayleigh criteria), to have a better separation of the tides. This is can be achieved to some extent by choosing proper orbit parameters like altitude and inclination. It is not fully achievable because (1) the lifetime of the mission is normally limited, and (2) the choice of altitude and inclination is limited by other scientific aims or applications.

The second concern is that the ocean tide signals should be kept other than reduced by orbit sampling. According to the experience of the satellite altimetry, longer time span can give a better estimation of the tides. However, it may not be true when modelling the ocean tides with satellite gravimetry. It should be reminded that the final products are derived point-wisely and instantaneously in satellite altimetry, while the global solutions are recovered within certain periods in satellite gravimetry. This spatially and temporally averaged solutions can reduce the magnitudes of the signals largely or slightly, depending on the relative length between the averaged periods and the recovery periods, as well as the spatial distribution of the signal. If one would like to extract the ocean tide signals from the recovered field time series in post-processing, the possible reduction in magnitude because of the spatial and temporal averaging can cause the underestimation of the tide signal. Therefore, the reduction effect should be evaluated in advance in this case. For the ocean tide co-estimation, no averaging effect is involved. Instead, one needs to consider the proper maximum degree/order to be parametrized for the ocean tides.

The third concern is that the data length used for ocean tide extraction should cover the length of the aliasing periods for individual estimated constituents. Otherwise, the phase information is not sufficient for precisely estimating such a periodic signal for each constituent. Further investigations are needed for all the topics mentioned above.

Bibliography

Andersen, O. B. (1999). "Shallow water tides in the northwest European shelf region from TOPEX/POSEIDON altimetry." In: *Journal of Geophysical Research: Oceans* 104.C4, pp. 7729–7741. ISSN: 2156-2202. DOI: 10.1029/1998JC900112.

Bender, P., D. Wiese, and R. Nerem (2008). "A possible dual-GRACE mission with 90 degree and 63 degree inclination orbits." In: *Proceedings of the third international symposium on formation flying, missions and technologies*. ESA/ESTEC, pp. 23–25.

Cartwright, D. E. and A. C. Edden (1973). "Corrected Tables of Tidal Harmonics." In: *Geophysical Journal International* 33.3, pp. 253–264. ISSN: 0956-540X. DOI: 10.1111/j.1365-246X.1973.tb03420.x.

Cartwright, D. E. and R. D. Ray (1990). "Oceanic tides from Geosat altimetry." In: *J. Geophys. Res.* 95.C3, pp. 3069–3090. ISSN: 2156-2202. DOI: 10.1029/JC095iC03p03069.

Cartwright, D. E. (1993). "Theory of ocean tides with application to altimetry." In: *Satellite altimetry in geodesy and oceanography*. Springer, pp. 100–141.

Cartwright, D. E. and R. D. Ray (1991). "Energetics of global ocean tides from Geosat altimetry." In: *Journal of Geophysical Research: Oceans* 96.C9, pp. 16897–16912. ISSN: 2156-2202. DOI: 10.1029/91JC01059.

Chen, J., C. Wilson, and K.-W. Seo (2009). "S2 tide aliasing in GRACE time-variable gravity solutions." In: *Journal of Geodesy* 83.7, pp. 679–687. ISSN: 0949-7714. DOI: 10.1007/s00190-008-0282-1.

Cheng, M. K. (2002). "Gravitational perturbation theory for intersatellite tracking." In: *Journal of Geodesy* 76.3, pp. 169–185. ISSN: 1432-1394. DOI: 10.1007/s00190-001-0233-6.

Cheng, M. and J. Ries (2017). "The unexpected signal in GRACE estimates of C_{20}." In: *Journal of Geodesy* 91.8, pp. 897–914. ISSN: 0949-7714. DOI: 10.1007/s00190-016-0995-5.

Darwin, G. (1883). "Reports of a committee for the harmonic analysis of tides." In: *British Association for the Advancement of Science* 86.

Davis, J., P Elósegui, J. Mitrovica, and M. Tamisiea (2004). "Climate-driven deformation of the solid Earth from GRACE and GPS." In: *Geophysical Research Letters* 31.24, p. L24605. ISSN: 0094-8276. DOI: 10.1029/2004GL021435.

Doodson, A. T. (1921). "The harmonic development of the tide-generating potential." In: *Proceedings of the Royal Society of London. Series A, Containing Papers of a Mathematical and Physical Character*, pp. 305–329. ISSN: 0950-1207.

Dow, J. (1988). "Ocean tides and tectonic plate motions from Lageos." Dessertation, Reihe C (344). Heft: Deutsche Geodätische Kommission.

Drinkwater, M., R Floberghagen, R Haagmans, D Muzi, and A Popescu (2003). "GOCE: ESA's first earth explorer core mission." In: *Space Science Reviews* 108.1-2, pp. 419–432. ISSN: 0038-6308.

Flechtner, F., K.-H. Neumayer, C. Dahle, H. Dobslaw, E. Fagiolini, J.-C. Raimondo, and A. Guentner (2016). "What can be expected from the GRACE-FO Laser Ranging Interferometer for Earth Science applications?" In: *Surveys in Geophysics*, pp. 1–18. ISSN: 0169-3298. DOI: 10.1007/s10712-015-9338-y.

Han, S.-C., C Jekeli, and C. Shum (2002). "Aliasing and polar gap effects on geopotential coefficient estimation: space-wise simulation study of GOCE and GRACE." In: *Vistas for Geodesy in the New Millennium*. Springer, pp. 181–186.

Han, S.-C., C. Jekeli, and C. K. Shum (2004). "Time-variable aliasing effects of ocean tides, atmosphere, and continental water mass on monthly mean GRACE gravity field." In: *J. Geophys. Res.* 109.B4, B04403. ISSN: 2156-2202. DOI: 10.1029/2003JB002501.

Han, S.-C., C. Shum, and K. Matsumoto (2005). "GRACE observations of M2 and S2 ocean tides underneath the Filchner-Ronne and Larsen ice shelves, Antarctica." In: *Geophysical research letters* 32.20, p. L20311. ISSN: 1944-8007. DOI: 10.1029/2005GL024296.

Han, S.-C., C. Shum, M. Bevis, C. Ji, and C.-Y. Kuo (2006). "Crustal dilatation observed by GRACE after the 2004 Sumatra-Andaman earthquake." In: *Science* 313.5787, pp. 658–662. ISSN: 0036-8075. DOI: 10.1126/science.1128661.

Han, S.-C., R. D. Ray, and S. B. Luthcke (2007). "Ocean tidal solutions in Antarctica from GRACE inter-satellite tracking data." In: *Geophysical Research Letters* 34.21, p. L21607. ISSN: 1944-8007. DOI: 10.1029/2007GL031540.

— (2010). "One centimeter-level observations of diurnal ocean tides from global monthly mean time-variable gravity fields." In: *Journal of Geodesy* 84.12, pp. 715–729. ISSN: 0949-7714. DOI: 10.1007/s00190-010-0405-3.

Hauk, M. and R. Pail (2018). "Treatment of ocean tide aliasing in the context of a next generation gravity field mission." In: *Geophysical Journal International* 214.1, pp. 345–365. ISSN: 0956-540X. DOI: 10.1093/gji/ggy145.

Hicks, S., R. Sillcox, C. Nichols, B Via, and E. McCray (2000). "Tide and current glossary." In: *Silver Spring, MD*, pp. 1–29.

Hicks, S. D. and M. W. Szabados (2006). *Understanding tides*. US Department of Commerce, National Oceanic and Atmospheric Administration, National Ocean Service.

Hofmann-Wellenhof, B. and H. Moritz (2006). *Physical geodesy*. Springer Science & Business Media.

Kaula, W. M. (2000). *Theory of Satellite Geodesy: Application of Satellites to Geodesy*. Dover Publications, inc., Mineola, New York.

Knudsen, P. (2003). "Ocean tides in GRACE monthly averaged gravity fields." In: *Space Science Reviews* 108.1-2, pp. 261–270. ISSN: 0038-6308. DOI: 10.1023/A:1026215124036.

Knudsen, P. and O. Andersen (2002). "Correcting GRACE gravity fields for ocean tide effects." In: *Geophys. Res. Lett.* 29.8, pp. 19–1–19–4. ISSN: 1944-8007. DOI: 10.1029/2001GL014005.

Koop, R. and R. Rummel (2007). "The future of satellite gravimetry." In: *Report from the workshop on the future of satellite gravimetry*. Vol. 113.

Le Provost, C, M. Genco, F Lyard, P Vincent, and P Canceil (1994). "Spectroscopy of the world ocean tides from a finite element hydrodynamic model." In: *Journal of Geophysical Research: Oceans* 99.C12, pp. 24777–24797. ISSN: 2156-2202.

Leuliette, E. W. and L. Miller (2009). "Closing the sea level rise budget with altimetry, Argo, and GRACE." In: *Geophys. Res. Lett.* 36.4. ISSN: 1944-8007. DOI: 10.1029/2008GL036010.

Liu, W., N. Sneeuw, S. I. Pour, M. J. Tourian, and T. Reubelt (2016). "A Posteriori Dealiasing of Ocean Tide Error in Future Double-Pair Satellite Gravity Missions." In: *International Symposium on Earth and Environmental Sciences for Future Generations*. Ed. by S. L. Freymueller J.T. Vol. International Association of Geodesy Symposia, vol 147. Cham: Springer International Publishing, pp. 103–109. DOI: 10.1007/1345_2016_259.

Luthcke, S. B., A. A. Arendt, D. D. Rowlands, J. J. McCarthy, and C. F. Larsen (2008). "Recent glacier mass changes in the Gulf of Alaska region from GRACE mascon solutions." In: *J. Glaciol.* 54.188, pp. 767–777. ISSN: 0022-1430. DOI: 10.3199/002214309797779933.

Lyard, F., F. Lefevre, T. Letellier, and O. Francis (2006). "Modelling the global ocean tides: modern insights from FES2004." In: *Ocean Dynamics* 56.5-6, pp. 394–415. ISSN: 1616-7341. DOI: 10.1007/s10236-006-0086-x.

Mayer-Gürr, T, R Savcenko, W Bosch, I Daras, F Flechtner, and C. Dahle (2012). "Ocean tides from satellite altimetry and GRACE." In: *Journal of Geodynamics* 59, pp. 28–38. ISSN: 0264-3707.

Munk, W. H. and D. E. Cartwright (1966). "Tidal spectroscopy and prediction." In: *Philosophical Transactions of the Royal Society of London A: Mathematical, Physical and Engineering Sciences* 259.1105, pp. 533–581. ISSN: 1364-503X.

Nyquist, H. (1928). "Certain Topics in Telegraph Transmission Theory." In: *Transactions of the American Institute of Electrical Engineers* 47.2, pp. 617–644. ISSN: 0096-3860. DOI: 10.1109/T-AIEE.1928.5055024.

Parke, M. E., R. H. Stewart, D. L. Farless, and D. E. Cartwright (1987). "On the choice of orbits for an altimetric satellite to study ocean circulation and tides." In: *J. Geophys. Res.* 92.C11, pp. 11693–11707. ISSN: 2156-2202. DOI: 10.1029/JC092iC11p11693.

Petit, G. and B. Luzum (2010). *IERS techinical no.36, IERS conventions (2010)*. Tech. rep. International Earth Rotation and Reference Systems Service, Frankfurt, Germany.

Pugh, D. T. (1996). *Tides, surges and mean sea-level (reprinted with corrections)*. John Wiley & Sons Ltd.

Ray, R. and S. Luthcke (2006). "Tide model errors and GRACE gravimetry: towards a more realistic assessment." In: *Geophysical Journal International* 167.3, pp. 1055–1059. ISSN: 0956-540X. DOI: 10.1111/j.1365-246X.2006.03229.x.

Ray, R. D. (1999). "A global ocean tide model from TOPEX/POSEIDON altimetry: GOT99. 2." In: *NASA Tech. Memo. 209478*. pp. 1–58.

Ray, R. D., D. Rowlands, and G. Egbert (2003). "Tidal models in a new era of satellite gravimetry." In: *Space Science Reviews* 108.1-2, pp. 271–282. ISSN: 0038-6308. DOI: 10.1023/A:1026223308107.

Reigber, C., P Schwintzer, and H Lühr (1999). "The CHAMP geopotential mission." In: *Boll. Geof. Teor. Appl* 40, pp. 285–289.

Rodell, M., I. Velicogna, and J. S. Famiglietti (2009). "Satellite-based estimates of groundwater depletion in India." In: *Nature* 460.7258, pp. 999–1002. ISSN: 0028-0836. DOI: 10.1038/nature08238.

Savcenko, R and W Bosch (2008). "EOT08a-a new global ocean tide model derived by empirical analysis of multi-mission altimetry data." In: *Geophys. Res. Abst., 10, EGU2008-A* 7470.

Savcenko, R. and W. Bosch (2012). *EOT11a-empirical ocean tide model from multi-mission satellite altimetry*. Deutsches Geodätisches Forschungsinstitut (DGFI).

Schlax, M. G. and D. B. Chelton (1994). "Detecting aliased tidal errors in altimeter height measurements." In: *J. Geophys. Res* 99, pp. 12,603–12,612. ISSN: 0148-0227. DOI: 10.1029/94JC00568.

Schrama, E. J. O. and P. N. A. M. Visser (2007). "Accuracy assessment of the monthly GRACE geoids based upon a simulation." In: *Journal of Geodesy* 81.1, pp. 67–80. ISSN: 1432-1394. DOI: 10.1007/s00190-006-0085-1.

Schrama, E. (2003). "Error characteristics estimated from CHAMP, GRACE and GOCE derived geoids and from satellite altimetry derived mean dynamic topography." In: *Earth Gravity Field from Space–From Sensors to Earth Sciences*. Springer, pp. 179–193. DOI: 10.1007/978-94-017-1333-7_15.

Schrama, E. J. (2011). *Tides*. Lecture Notes. Delft University of Technology, Faculty of Areospace Engineering.

Schureman, P. (1958). *Manual of harmonic analysis and prediction of tides*.

Schwiderski, E. W (1980a). "On charting global ocean tides." In: *Reviews of Geophysics* 18.1, pp. 243–268. ISSN: 1944-9208. DOI: 10.1029/RG018i001p00243.

Schwiderski, E. W. (1980b). "Ocean tides, part I: global ocean tidal equations." In: *Marine Geodesy* 3.1-4, pp. 161–217. ISSN: 0149-0419.

Schwiderski, E. W. (1983). "Atlas of ocean tidal charts and maps, part I: The semidiurnal principal lunar tide M2." In: *Marine Geodesy* 6.3-4, pp. 219–265. ISSN: 0149-0419.

Seo, K. W., C. R. Wilson, S. C. Han, and D. E. Waliser (2008a). "Gravity Recovery and Climate Experiment (GRACE) alias error from ocean tides." In: *J. Geophys. Res.* 113.B3, B03405. ISSN: 2156-2202. DOI: 10.1029/2006JB004747.

Seo, K.-W., C. R. Wilson, J. Chen, and D. E. Waliser (2008b). "GRACE's spatial aliasing error." In: *Geophysical Journal International* 172.1, pp. 41–48. DOI: 10.1111/j.1365-246X.2007.03611.x.

Shannon, C. E. (1949). "Communication in the Presence of Noise." In: *Proceedings of the IRE* 37.1, pp. 10–21. ISSN: 0096-8390. DOI: 10.1109/JRPROC.1949.232969.

Sheard, B. S., G. Heinzel, K. Danzmann, D. A. Shaddock, W. M. Klipstein, and W. M. Folkner (2012). "Intersatellite laser ranging instrument for the GRACE follow-on mission." In: *Journal of Geodesy* 86.12, pp. 1083–1095. ISSN: 1432-1394. DOI: 10.1007/s00190-012-0566-3.

Smith, A. J. E. (1999). "Application of satellite altimetry for global ocean tide modeling." Dissertation. TU Delft: Delft University of Technology.

Sneeuw, N. (2000). "A semi-analytical approach to gravity field analysis from satellite observations." Doctoral dissertation. Institute of Astronomical and Physical Geodesy, Technical University of Munich.

Stammer, D., R. D. Ray, O. B. Andersen, B. K. Arbic, W. Bosch, L. Carrère, Y. Cheng, D. S. Chinn, B. D. Dushaw, G. D. Egbert, S. Y. Erofeeva, H. S. Fok, J. A. M. Green, S. Griffiths, M. A. King, V. Lapin, F. G. Lemoine, S. B. Luthcke, F. Lyard, J. Morison, M. Müller, L. Padman, J. G. Richman, J. F. Shriver, C. K. Shum, E. Taguchi, and Y. Yi (2014). "Accuracy assessment of global barotropic ocean tide models." In: *Rev. Geophys.* 52.3, pp. 243–282. ISSN: 1944-9208. DOI: 10.1002/2014RG000450.

Swenson, S. and J. Wahr (2006). "Post-processing removal of correlated errors in GRACE data." In: *Geophys. Res. Lett.* 33.8, p. L08402. ISSN: 1944-8007. DOI: 10.1029/2005GL025285.

Tapley, B. D., S Bettadpur, M Watkins, and C. Reigber (2004). "The gravity recovery and climate experiment: Mission overview and early results." In: *Geophysical Research Letters* 31.9, p. L09607. ISSN: 1944-8007. DOI: 10.1029/2004GL019920.

Thompson, P. F., S. V. Bettadpur, and B. D. Tapley (2004). "Impact of short period, non-tidal, temporal mass variability on GRACE gravity estimates." In: *Geophys. Res. Lett.* 31.6, p. L06619. ISSN: 1944-8007. DOI: 10.1029/2003GL019285.

Tourian, M. J. (2013). "Application of spaceborne geodetic sensors for hydrology." Doctoral dissertation. University of Stuttgart.

Visser, P. N. A. M., N. Sneeuw, T. Reubelt, M. Losch, and T. Van Dam (2010). "Space-borne gravimetric satellite constellations and ocean tides: aliasing effects." In: *Geophysical Journal International* 181.2, pp. 789–805. ISSN: 1365-246X. DOI: 10.1111/j.1365-246X.2010.04557.x.

Wiese, D. N., P. Visser, and R. S. Nerem (2011). "Estimating low resolution gravity fields at short time intervals to reduce temporal aliasing errors." In: *Advances in Space Research* 48.6, pp. 1094–1107. ISSN: 0273-1177. DOI: 10.1016/j.asr.2011.05.027.

APPENDIX A

Appendix 1 Mitigation in post-processing

Figures below shows the geoid height RMS and RMS of individual spherical harmonic coefficients of S_2, N_2, K_2, O_1, P_1, Q_1 and K_1 for the recovered fields and de-aliased fields with respect to different aliasing periods. See the related discussion in Chapter 5.

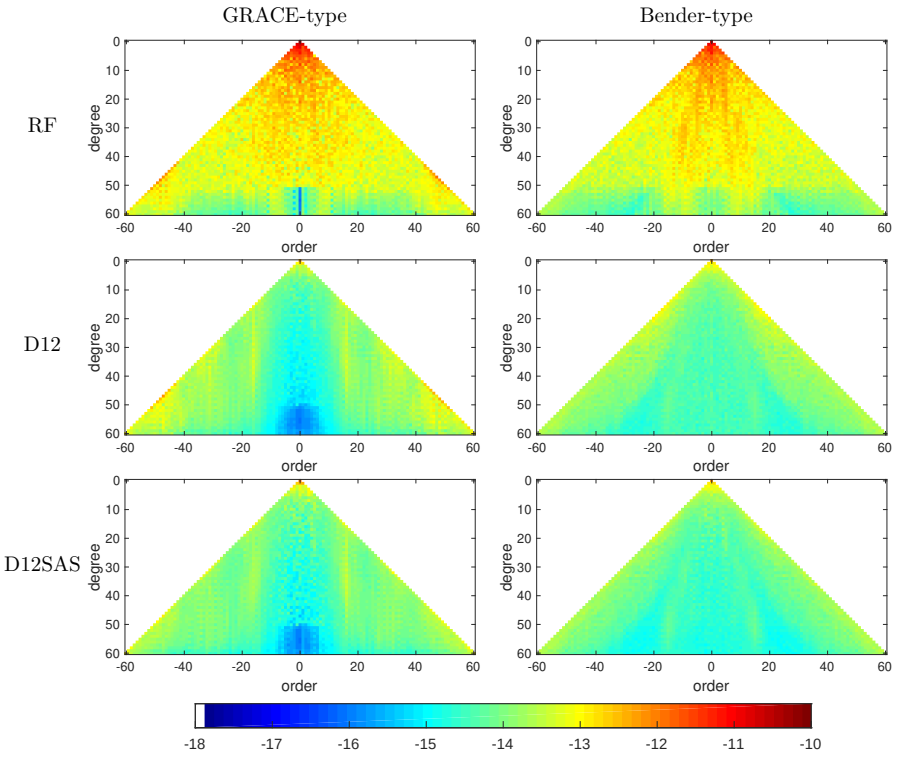

Figure A.1: RMS of individual spherical harmonic coefficients of S_2 for three fields: RF, D12 and D12SAS.

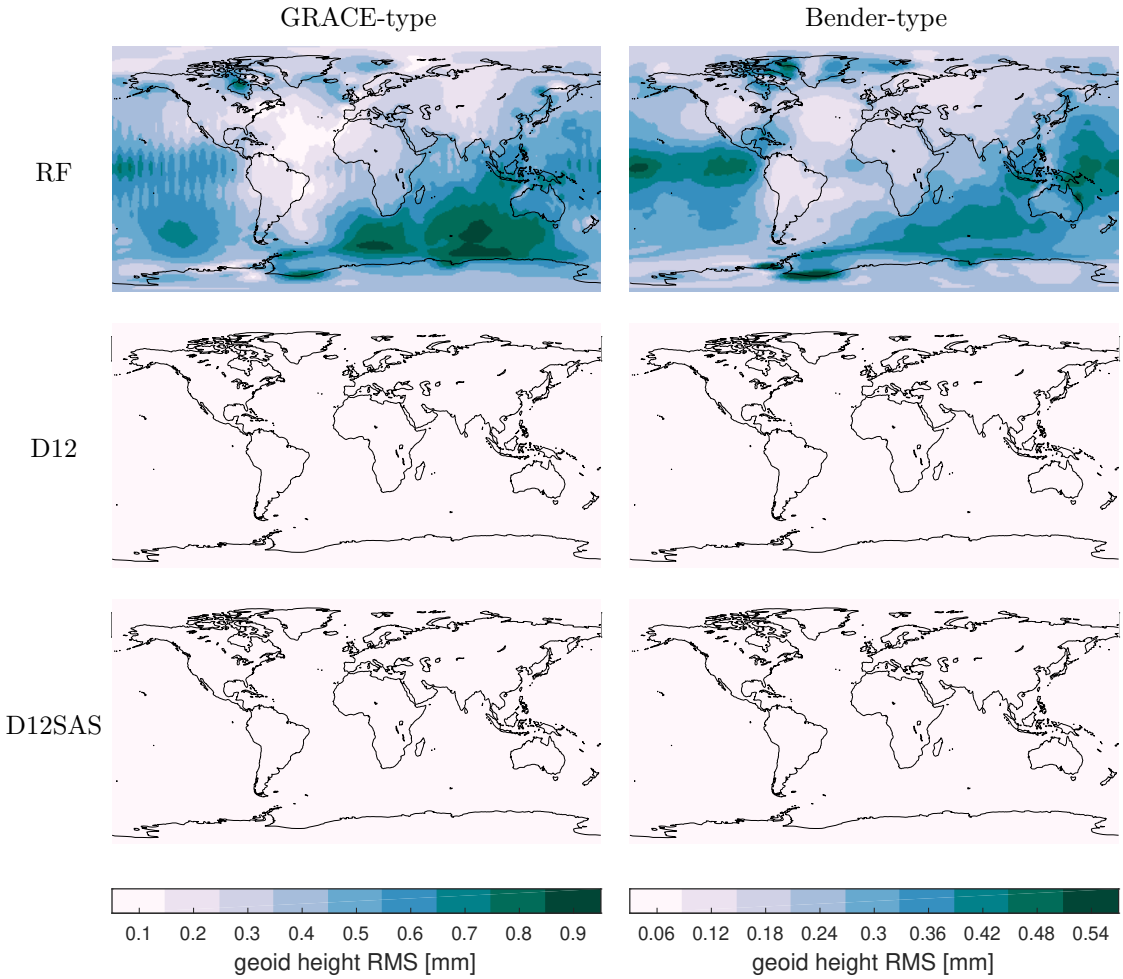

Figure A.2: Geoid height RMS [mm] of S_2 for three fields: RF, D12 and D12SAS. Each colorbar is valid for its column. Please note the different colorbar ranges for GRACE-type scenario and Bender-type scenario.

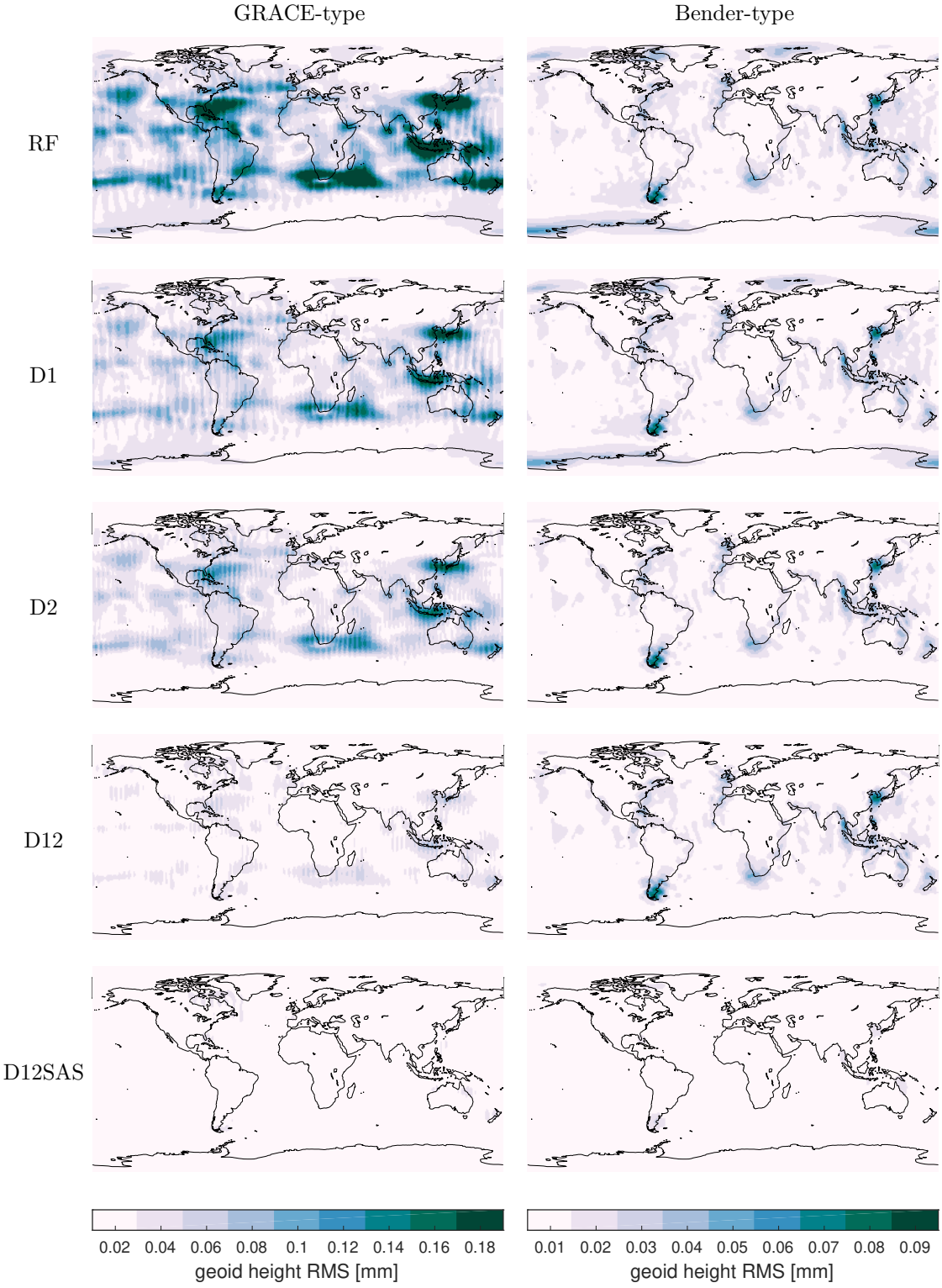

Figure A.3: Geoid height RMS [mm] of N_2 for five fields: RF, D1, D2, D12 and D12SAS. Each colorbar is valid for its column. Please note the different colorbar ranges for GRACE-type scenarios and Bender-type scenarios.

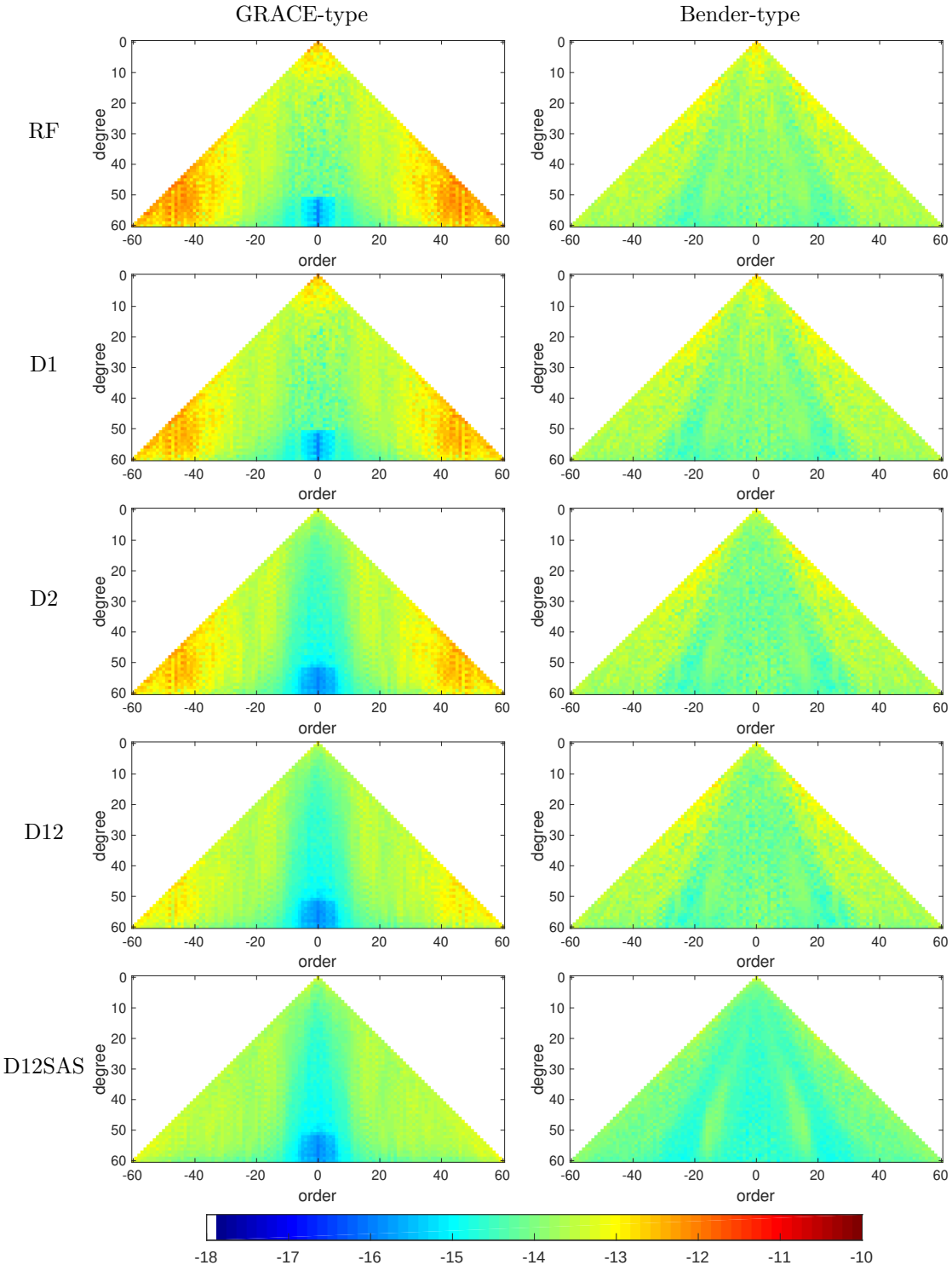

Figure A.4: RMS of individual spherical harmonic coefficients of N_2 for five fields: RF, D1, D2, D12 and D12SAS.

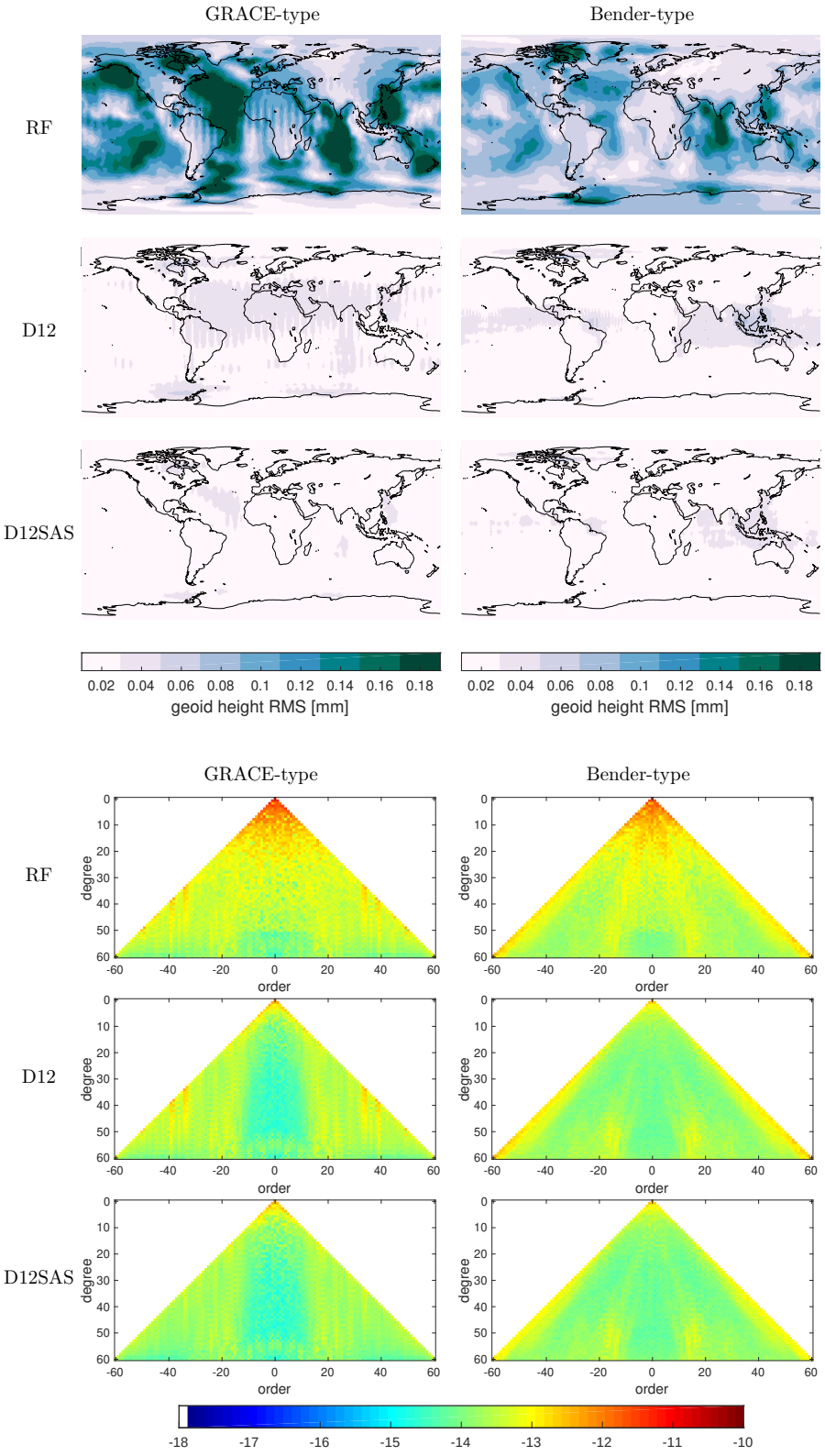

Figure A.5: Geoid height RMS [mm] (top panel) and RMS of individual spherical harmonic coefficients of K_2 for three fields: RF, D12 and D12SAS.

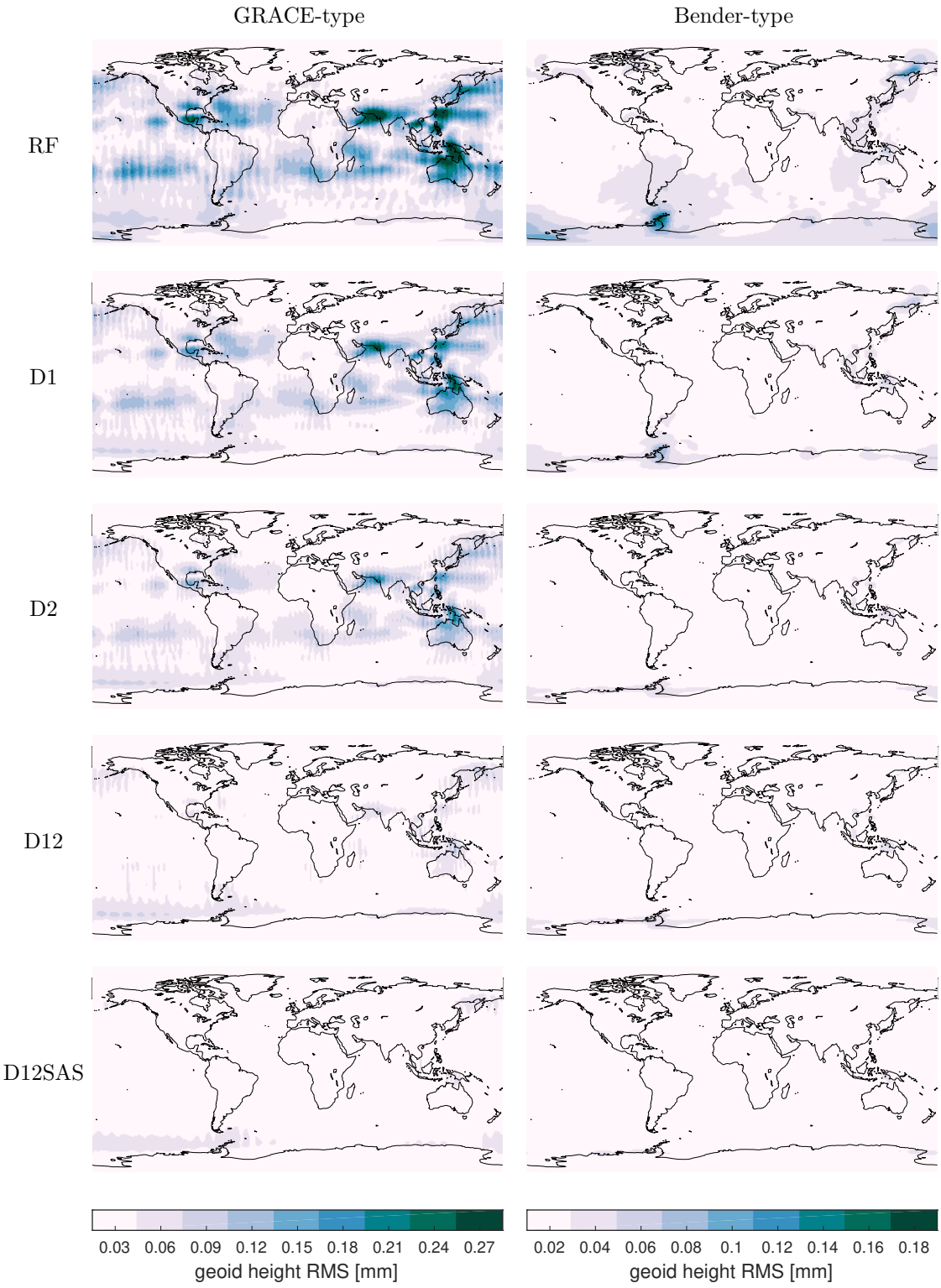

Figure A.6: Geoid height RMS [mm] of O_1 for five fields: RF, D1, D2, D12 and D12SAS. Each colorbar is valid for its column. Please note the different colorbar ranges for GRACE-type scenarios and Bender-type scenarios.

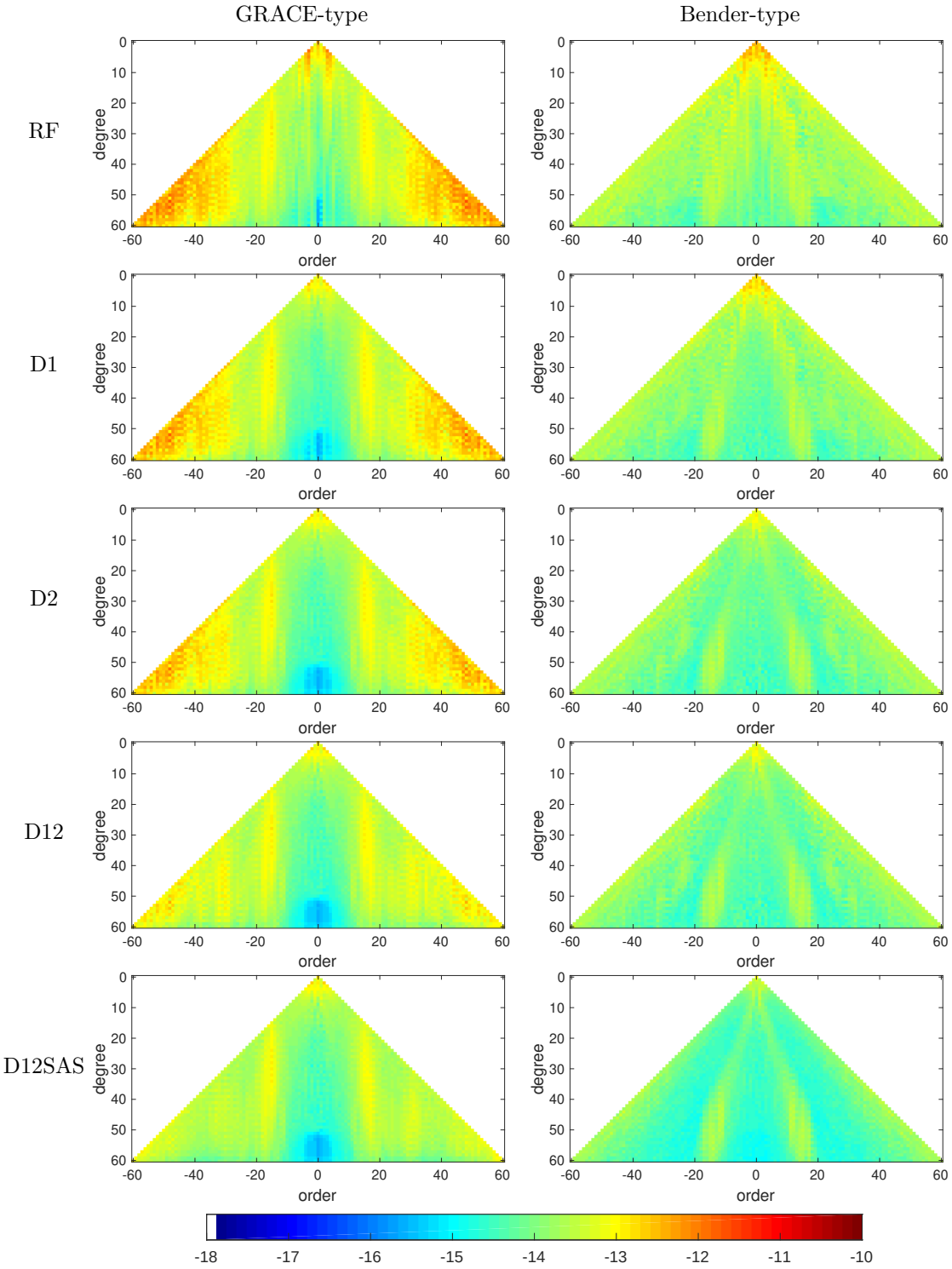

Figure A.7: RMS of individual spherical harmonic coefficients of O_1 for five fields: RF, D1, D2, D12 and D12SAS.

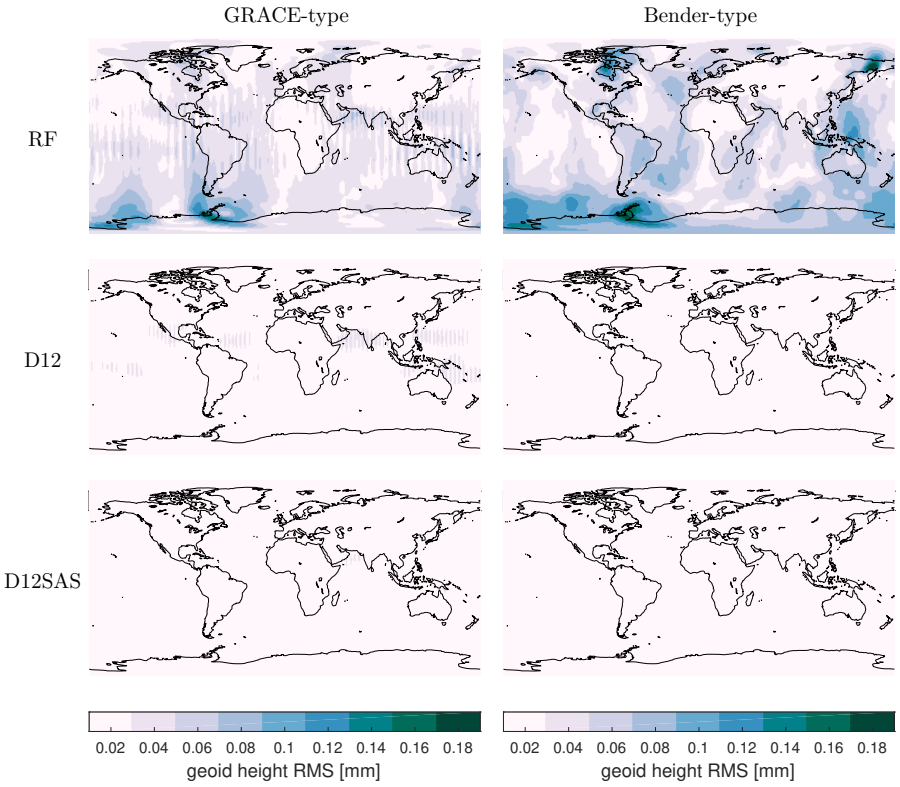

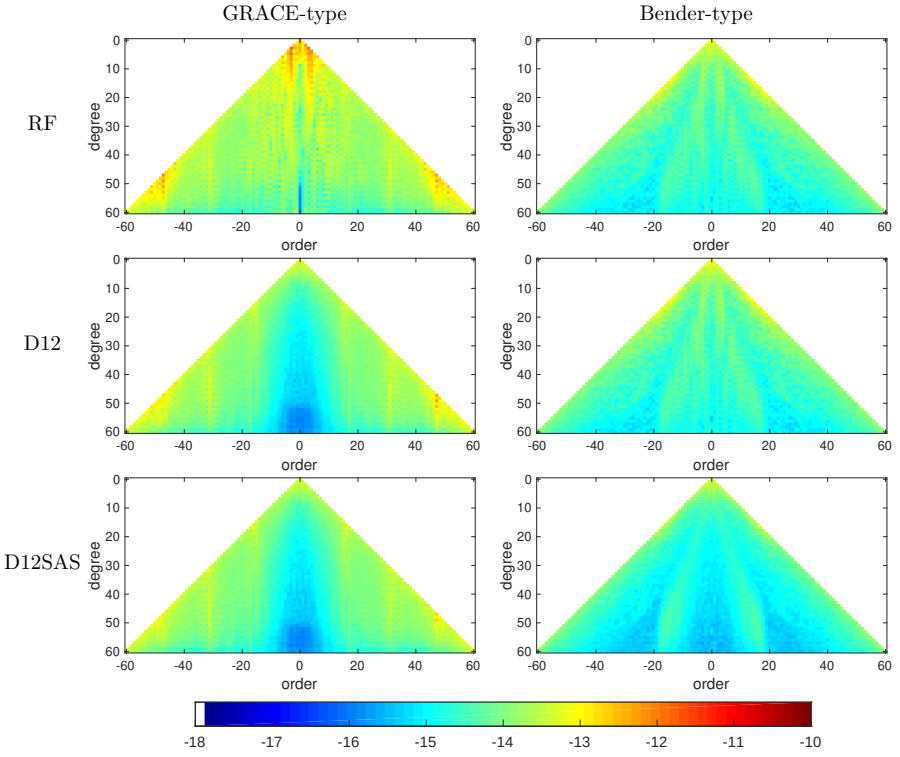

Figure A.8: Geoid height RMS [mm] and RMS of individual spherical harmonic coefficients of P_1 for three fields: RF, D12 and D12SAS.

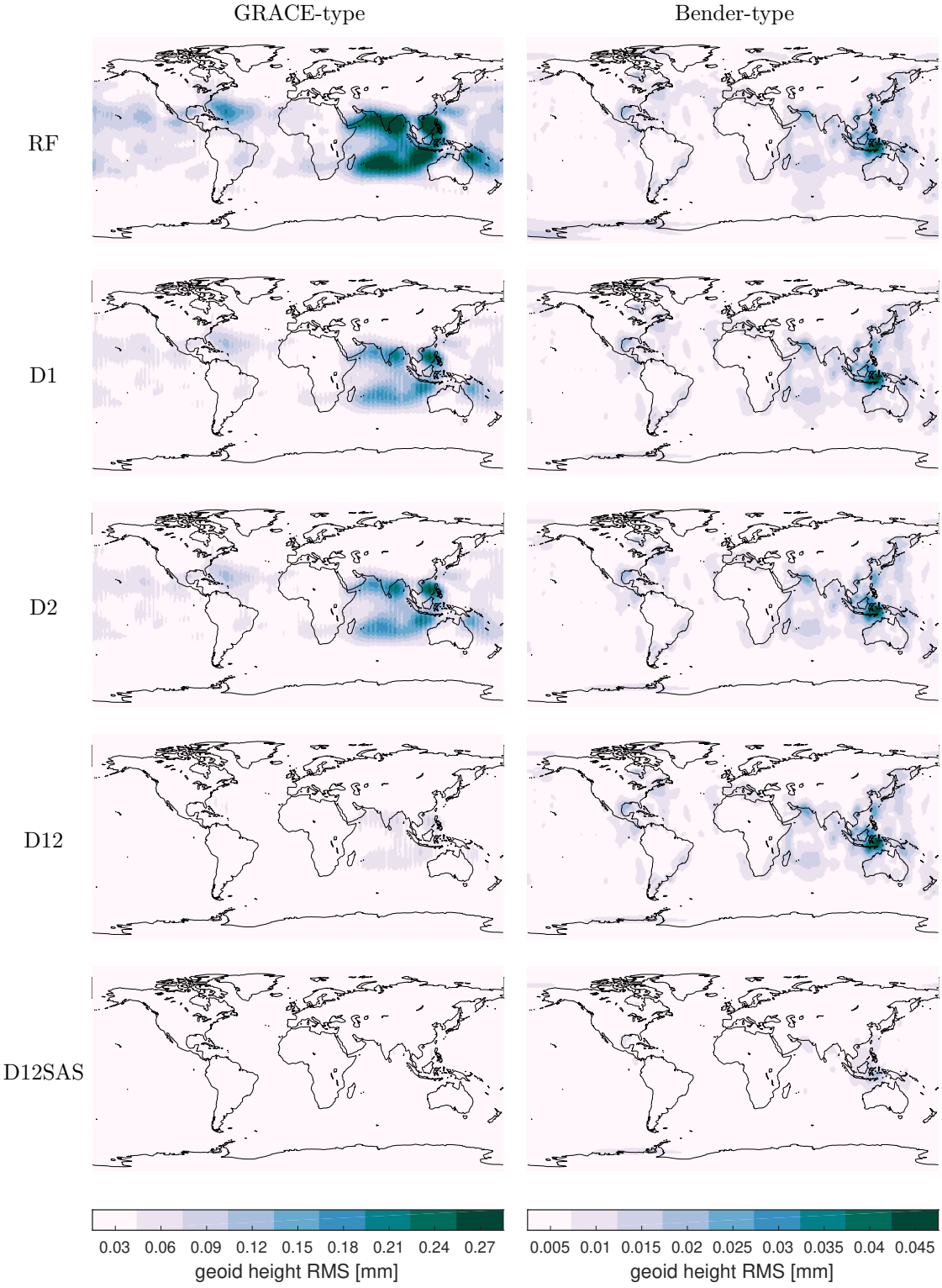

Figure A.9: Geoid height RMS [mm] of Q_1 for five fields: RF, D1, D2, D12 and D12SAS. Each colorbar is valid for its column. Please note the different colorbar ranges for GRACE-type scenarios and Bender-type scenarios.

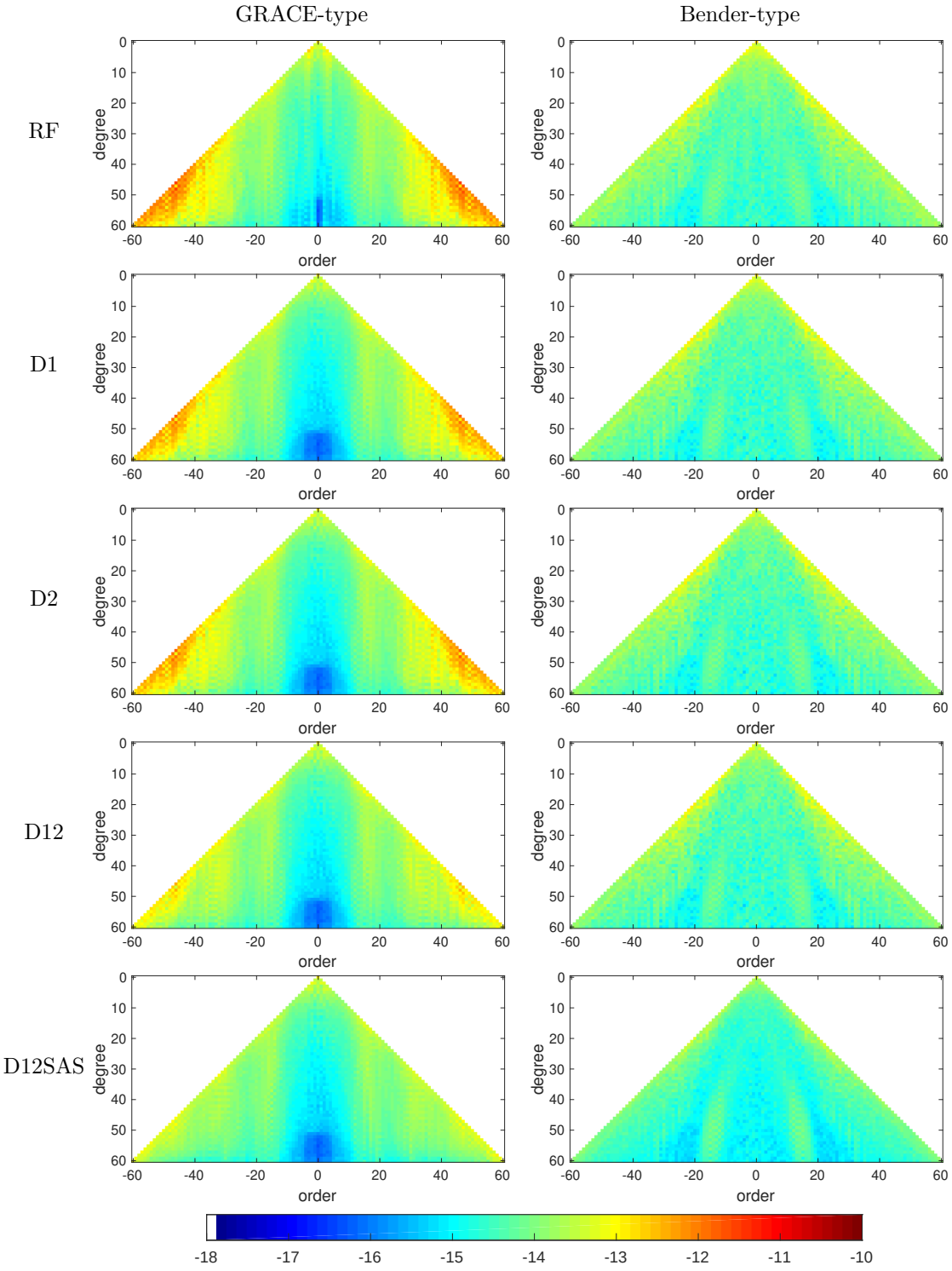

Figure A.10: RMS of individual spherical harmonic coefficients of Q_1 for five fields: RF, D1, D2, D12 and D12SAS.

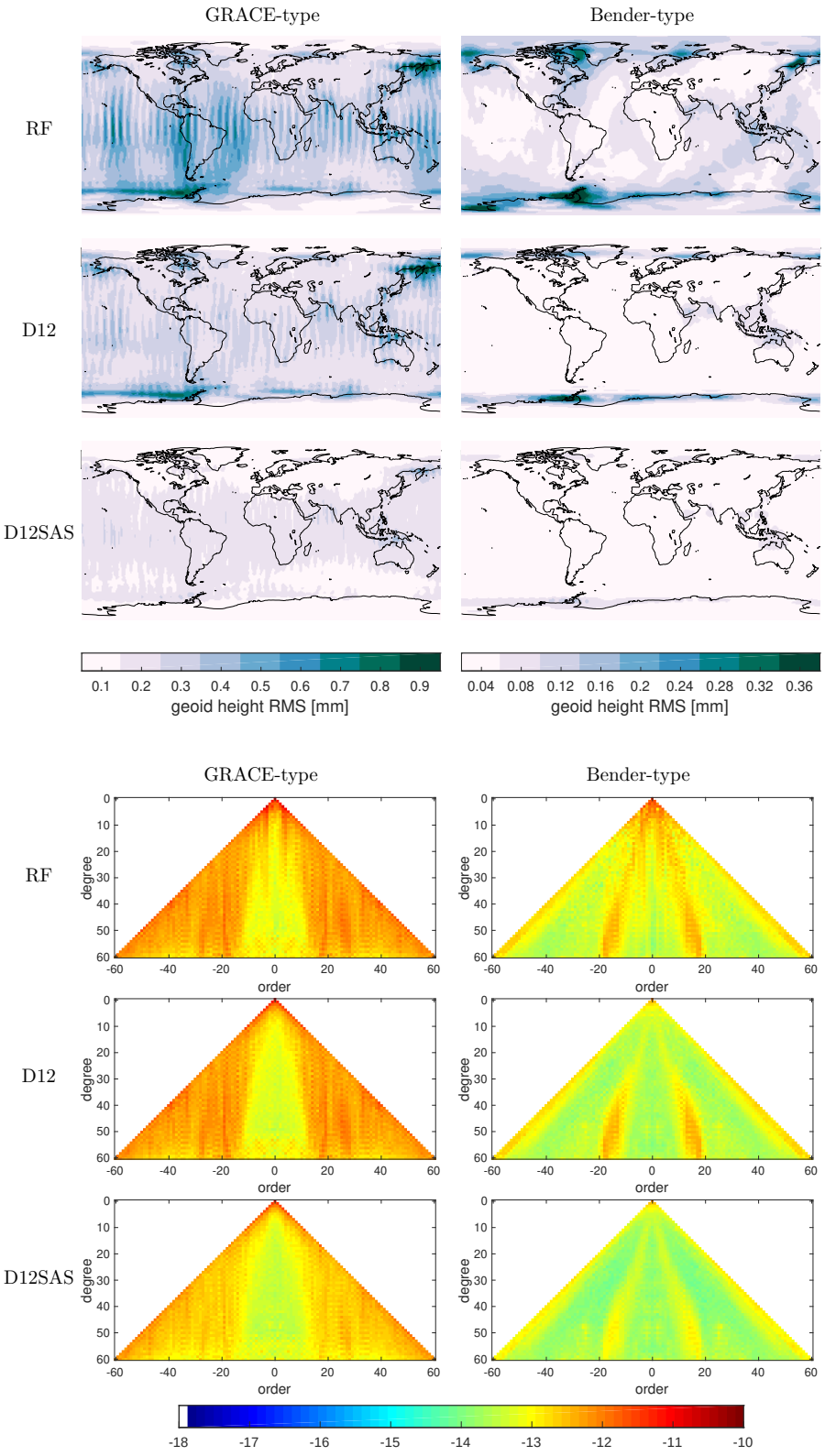

Figure A.11: Geoid height RMS [mm] and RMS of individual spherical harmonic coefficients of K_1 for three fields: RF, D12 and D12SAS. Each colorbar is valid for its column. Please note the different colorbar ranges for GRACE-type scenarios and Bender-type scenarios.